Application and Analysis of the Constant Photocurrent Method in Studies on Amorphous Silicon and other Thin-Film Semiconductors

IVICA ZRINŠČAK

A thesis submitted in partial fulfilment of the
requirements of the University of Abertay Dundee
for the degree of Doctor of Philosophy

This research programme was carried out
in collaboration with the University of Dundee

June 2005

I certify that this thesis is the true and accurate version of the thesis approved by the examiners.

Signed .....[redacted].....

Date...17/8/05.....

(Director of Studies)

To my family

Acknowledgements

The author is greatly thankful to Professor Charlie Main and Doctor Steve Reynolds under whose supervision the research was conducted, their constant interest, encouragement, patience and friendship throughout the course of this work.

The author would also like to express his gratitude to Professor Allan Gillespie and Doctor Colin Cartwright for their kindness, helpful advice and support in bringing this work to a successful end.

Further thanks are due to the following:

- Professor Merv Rose and Doctor Saydulla Persheyev, University of Dundee, for providing HWCVD samples, FTIR and Transmittance measurements.
- Intersolar UK for providing with PECVD samples.
- PD Doctor Rudolf Brüggemann, University of Oldenburg, Germany, for providing samples and helpful advice during this study.
- Doctor Reinhardt Carius, Forschungszentrum Jülich, Germany, for providing microcrystalline samples.
- Doctor Amar Merazga, Faculté des Sciences et Sciences de l'ingénieur, Université Mohammed Khidir, Biskra, Algéria, for his assistance in developing the new CPM model.
- Members of the technical staff for their assistance during this study.

Special thanks are due to Doctor Allan MacLeod, Mariana Gueorguieva, Vladimir Smirnov, Elaine Billen, Robert Sharpe and Fu Yu for their support, useful comments and friendship during this work and to Doctor James Kelly for proof reading this thesis.

The author wishes also to acknowledge the support of EPSRC through research grant no. GR/M 16696.

Declaration

I declare that while registered as a candidate for the degree for which this thesis is presented I have not been a candidate for any other award. I further declare that except where stated the work contains in this thesis is original and was performed by the author.

Signed .... [redacted] ..... Date ..17/08/2005.....

Ivica Zrinščak

Abstract

The opto-electronic properties of amorphous hydrogenated silicon films (a-Si:H) produced by plasma enhanced chemical vapour deposition (PECVD) in a commercial reactor and hot-wire chemical vapour deposition (HWCVD) in a laboratory setup, are subject to light-soaking and annealing and investigated using transient photoconductivity (TPC) and constant photocurrent (CPM) measurements. As a result it is to be found that the HWCVD produced material is competitive with the commercially produced PECVD material and shows a tendency to be more resistant against light-soaking as long as significant contamination does not occur in the deposition process.

Depth profiling by chemical etching and correlation of infrared spectroscopy (FTIR) and CPM results are used to analyse the effect of oxygen and carbon contamination on the photoelectrical properties of a-Si:H material deposited using HWCVD method. It is shown how changing dissociation processes at the heated wire surface, surrounded by silane gas, affect the electronic and structural properties of the a-Si:H material produced.

The optimum growth of a-Si:H material by HWCVD depends very much on the 'substrate to filament' distance, investigated by steady-state conductivity and CPM measurements. It is found that this has a big influence on the optoelectronic properties of the film and on the uniformity of film thickness, which is important for designing large area industrial HWCVD deposition units.

The influence of the silane content (SC) (silane concentration in hydrogen) during the deposition process, in HWCVD and PECVD technique, on the film properties were investigated using CPM and FTIR measurement methods. From correlation between CPM and FTIR results it is shown that for low silane content (< 10%) the structure of the resulting material is predominately microcrystalline (μc-Si:H) and amorphous for high silane content.

Proton irradiation effects on undoped a-Si:H and μc-Si:H samples from PECVD and HWCVD deposition method were investigated by using steady-state photoconductivity and CPM experimental methods before and after 100 MeV proton irradiation. In contrast to 1 MeV electron irradiation, where major changes in the density of states were reported, the proton irradiation did not have any observable effect on the optoelectronic properties of the samples investigated.

As a major part of this thesis the validity and precision of the constant photocurrent method – CPM, as a means to determine the density of states in thin films, is subject to investigation. In the past clear differences have been observed in the absorption coefficient spectrum of a-Si:H between DC - and AC - CPM measurements. In this thesis an explanation for these differences will be proposed and elaborated. DC-CPM measurement gives a consistently higher value for the absorption coefficient α at low photon energies. A small-signal analysis of the photoconductive response to modulated sub-gap illumination reveals low frequency poles associated with thermal emission processes, which explains this discrepancy. Computer simulation demonstrates that while DC – CPM, which includes these transitions, gives a more accurate value for absorption, AC – CPM provides a more accurate means of determining the distribution of occupied gap-states. Further it is shown that combining DC and AC methods allows determination of the distribution of deep *unoccupied* gap-states. These concepts are applied to experimental results for several undoped a-Si:H films.

The CPM method has mainly been applied to measurements on thin film silicon materials. However, in a study on 'non-silicon' materials (i.e. CdTe, GaAs, CdSe & CdS_2) the applicability of the CPM method to these photoconductive materials is demonstrated in this work.

Symbol and abbreviation list

A	Absorptance
a_0	interatomic spacing
B	energy band width of delocalized states
C_n	electron capture coefficient
C_r	hole capture coefficient
D^-	defect state occupied with two electrons
d	film thickness
d	film position
D^+	unoccupied defct state
$D^{+/0}$	recombination path *via* D^+ and D^0
D^0	defect state occupied with one electrons
$D^{0/-}$	recombination path *via* D^0 and D^-
E	electric field
e	electron(s)
e	elementary electron charge
e_n	thermal emission probability for electrons
E	energy
E_c	conduction band energy
E_F	Fermi energy
E_{Fn}	free electron quasi Fermi level
E_{Fn}^t	trap quasi Fermi level for electrons
E_{Fp}	free hole quasi Fermi level
E_{Fp}^t	trap quasi Fermi level for holes
E_g	mobility gap / band gap
E_n	trap depth energy
e_n	emission probability for electrons
e_p	emission probability for holes
E_{ph}	photon energy
E_t	trap energy
E_v	valence band energy
$f(E_t)$	occupation function in non-equilibrium steady-state conductivity

$f_0(E_t)$	Fermi-Dirac occupancy function in a thermal equilibrium
G	generation rate
ΔG	excess generation rate
G_0	thermal generation rate
g_c	density of states at conduction band edge in $cm^{-3}\ eV^{-1}$
G_v	density of occupied states in $cm^{-3}\ eV^{-1}$
G_ω	modulated generation rate
g_v	initial density of states within the band gap in $cm^{-3}\ eV^{-1}$
h	hole(s)
I_{CPM}	CPM photo current, which is held constant during the measurement.
I_{ph}	photo current
$\Delta i(t)$	transient photocurrent
k	Boltzmann's constant
$\boldsymbol{k}$	electron momentum
L	filament to substrate spacing
L_M	filament to substrate distance
N	density of states (DOS) in cm^{-3}
n	electron density
$\overline{n}$	effective electron density at conduction band edge
Δn	excess density of free electrons
n_0	thermodynamic equilibrium free electron density
N_c	conduction band density of states
N_D	density of defects in cm^{-3} in the mid gap
N_t	density of traps
n_t	trapped electron density
p	hole density
$\overline{p}$	effective hole density at valence band edge
Δp	excess density of free holes
p_0	thermodynamic equilibrium free hole density
P_s	silane gas pressure
r	recombination rate
R	refractive index
R_1	refractive index from film surface to air interface

R_2	refractive index from film to substrate interface
T	temperature
t	time
T	transmittance
$\overline{T}$	averaged transmittance
T_c	Characteristic temperature of exponential distribution
T_f	filament temperature
T_{max}	amplitude maxima in transmittance curve
T_{min}	amplitude minima in transmittance curve
T_s	substrate temperature
U	correlation energy
v	velocity
$V(\boldsymbol{r})$	periodic lattice potential
V_0	disorder potential in a-Si network
W	defect lattice relaxation energy
Δx	scattering length

α	absorption coefficient
γ	Rose factor
$h\nu$	photon energy
$\hbar$	Planck's quantum constant
η	quantum efficiency
μ	carrier mobility
μ_e	electron mobility
μ_h	hole mobility
ν_n	attempt to escape frequency
σ	total photoconductivity
$\Delta\sigma$	photoconductivity
σ_0	dark conductivity
σ_n	photoionization cross-section for electrons
τ	electron lifetime
Φ	photon flux

φ	phase shift
ω	modulation frequency
ω_e	emission frequency
ω_r	recombination frequency
ω_t	trapping frequency

Table of Contents

Chapter 1 - Introduction

1.1 Background Information

The element silicon (Si) is the second most common element on earth. Identified as an element by the Swedish scientist J.J. Berzelius in 1823 it took nearly 130 years before it became the most important core material for our modern world wide electronic industry. The breakthrough for silicon came when its semi conducting properties were recognized and after the development of the first transistor at the Bell Laboratories in 1947.

Silicon is produced as polycrystalline silicon using three common methods: the reduction of silicontetrachloride ($SiCl_4$) using zinc (Zn), the reduction of trichlorsilane ($SiHCl_3$) using hydrogen (H_2) and the thermal decomposition of silane (SiH_4). In general, semiconductor grade devices cannot be fabricated directly from polycrystalline silicon without first being converted into single crystal ingot form. This is done by growing a single silicon crystal rod (-> ingot) from the silicon melt. The single crystalline silicon ingots are then sliced into wafers and become ready for the mass production of semiconductor devices such as microchips and solar cells.

A different method of producing silicon was introduced from the work of Chittick et al using thermal decomposition of silane by radio frequency heating onto an unheated substrate as a thin amorphous silicon film (Chittick et al, 1969). The viability of amorphous silicon (a-Si) as photoconductive device originated within the University of Dundee, with the pioneering work of Spear and LeComber (Spear and LeComber 1970, Spear et al, 1974). The discovery of the photoconductive properties and substitutional doping of amorphous silicon have led directly to the world wide interest and industry in photovoltaics (Spear and LeComber 1975). In 1979 LeComber et al introduced the usage of a-Si for field effect devices i.e. the field effect transistor, which boosted in the early 1980's the liquid crystal technology into today's 'Thin Film Transitor' (TFT) display applications (LeComber et al, 1979).

A disadvantage of amorphous silicon is that it is gradually degraded by exposure to light through the Staebler-Wronski effect (Staebler and Wronski 1977). Due to its amorphous structure the carrier mobilities are much lower than in crystalline silicon (c-Si) which makes it less efficient than c-Si. However, because the quantity of silicon material

required for thin films is far smaller than for traditional solar cells, the cost of thin film manufacturing is far less than for crystalline silicon solar cells.

1.2 The properties of amorphous silicon

1.2.1 Atomic structure

Crystalline Silicon *c-Si* has a regular network structure where every silicon atom has exactly four silicon neighbour atoms in a tetrahedral coordination which results in a cubic diamond structure with a lattice constant of 5.42 Å.

The network structure of amorphous silicon differs from the crystalline structure in that there is no long-range order because of many displacements of the silicon atoms from their ideal crystalline position. Short-range nearest neighbour order is only slightly modified but this is enough to result in different bonding lengths and bonding angles between the Si atoms, which makes the long-range order of the network unpredictable. This amorphous network structure is also termed as a 'Continuous Random Network - CRN' (Street 1991, p4).

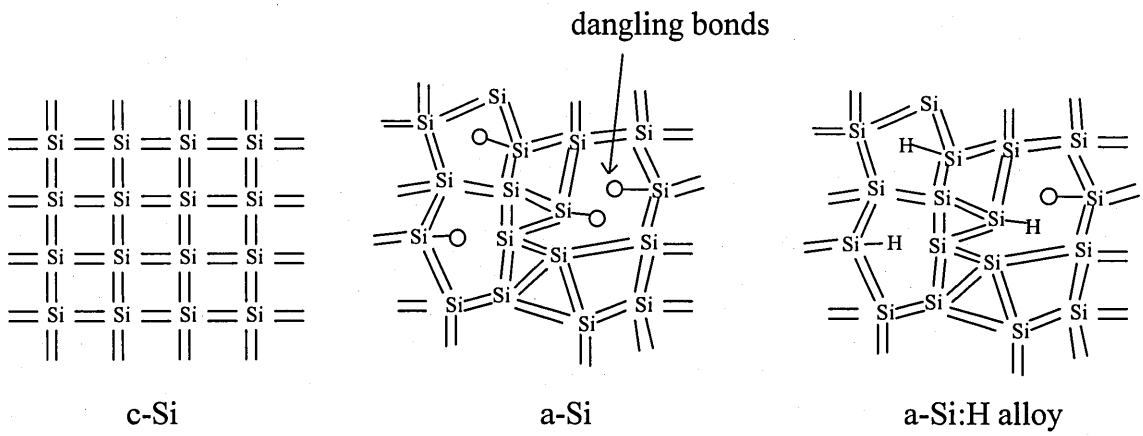

Figure 1.1 Illustrative 2-D schematic of The network structure of crystalline (c-Si) and amorphous silicon (a-Si). Also illustrated are the dangling bonds in the amorphous state and their removal by hydrogen diffusion (a-Si:H alloy).

Figure 1.1 illustrates in a simple 2-D schematic the main differences between the crystalline and amorphous network structure. Also illustrated in the picture of the amorphous state are the 'dangling bonds', which are isolated coordination defects caused when the network is unable to satisfy all the bonds, which can potentially be formed by an atom. The dangling bond defect states are very efficient recombination centres, which results in significant reduced efficiency in photodetector applications. They are caused by the deposition process itself and also by breaking weak bonds between silicon atoms when exposed to light. This effect is also known as the *Staebler-Wronski-Effect* (Staebler and Wronski 1977, Kolodziej 2004).

A solution to minimize dangling bond defect states is to incorporate hydrogen into a-Si material, which will satisfy these bonds. Fortunately the glow discharge deposition method results in much of the hydrogen from the SiH_4 being incorporated into the material (10 % to 20 %). Some hydrogen atoms bond to the Si dangling bonds and drastically reduce the gap centre density of defect states by 3 to 4 orders of magnitude (figure 1.1). The material is termed as *hydrogenated amorphous silicon - a-Si:H* (Fritzsche 1977).

1.2.2 Electronic state structure and optical properties

One fundamental property of a semiconductor is the presence of a band gap separating the occupied valence band from the empty conduction band states. As a result from the free electron theory the band gap in crystalline silicon is a consequence of the periodicity of the crystalline lattice. Due to the short-range order, which is very similar for amorphous and crystalline silicon, the bands are most strongly influenced by local interactions and therefore continue to exist in amorphous material.

The valence band and the conduction band in crystalline and amorphous silicon are described by energy-momentum *(E-k)* dispersion relations, which are the result of Bloch's solutions for the Schrödinger's equation of the electronic states. Because of the periodic lattice potential, $V(\boldsymbol{r})$, in crystalline silicon the wavefunctions have a well-defined momentum, $\boldsymbol{k}$, and extend throughout the crystal. They are said to be extended or delocalised.

In amorphous silicon the situation is different: in a continuous random network structure the potential $V(\boldsymbol{r})$ is not periodic, which is caused by strong scattering of electrons

over a range of only one or two atomic spacing. This strong scattering causes a large uncertainty in the electron momentum $\boldsymbol{k}$, through the Heisenberg uncertainty principle

$$\Delta \boldsymbol{k} = \hbar / \Delta x \approx \hbar / a_0 \approx \boldsymbol{k}, \tag{1.1}$$

if it is assumed that the scattering length Δx is approximately equal to the interatomic spacing a_0. Since $\Delta \boldsymbol{k}$ is in the same order as $\boldsymbol{k}$, the momentum is not a good quantum number and therefore not conserved in electronic transitions (Street 1991, p11).

The consequences of the loss of the $\boldsymbol{k}$-conservation are that energy bands are no longer described by the E-$\boldsymbol{k}$ dispersion relations but instead by a density-of-states (DOS) distribution $N(E)$ illustrated in figure 1.2. Optical transitions which are forbidden by momentum conservation do not apply to amorphous semiconductors therefore the distinction is lost between direct and indirect semiconductors. Silicon has an indirect band gap in its crystalline phase but not in the amorphous phase.

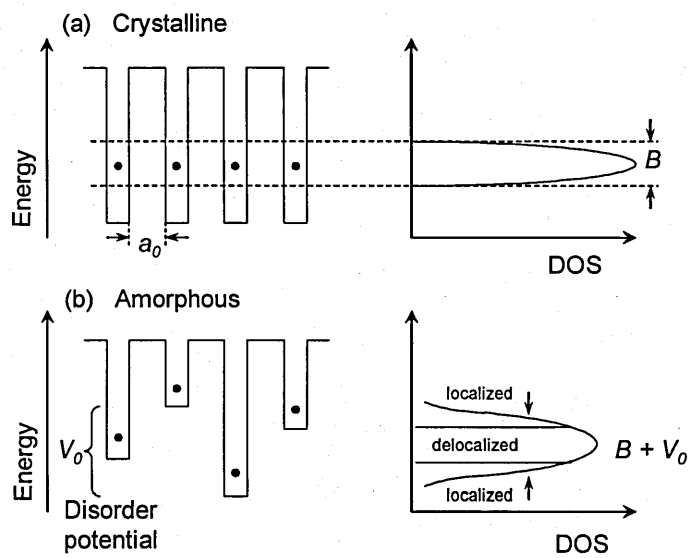

Figure 1.2 Anderson model of the potential wells for (a) crystalline and (b) amorphous network. V_0 is the disorder potential

A further consequence of the disorder potential is the existence of localized wavefunctions confined to a small volume of material rather than being extended. The Anderson model illustrated in figure 1.2 (a) describes the crystalline phase by a regular

array of identical atomic potential wells. The interaction between the atoms broadens the state energy to form a narrow band of delocalised states of the energy width B. In the disordered state illustrated in figure 1.2 (b) the same array of sites is varied by a random potential of average magnitude V_0 that broadens the band.

Anderson showed that when V_0 / B exceed a critical value all of the states of the material are localized and there is no electrical conduction at zero temperature. Even if the Anderson criterion is not met, there are still localized states at the extreme edges of the band where the centre of the band comprises extended states as proposed by Mott and Davis (Mott and Davis 1979).

In reality the energy bands of amorphous semiconductors are too broad compared to the disorder potential for complete localization but the band edges are broadened and the states there are localized. These are referred to as *tail states* or *band tails.* The extended and localized states are separated by a mobility edge at energy E_c which is also referred as *band gap*. Only electrons above E_c are mobile and contribute to the conduction (Anderson 1958, Mott and Davis 1979).

1.2.3 The standard density of states – DOS

To describe the electronic properties of amorphous silicon it is necessary to obtain the energy distribution of electronic states. Depending on their character the different states determine the electrical transport, recombination etc. As mentioned previously due to the disorder of the network structure in a-Si:H the energy distribution of electronic states is broadened into the energy gap between E_c and E_v compared with the model for crystalline silicon. Figure 1.3 illustrates the schematic electronic state structure for an amorphous semiconductor as described in Overhof and Thomas (Overhof and Thomas 1989). The density of states distribution model consists of three main sections: the main conduction and the valence bands, the band-tail regions close to the valence and conduction bands and the defect states in the mid gap. The abrupt band edges of a crystalline semiconductor (dashed curve) are replaced by a broadened tail of states extending into the band gap, which originates from the deviations of the bond length and angle arising from the amorphous network structure. The valence band tail is more influenced by deformations of the a-Si network structure than the conduction band tail, which results in different *Urbach*

energies E_U, determined from the exponential energy dependence of the optical absorption, which is the slope of the valence- (conduction-) band tail (Urbach 1953). Typical values for the valence band tale are between 45 – 55 meV and for conduction band tail about 25 – 35 meV for good intrinsic material.

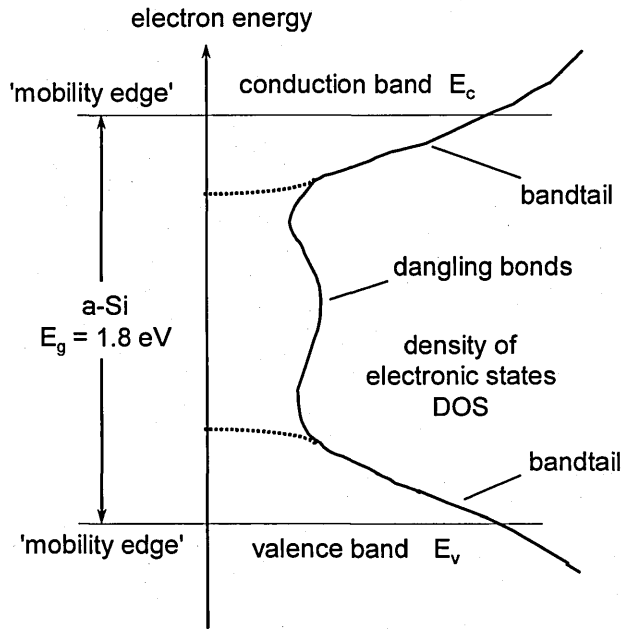

Figure 1.3 Standard model of the density of states (DOS) distribution of an amorphous semiconductor showing the bands, the band tails, and the defect states in the band gap. The dashed curves are the equivalent density of states in a crystal.

The band tails are most important because electronic transport occurs at the band edge. Electronic states deep within the gap arise from departures from the ideal network, such as coordination defects or unsatisfied Si-bonds. At the energy E_c (E_v for the valence band) where the band-tail localized states and the extended states are separated by what is called the *mobility edge* or *band edge* and the region between E_c and E_v the *mobility gap* or *band gap*. These concepts replace the band edge and the band gap of the crystalline theory.

Charge transport is determined whether the states creating the conduction path are above or below the mobility edge. Note it is widely accepted to use the terms *band edge* and *band gap* in the amorphous material field. The typical band gap energy E_g for crystalline silicon is 1.14 eV. The corresponding energy in non-doped amorphous silicon lies between 1.7 eV and 1.8 eV. The density of deep defects (dangling bonds) N_D also

termed as defect density is in good quality a-Si:H (10 % hydrogen content) typically around 10^{16} cm^{-3}. The free carrier mobility in a-Si is about 100 times smaller than in c-Si because of frequent scattering in the band states in a random potential, while the drift mobility is even smaller because of trapping events in the tail states. Typical value for the electron mobility μ_e in a-Si:H is about 10^{-3} $m^2 V^{-1} s^{-1}$ and about 0.14 $m^2 V^{-1} s^{-1}$ for c-Si.

1.2.4 Photoconductivity

Photoconductivity occurs when carriers are optically excited from non-conducting to conducting states. It is an indirect measure of the recombination and does not distinguish between radiative and non-radiative mechanisms. Under illumination electrons and holes are excited to the band edges where they drift towards the appropriate electrodes under the applied electric field E.

For crystalline semiconductors photoconductivity is mainly dominated by transitions from the valence band into the conduction band. In the case of c-Si direct optical transitions are not allowed because of the $\boldsymbol{k}$-conservation. The corresponding states from the valence band and the conduction band lie at different values of $\boldsymbol{k}$. Both the quasi-momentum of the electron and its energy has to change during the transition. As the photon has negligibly small momentum phonon participation is required to provide the necessary momentum change. This process is called phonon-assisted absorption. Hence crystalline silicon is classified as an *indirect semiconductor*.

Transport in amorphous silicon is not as easy to describe as in crystalline silicon. While electronic transport above the band edge is dominant at high temperatures, at lower temperatures the *multiple trapping* mechanism influences more and more the electronic transport (Tiedje and Rose, 1980). Multiple trapping is described as electronic transport between delocalised states above E_c and localized states below E_c.

At low temperatures the *hopping* mechanism also becomes significant, which is the electronic transport between localized states in the mobility gap (Mott 1968). Defect states in the mobility gap play a role as recombination centres in the photoconductivity. Hence it is important to reduce the amount of defects to improve the electronic properties of amorphous silicon.

1.3 Production processes of amorphous silicon

1.3.1 Background

The main aim in the production of amorphous silicon is to develop a deposition method that will produce amorphous silicon films with a low defect density, high carrier mobility and enhanced stability against degradation as well as a low-cost production possibility.

The usual method of depositing a-Si:H is by plasma decomposition of silane gas SiH_4. Silane decomposes in the absence of plasma above about 450 °C but films grown in this way are mostly of low quality because the temperature is too high to retain the hydrogen and as a result the defect density becomes so high that it will render them useless for electronic applications. By decomposition of silane at lower temperature in plasma the hydrogen is able to passivate dangling bonds which results in much higher quality films and also allows doping during the growing process (Spear and LeComber 1977).

The first plasma deposition system for the production of amorphous silicon films was developed by Chittick et al, which was a radio frequency inductive system (Chittick et al, 1969). Since then different methods have been developed to produce hydrogenated amorphous silicon films and the following chapters will focus on two popular techniques called *plasma enhanced chemical vapour deposition - PECVD* and *hot-wire chemical vapour deposition – HWCVD also* referred as *catalytic CVD*, since materials produced in these ways are the subject of this thesis.

1.3.2 Plasma enhanced chemical vapour deposition – PECVD

The PECVD deposition method is the preferred technique in industry to produce high quality amorphous silicon films and devices because it is presently the only method to satisfy industrial requirements. It is based on a radio frequency (RF) capacitively coupled system (often referred to as the glow-discharge method) where a plasma is created between two parallel electrodes in a deposition chamber (Street 1991, p18, Roca I Cabarrocas 1998, 2000). Figure 1.4 illustrates a schematic diagram of a typical RF-PECVD plasma reactor.

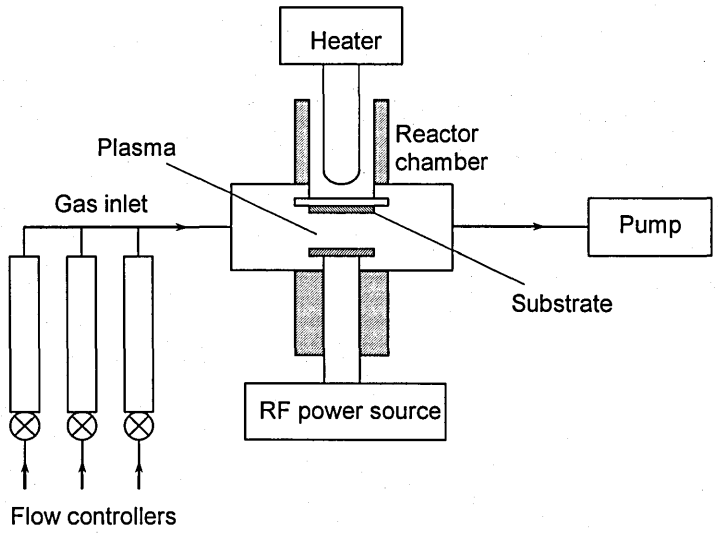

Figure 1.4 Schematic diagram of a typical RF-PECVD reactor for depositing a-Si:H (from Street 1991, p19).

The reactor contains a set of gas inlet arrangements (for silane, hydrogen, doping gases, etc.), the deposition chamber that holds the substrate (e.g. Corning glass 7059) including its heating system, a pumping system and the source of power for the discharge.

To produce good material there are several parameters to be controlled. The gas pressure determines the mean free path for collisions of the gas molecules and influences whether the reactions are at the growing surface or in the gas. The gas flow rate determines the residence time of the gas in the reactor. The RF power controls the rate of dissociation of the gas and therefore also the film growth rate. The temperature of the substrate controls the chemical reactions on the growing surface.

Deposition usually takes place at a gas pressure of 0.1-1 Torr (→ *plasma enhanced*), which is the optimum pressure to sustain the plasma. For the plasma excitation frequency *RF* 13.56 MHz is used as a standard. It is universally accepted that the most important parameter controlling the electronic properties of a-Si:H is the substrate temperature *Ts*. Between 200 °C and 300 °C optimum device quality material is usually produced. Less well-defined is the optimum gas flow rate because of the various designs of reactor chambers.

The film growth mechanism is described as follows: a discharge is sustained by the acceleration of electrons by the applied electric field. These electrons collide with gas

molecules causing ionisation and more electrons. Acceleration of the ions in the plasma is negligible because of their large mass. At temperatures above 550 °C silane gas dissociates into neutral radicals or ions. Examples of dissociation reactions are,

$SiH_4 \rightarrow SiH_2 + H_2$ at 2.2 eV

$SiH_4 \rightarrow SiH_3 + H$ at 4.0 eV

$SiH_4 \rightarrow Si + H_2$ at 4.2 eV

The creation of SiH_3 radicals is important because they are less reactive so they survive the collisions longest and therefore are more likely to reach the substrate surface. The next step in film growth is the adsorption of molecular fragments onto the growing surface followed by the release of hydrogen from the surface. The hydrogen release is a necessary step because terminated Si-H bonds will not take up any SiH_3 radicals. Bonding of SiH_3 can only occur at any non-terminated silicon bond. The result is an a-Si:H film with about 10 % hydrogen for good quality. The hydrogen is very important for production of good quality material because of its fortunate property of being able to remove any subsurface defects left by the deposition process when attached to a silicon-dangling bond (Street 1991, p29, Robertson 2000).

By adding additional gases into the deposition process like phosphine (PH_3), or diborane, (B_2H_6), it is possible to produce doped amorphous silicon films either as n-type (by phosphine) or p-type (by diborane) material. This possibility enables production of electronic devices such like TFT transistors or amorphous silicon solar cells.

Some newer modification of the standard PECVD deposition method is to increase the plasma excitation frequency up to 300 MHz (VHF-PECVD), which results in an enhanced deposition rate by almost one order of magnitude compared with standard PECVD. But in the last 10 years a different deposition has gained more popularity because it allows lower substrate temperatures and higher deposition rates and enables the production of films with better electronic properties. The main difference from the PECVD method is that it uses a hot tungsten wire to dissociate catalytically silane gas and therefore it is termed as *catalytic-CVD* (CAT-CVD) or *hot-wire CVD* (HWCVD) (Matsumura 1998, Masuda et al, 2002).

1.3.3 Hot-wire chemical vapour deposition – HWCVD

The hot-wire CVD deposition method was developed to overcome problems arising from the PECVD deposition method influenced by the plasma or from charge-induced damage. Wiesmann et al (Wiesman et al, 1979) reported that silicon thin films could be formed by cracking silane gas with a heated tungsten (W) or carbon filament. Mahan et al (Mahan et al, 1991) succeeded in producing high quality a-Si:H films and called the method hot-wire CVD (HWCVD).

The HWCVD arrangement consists mainly of three parts: the parts for the gas inlet into the low-pressure deposition chamber, heated catalyser for gas decomposition by the catalytical cracking reactions and the substrates for film formation. For the heated catalyser mostly tungsten wire is used because the melting point of tungsten is as high as 3382 °C and it remains as high as 2165 °C even when the surface of W is converted into silicide by the reaction with silane gas.

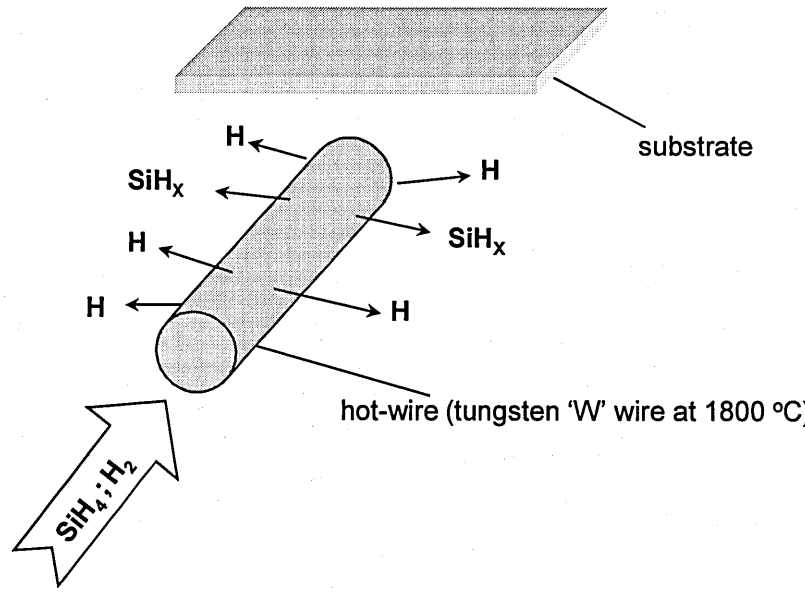

Figure 1.5 Schematic diagram of a hot-wire deposition setup typically with a W filament. Parameters that can be varied are i.e. the wire-temperature, distance between wire and substrate, gas pressure, filament temperature, silane and hydrogen flow rates.

In HWCVD the hot tungsten filament (~ 1800 °C) assists a catalytic decomposition of a silane and hydrogen gas mixture as illustrated in figure 1.5. The catalytic process is as follows (Matsumura 1998, Abe et al, 2000, Gallagher 2001, Holt et al, 2001): at filament temperature T_f greater than 1800 °C and low silane gas pressure P_s, SiH_4 reacts with the filament followed by the release of four H- and one Si-atom from the filament. This is expected at high T_s and low P_s because H desorbs from the filament more rapidly than it is supplied by SiH_4 decomposition, so H atoms are bonded to a small fraction of the surface-W atoms. For such H-depleted conditions and high thermal energy the probability of SiH_4 reaction with surface W-dangling bonds is high and after the SiH_4 reacts the Si and H atoms diffuse away from each other until they thermally break their surface W-bond and escape. The primary radical species leaving the surface are thus H and Si. As T_f is lowered more W surface bonds are H terminated and the probability decreases for reaction between silane and W. On the other hand the release of Si and H atoms decreases faster than the reaction probability between silane and W implying that some of Si from the decomposed silane is absorbed into the W-matrix, and that H_2 in addition to H is released.
As T_f is further lowered below 1500 °C Si release becomes negligible; almost all Si from decomposed silane is incorporated into and onto the W. This causes severe stress and ultimate wire breakage at ~ 1200 °C.

Usually HWCVD deposition takes places at filament Temperatures between 1800 °C and 2200 °C depending on the gas pressure (~ 0.001 Torr). Substrate temperature is between 150 °C and 250 °C (Heintze et al, 1996, Iiduka et al, 1997, Tange et al, 2001).

As in PECVD, since the deposition species are formed outside the substrate surface, the film can be grown at low substrate temperatures.

It is reported that HWCVD produced films are more resistant against degradation than PECVD produced films. Also it was mentioned that the photosensitivity, which is the ratio of the photoconductivity to the dark conductivity, is slightly better than in PECVD films (Matsumura 1998, Itoh et al, 2001).

In following chapters PECVD and HWCVD produced films are going to be investigated by defect spectroscopy methods to obtain the quality difference between both deposition methods.

1.4 The properties of microcrystalline silicon - μc-Si:H

1.4.1 Preparation conditions compared with a-Si:H

Microcrystalline silicon is an intermediate structure between the amorphous and poly crystalline phase of silicon. The main advantage of this material is that it is not as affected by the Staebler-Wronski effect after light induced degradation as a-Si:H (Liu and Xu 1986). Furthermore the absorption coefficient of this material is a superposition of the amorphous and crystalline phase that should result in more efficient solar cell application (see figure 1.7). The production of μc-Si:H is similar to the deposition process of a-Si:H. It can be produced either in PECVD or HW-CVD. The production of μc-Si:H is mainly controlled by varying the silane to hydrogen gas ratio (also termed silane content SC) during deposition. Increasing the silane concentration the structure can change from mainly crystalline fractions towards mainly amorphous growth with small crystalline inclusions. Typically the silane content values for μc-Si:H material is about 5% to 7% (Wanka et al, 1996, Stiebig et al, 2000, Dalal 2001).

The starting point of the growth process of μc-Si:H is an initial amorphous silicon layer on which the silicon radicals arrange themselves in a crystalline structure but not exactly like in crystalline silicon. The structure looks like an arrangement of lots of crystallites as in polycrystalline silicon but with much smaller dimensions. μc-Si:H is also known as nano-crystalline silicon. Figure 1.6 shows the structure changes in silicon from the amorphous phase up to the microcrystalline phase for different silane content.

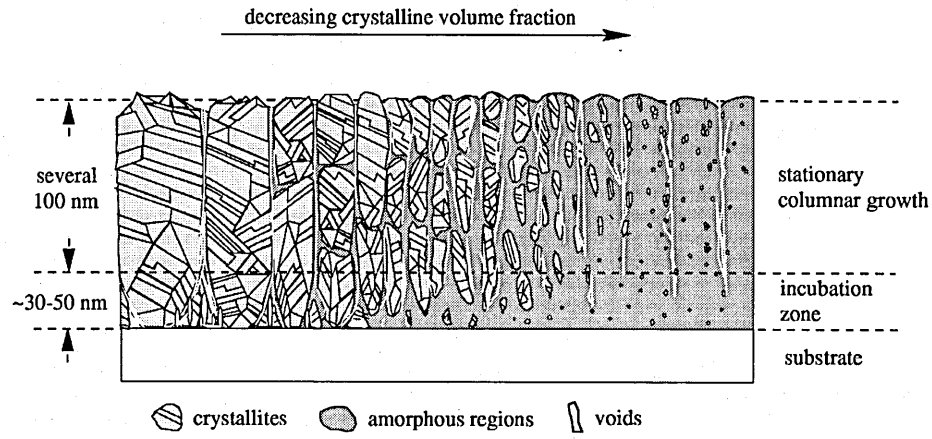

Figure 1.6 Schematic illustration of the different structural phases for microcrystalline silicon when decreasing the silane content from left to right (taken from Vetterl et al, 2000).

1.4.2 Electronic and optical properties of microcrystalline silicon

To determine the optical properties of μc-Si:H, the constant photocurrent measurement technique (CPM) was used to obtain the absorption coefficient which is shown in figure 1.7 (see also chapter 7.5). For comparison the absorption coefficient data for a-Si:H and c-Si are plotted (see also Vetterl et al, 2000). For photon energies above 1.7 eV the absorption coefficient is higher than for c-Si which could be explained by absorption in the amorphous phase and light scattering. For photon energies below 1.7 eV the absorption coefficient of μc-Si:H becomes similar to c-Si but is at least 2-3 times higher then for a-Si:H. For photon energies below 1.1 eV the absorption coefficient of μc-Si:H show similarities to defect-related absorption like a-Si:H but still needs to be further classified.

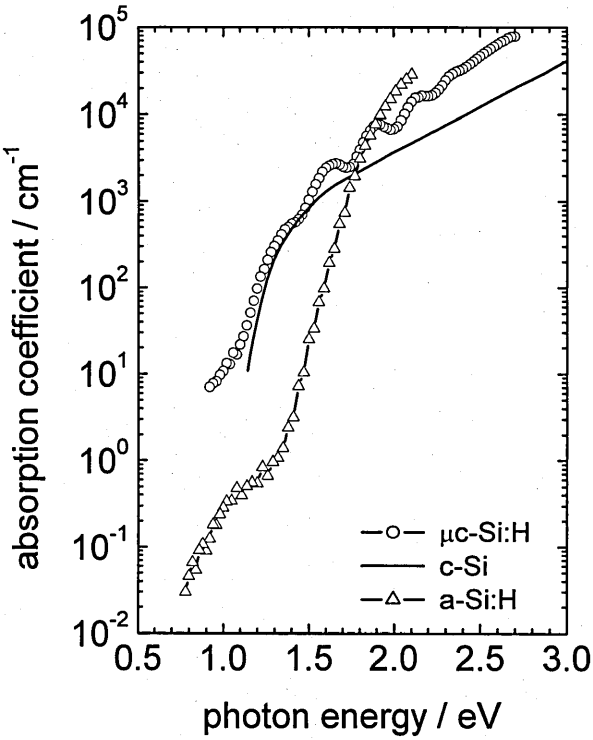

Figure 1.7 Absorption coefficient spectra obtained by CPM for microcrystalline Silicon (μc-Si:H), crystalline silicon (c-Si) and amorphous silicon (a-Si:H).

Measurements of the dark conductivity σ_0 at room temperature for μc-Si:H results in values at 2 - 3 orders of magnitude higher than for a-Si:H. Thus the mobility-lifetime product $\mu\tau$ measured by excitation with 1.96 eV photons results in values similar to a-Si:H.

Typical $\mu\tau$-products for good quality intrinsic microcrystalline silicon are about 10^{-6} $cm^2 V^{-1}$ to 10^{-5} $cm^2 V^{-1}$ (Brüggemann et al, 1998, Vaněček et al, 1998, Brüggemann et al, 1999).

The determination of the bandgap for μc-Si:H from optical transmittance measurements results in high values for the optical gap in the range of 1.9 eV to 2 eV. However, these results may be misleading to qualify the material as a high-gap semiconductor. Indeed, looking at the lower part of the absorption coefficient spectrum obtained by constant photocurrent method reveals a low optical gap which almost becomes identical to that of monocrystalline silicon.

1.4.3 Applications for microcrystalline silicon

Due to the high absorption of this material below 1.7 eV compared to a-Si and the resistance against light induced aging and a $\mu\tau$ - product similar to that of a-Si makes this material very promising for using in solar cell applications. Microcrystalline p-i-n thin film solar cells have already been produced but shown efficiency far below of amorphous p-i-n solar cells. This might be explained with the complicated transport mechanism especially the influence of the grain boundaries in μc-Si:H which still needs further investigation. Latest efficiency data for μc-Si:H p-i-n thin film solar cells are about 10% (Meier et al, 1998, Matsumura 1998, Vetterl et al, 2000).

1.5 Measurement techniques - defect spectroscopy

The quality of amorphous silicon material depends very much on the number of defects contained therein which is specified as the defect density N_D. Good quality a-Si:H films are specified as having a defect density less than 10^{16} cm^{-3}. The aim is to produce amorphous silicon films with a defect density as low as possible. The defect density can be obtained by several measurement techniques such as *optical transmittance measurement*, *electron spin resonance - ESR*, *transient photoconductivity measurement - TPC*, *photothermal defection spectroscopy - PDS* and *constant photocurrent measurement - CPM.*

In this thesis the CPM method is the main measurement application of interest. In addition measurement results will be presented from optical transmittance, steady-state photoconductivity, FTIR and TPC measurements. ESR and PDS measurements are not part of this thesis but they also belong to the widely used defect spectroscopy applications.

1.5.1 Optical transmittance measurement

Optical transmittance measurements are very commonly used to obtain the absorption coefficient for any kind of thin silicon films. It is straightforward in principle, and operates only by comparing the intensity of a reference beam against the intensity of a transmitted probe beam. The measured *transmittance spectrum* is analysed by specially written software which gives results for the absorption coefficient spectra, thickness, and changes in the refractive index over the measured energy range of the sample. The basic relationship between the absorption coefficient $\alpha(E_{ph})$, sample thickness d, refractive index R_1 from '*a-Si:H surface to air*' interface, the refractive index R_2 from '*a-Si:H to substrate*' interface and the averaged transmission $\overline{T}$ is

$$\overline{T} = \frac{(1-R_1)(1-R_2)e^{-\alpha d}}{1-R_1R_2e^{-2\alpha d}} \text{ with } \overline{T} = \sqrt{T_{\max}T_{\min}} \,. \tag{1.2}$$

For amorphous silicon films $\alpha(E_{ph})$ can be obtained over a range limited to high photon energies only. Absorption coefficient data for photon energies lower than 1.7 eV are not

obtainable by this measurement technique because of increasing interference influences in the transmittance spectrum towards smaller photon energies.

The results from optical transmittance are used to scale $\alpha(E_{ph})$ measured by PDS and/or CPM (see below) to absolute scale and to extend the $\alpha(E_{ph})$ spectrum towards higher photon energies (Swanepoel 1983, Hishikawa et al, 1991).

1.5.2 Electron spin resonance – ESR

ESR is used to reveal structural information about defects. When a single electron occupies a quantum state the two states of the *Pauli* pair are normally degenerate, but are split by a magnetic field. Paramagnetism and ESR are the result of the transition between the split energy levels.

The transition occurs at microwave frequencies for the usual magnetic fields. The strength of the microwave absorption gives information about the local bonding structure. The density of spins measured by ESR is equal to the defect density N_D. The results from ESR are often used to calibrate the density of defect states obtained by CPM and/or PDS measurements.

ESR is only sensitive to defects occupied by one electron only (D^0) because defects occupied by two electrons (D^-) or empty defects (D^+) are not paramagnetic (Street 1991, p109, Shimizu et al, 2001).

1.5.3 Fourier-transform infrared spectroscopy – FTIR

FTIR measurements are not directly related to defect density measurement of a-Si:H films but are used to investigate the type of silicon-hydrogen bondings (Si-H, $Si-H_2$, $Si-H_3$) and possible impurities (i.e. silicon-oxygen or silicon-nitrogen bonding) in amorphous silicon films, which have a major influence on the structural and electronic properties of this material. The basic concept of this spectroscopy method is based on the concept that when hydrogen bonds to the a-Si network it creates a local vibrating dipole with the next neighbouring Si-atom because of the electro-negativity difference between the H-atom (slightly positively charged) and the Si-atom (slightly negatively charged). This dipole acts like a harmonic oscillator: when an infrared resonant photon is absorbed by the oscillator

the Si-H dynamic dipole moment is changing, exciting the oscillator to the next higher vibrational level with a larger dynamic dipole moment due to the increased vibrational amplitude. This change in the dynamic dipole moment and the number of bonded hydrogen atoms involved contributing to a specific line, determines the intensity of the corresponding infrared absorption.

Significant Si-H_x vibrational modes are at 630 - 640 cm^{-1}, the 'wagging' mode, at 850 - 890 cm^{-1}, the 'scissor' mode, and at 2000 - 2100 cm^{-1} the 'stretching' mode, which is used to distinguish between a-Si:H and μc-Si:H material (Brodsky et al, 1977, Stutzman 1998).

1.5.4 Photo-thermal deflection spectroscopy – PDS

PDS is used to measure the absorption coefficient for photon energies below the bandgap of amorphous silicon. PDS measures the heat absorbed in the sample and detects all possible optical transitions. Measurement setup: a sample is immersed in a liquid whose refractive index is strongly depended on the temperature. When illuminating the sample with monochromatic light the sample heats up and changes the refractive index of the surrounding liquid. A laser beam passing very close to the samples surface is deflected by the changing refractive index. The value of this deflection is proportional to the generation rate G and thus $\alpha(E_{ph})$ can be obtained. PDS is also referred to as a non-contact measurement because the sample doesn't have any surface contacts that might influence e.g. a photocurrent measurement, but on the other hand, it is very sensitive to surface absorption which influences the overall absorption spectrum (Jackson et al, 1981, Siebke et al, 1997).

1.5.5 Transient photocurrent measurement – TPC

Transient photoconductivity (TPC) is defined as the photoconductive response to impulse (typically 620 nm wavelength laser pulse of 5 ns duration) optical excitation of a photoconductor. Figure 1.8 shows schematically the experimental setup for TPC. In a brief description the TPC measurement may be described as follows: the response of a semiconductor to a short exciting impulse $G(t) = n\,\delta(t)$ generating n free carriers per unit volume, which is collected as a set of sampled TPC data points $\Delta i(t_k)$ at arbitrary time points t_k.

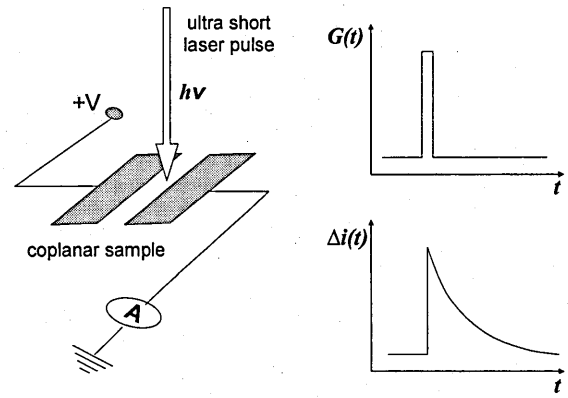

Figure 1. 8 Schematic diagram for the transient photoconductivity (TPC) experimental setup.

Information on the density of states may be obtained by transforming the TPC impulse response into the frequency domain. The frequency response for the photoconductor maybe found by performing a numerical Fourier transform of the TPC impulse response. Note that the conventional FFT procedures are unsuitable because of the wide range of current and time which are involved. Writing the complex AC photocurrent at a modulation frequency ω_n as $I(\omega_n)$, then the simplest scheme (Main et al, 1993, Webb 1994, Main 1997) gives

$$I(\omega_n) = \sum_k \Delta i(t_k)[\cos(\omega_n t_k) - j\sin(\omega_n t_k)]\Delta t_k . \tag{1.3}$$

In practice, windowing and spline fitting are also employed to compute the integral (in practice, a summation) more accurately. The DOS $g(E_n)$ at specific energies E_n, now may be calculated from

$$g(E_n) \approx \frac{2ne\mu_e EA}{C_n \pi kT} \mathrm{Im}\{1/I(\omega_n)\}, \text{ with } E_n = kT\, ln(v_n), \tag{1.4}$$

where μ_e is the free electron mobility, C_n is the electron capture coefficient, E is the applied electric field and A is the conduction path cross-sectional area of the film. The energy E_n is the trap depth below E_c for which the mean emission time $t = 1/\omega_n$, n is the initial excess density, and attempt-to-escape frequency is v_n.

1.5.6 Steady-state photoconductivity - μτ-product

A very commonly used parameter, obtained from steady-state measurement of the *photoconductivity* $\Delta\sigma$ is the $\mu\tau$ – *product*. It consists of the *mobility* μ and the *lifetime* τ of the majority charge carrier (it is assumed here the majority charge carrier are electrons *e*). From

$$\Delta\sigma = en\,\mu_e \text{ with } n=G\,\tau, \tag{1.3}$$

where G is the generation rate and n the density of free carrier, it is possible to obtain the $\mu\tau$ – product. Its value is an indicator of the optoelectronic properties of a-Si:H material. Good undoped a-Si:H films have a $\mu\tau$ – product between 10^{-6} $cm^2\,V^{-1}$ and 10^{-7} $cm^2\,V^{-1}$. In general a high $\mu\tau$ – product leads to good optoelectronic properties but also can be an indicator for doping influences.

1.5.7 Constant photocurrent measurement – CPM

CPM is, like PDS, a further method to measure the absorption coefficient for photon energies below the bandgap. Unlike PDS, CPM involves measurement of the photocurrent arising from optical generation, and further, keeping the measured photocurrent of a sample constant by varying the photon flux over the desired photon energy range. Only transitions which are contributing to the photocurrent are detected by CPM. The measured absorption coefficient is directly proportional to the inverse photon flux and hence in zero order approximation proportional to the DOS (Grimmeis and Lebedo 1975, Vaněček et al, 1981).

The next chapter will take a deeper look into the basic theory of the CPM measurement method, where the relationship between the steady-state photoconductivity and the density of states – DOS will be presented as well as the methods to calculate the DOS from absorption coefficient spectra obtained by CPM measurements.

Chapter 2 - Constant Photocurrent Method – Theory

2.1 Introduction

The Constant Photocurrent Measurement technique – CPM – was introduced 1974 by Grimmeis and Lebedo (Grimmeis and Lebedo, 1974) to investigate the defect density distribution of crystalline silicon (c-Si) and gallium arsenide (GaAs). In 1981 CPM was used by Vaněček et al (Vaněček et al, 1981) to investigate the defect density distribution in a-Si:H. Since then CPM has become an essential tool for obtaining the defect density in all types of a-Si:H materials because of its relatively easy setup and good resolution at photon energies lower than 1.3 eV.

As mentioned already CPM is an easy to use experimental method to obtain the *defect density distribution* N_d in the bandgap of amorphous silicon. By altering the intensity of a monochromatic beam of light the *photo current* I_{ph} and therefore *lifetime* τ of the excess or photo- carriers in a sample is kept constant as *photon energy* E_{ph} is varied (since the excess density $\Delta n = G\tau$). The amount of *photon flux* Φ needed to keep the photo current constant for each value of photon energy is monitored by calibrated photo detectors. The inverse value of the photon flux monitored is directly proportional to the *absorption coefficient* $\alpha(E_{ph})$ which can be written as

$$\alpha(E_{ph}) \propto \frac{C}{\phi(E_{ph})}, \text{ for } 0.5 < \gamma < 1 \text{ and } \alpha d << 1 \qquad (2.1)$$

where C is a constant and the Rose-factor γ, which represents the dependence between the photoconductivity and the generation rate by $\Delta\sigma \propto G^{\gamma}$ with γ assumed to be spectrally independent. Equation 2.1 presents the core relation of the CPM method. The following chapters will show the origin of this relation followed by the analysis of the CPM spectra; the limitation of the CPM method, the most common used experimental methods (i.e. AC, DC and absolute CPM) to perform a CPM measurement and a detailed description of the CPM setup used in this thesis. To understand the principle of this measurement method it is necessary to have a deeper look into the physics of photoconductivity in a-Si:H.

2.2 Steady-state photoconductivity

In a steady uniform illumination of a certain wavelength the conductivity changes by altering the carrier density. The observed *total conductivity* under illumination σ is defined as the sum of the *photoconductivity* $\Delta\sigma$ and the *dark conductivity* σ_0 in thermodynamic equilibrium.

$$\sigma = \sigma_0 + \Delta\sigma. \tag{2.2}$$

To explain some basic concepts of photoconduction figure 2.1 shows a simple case of a trap free semiconductor under a steady uniform illumination with photon energy greater than the band gap.

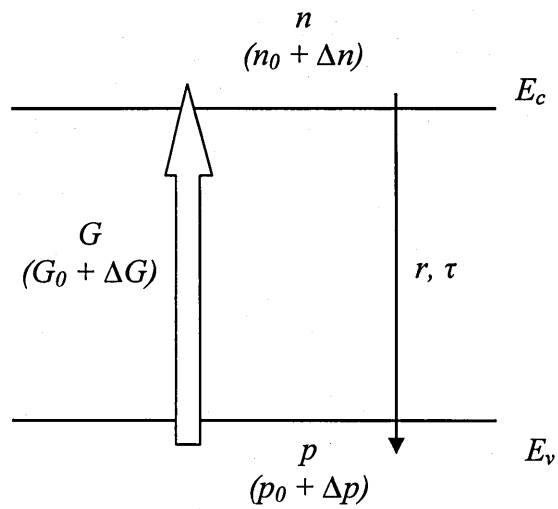

Figure 2.1 Electron transitions in a simple case of a trap free semiconductor.

In the following it is assumed that electrons are dominating the conduction. The illumination creates excess densities of free electrons and holes Δn, Δp at an optical (excess) generation rate ΔG above the thermal generation rate G_0. The free carriers recombine in a reverse process with the recombination rate r. The electron lifetime τ is the mean time the excess electrons spend in the extended states before they recombine and n_0 and p_0 are the thermodynamic equilibrium free carrier densities.

In the steady-state photoconductivity the generation and the recombination rates are equal so that

$$\Delta G = \Delta n / \tau \tag{2.3}$$

and the recombination rate is equal to

$$r = (n_0 + \Delta n)\,(p_0 + \Delta p)\,C_r = G_0 + \Delta G, \tag{2.4}$$

where C_r is the hole capture coefficient, which is the probability per second for an electron recombining with a given hole. The material is electrically neutral and trap free so that $n = p$, $n_0 = p_0$ and therefore $\Delta n = \Delta p$. The thermal generation rate $G_0 = n_0 p_0 C_r$. Substituting into equation 2.4 we obtain

$$\begin{aligned} r &= n_0 p_0 C_r + (2\Delta n\, n_0 + \Delta n^2)\, C_r \\ &= G_0 + \Delta G. \end{aligned} \tag{2.5}$$

In the case of a low $\Delta G << G_0$ and therefore $\Delta n << n_0$ we obtain for

$$\Delta n = \Delta G\,(2 n_0 C_r)^{-1}, \tag{2.6}$$

where Δn is proportional to ΔG, i.e. the probability of a single electron to recombine is determined by a fixed 'large' density of thermally generated holes. Because the recombination rate depends only on the excess density of one recombining species this is also referred as *monomolecular* recombination. By substituting equation 2.3 into 2.6 we obtain

$$\tau = (2 n_0 C_r)^{-1}, \tag{2.7}$$

where the recombination time is constant and independent of ΔG. In the opposite case where $\Delta G >> G_0$ and therefore $\Delta n >> n_0$ this gives

$$\Delta n = (\Delta G / C_r)^{1/2}, \tag{2.8}$$

the excess electron density changes with the square root of the excess generation rate. As a consequence the recombination rate depends on *both* densities of recombining species and is termed as *bimolecular* recombination. The recombination time depends on the excess generation rate and is given by

$$\tau = (\Delta G\, C_r)^{-1/2}, \tag{2.9}$$

so when the excess generation rate increases the recombination time decreases.

In amorphous semiconductors the recombination process is more likely to be capture by localized states in the gap, band tails or dangling bond defects acting as traps and/or recombination centres.

Traps are considered as localized states in the near band edges where free carriers are temporarily captured followed by thermal re-emission into the same band. Recombination centres are considered to be localized states in the mid gap where an electron capture into a localized state is directly followed by a hole capture into the same state. This is referred as *2-step* recombination according to the *Shockley-Read* mechanism (Shockley and Read, 1952). Note this is only one example of a variety of possible transitions via localized states. In figure 2.2 the Shockley-Read mechanism is illustrated for two separate transitions from the mobility edges.

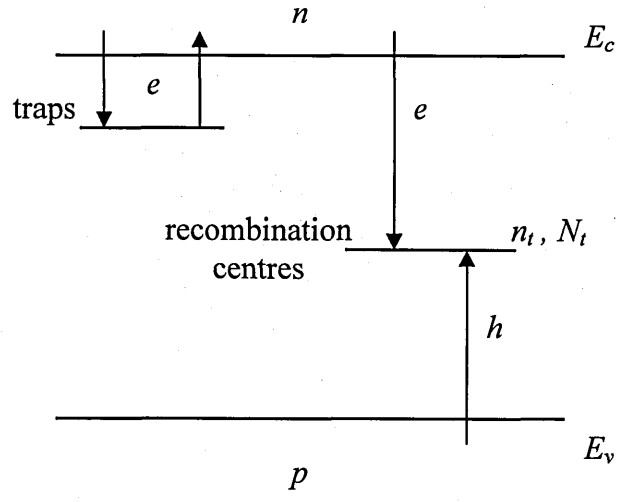

Figure 2.2 Shockley-Read mechanism showing for temporarily electron capture in traps near to the mobility edge and electron (hole) capture into localized states (recombination centres).

In the case of temporarily electron capture into a discrete trap at energy E_t with N_t the total density of traps, the probability of thermal re-emission can be obtained by the principle of *detailed balance* where, in thermal equilibrium, the capture and release rates are equal. So the

rate of capture of free electrons = rate of re-emission into the C-band

$$C_n n_0 N_t (1 - (f(E_t)) = e_n N_t f_0(E_t), \tag{2.10}$$

where C_n is the capture coefficient, n_0 is the equilibrium (dark) electron density, e_n is the thermal emission probability ($s^{-1}cm^{-3}$) and $f_0(E_t)$ which describes the *Fermi-Dirac* occupancy in a thermal equilibrium according to

$$f_0(E_t) = \frac{1}{1 + \exp(\frac{E_t - E_F}{kT})}, \tag{2.11}$$

where E_F is the *Fermi-energy* and all the localized states in the gap below this energy are occupied. Substituting equation 2.11 into 2.10 and with

$$n_0 = N_c \exp(-\frac{E_c - E_F}{kT}) \tag{2.12}$$

the result for the thermal emission coefficient is

$$e_n = C_n N_c \exp(-\frac{E_c - E_t}{kT}) = C_n \overline{n}\,. \tag{2.13}$$

This result is thus of the form of an *attempt to escape frequency* $v_n = C_n N_c$ multiplied by the probability to find the corresponding thermal energy to make the transition to E_c. Note that this approach 2.13 has been derived for 'one-electron' states.

In the next case we now consider a steady illumination of the semiconductor including a single electron level anywhere in the gap. Figure 2.3 shows all four transitions occurring via a given set of states.

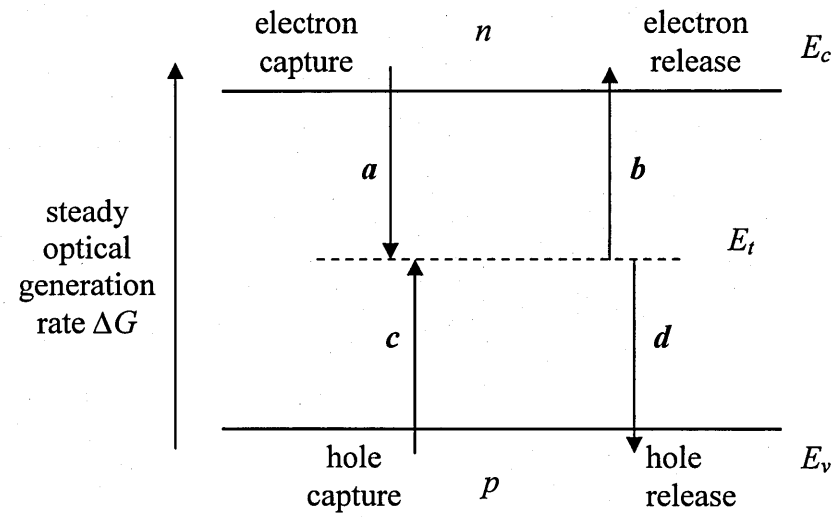

Figure 2.3 Electron (hole) capture and release into localized states during steady illumination.

In steady-state the sum of the rates (a) and (b) must be equal to (c) and (d). This leads to the rate equation

$$\frac{dn_t}{dt} = 0 = \quad a \quad - \quad b \quad - \quad c \quad + \quad d$$
$$= nC_n N_t[1 - f(E_t)] - \bar{n}C_n N_t f(E_t) - pC_p N_t f(E_t) + \bar{p}C_p N_t[1 - f(E_t)]. \tag{2.14}$$

The aim is to find an expression for the occupation function $f(E_t)$ which no longer follows the Fermi-Dirac statistics. After some rearrangement of equation 2.14 the occupation function can be written as

$$f(E_t) = \frac{nC_n + \bar{p}C_p}{C_n(n+\bar{n}) + C_p(p+\bar{p})}, \tag{2.15}$$

where $\bar{p}\,C_p = e_p$ and $\bar{n}\,C_n = e_n$ are the emission probabilities. Note that $f(E_t)$ is *independent* of N_t. Simmons and Taylor generalized this approach so that it is applicable to arbitrary *distribution* of states, too (Simmons and Taylor, 1971). The emission probabilities $\bar{p}\,C_p$ and $\bar{n}\,C_n$ generally fall off exponentially with greater energy distance from the band edges while the capture coefficients C_n and C_p are considered to be independent of (or less dependent on) energy depth.

The equation 2.15 enables determination as to whether a state is acting as an electron trap (or hole trap) or as a recombination centre. For traps the electron release is much greater than the capture rate for holes ($\overline{n}\, C_n >> \overline{p}\, C_p$) so that from equation 2.15

$$f(E_t) \approx \frac{n}{\overline{n}}, \tag{2.16}$$

the occupation of traps depends exponentially from depth E and is related to that of free states at E_c because $\overline{n}$ contains a *Boltzman* factor and hence it is temperature dependent.

At this point it is useful to define the *free electron quasi Fermi level* E_{Fn} to describe the increased electron density under illumination by

$$n = N_c \exp(-\frac{E_c - E_{Fn}}{kT}). \tag{2.17}$$

From (2.16) the occupation of *shallow* traps can be described by using the same quasi-Fermi level

$$n_t = N_t f(E_t) = N_t \exp(-\frac{E_t - E_{Fn}}{kT}). \tag{2.18}$$

If an electron is captured by a recombination centre it is more likely that it will capture a hole (recombine) than be re-emitted. With $\overline{p}\, C_p$; $\overline{n}\, C_n << nC_n$; pC_p the occupancy results in

$$f(E_t) \approx \frac{nC_n}{nC_n + pC_p}. \tag{2.19}$$

Considering the case of simple symmetry where $n = p$ and $C_n = C_p$, then $f(E_t)$ is equal to 0.5 i.e.: constant occupation. The occupation only depends on the capture terms not on energy or temperature, as in traps.

To describe the transition between a state acting as a trap or acting as a recombination centre a *trap quasi Fermi level* E_{Fn}^{t} (E_{Fp}^{t} for holes) is introduced which is general slightly above the free electron quasi Fermi level E_{Fn} and does not coincide with it.

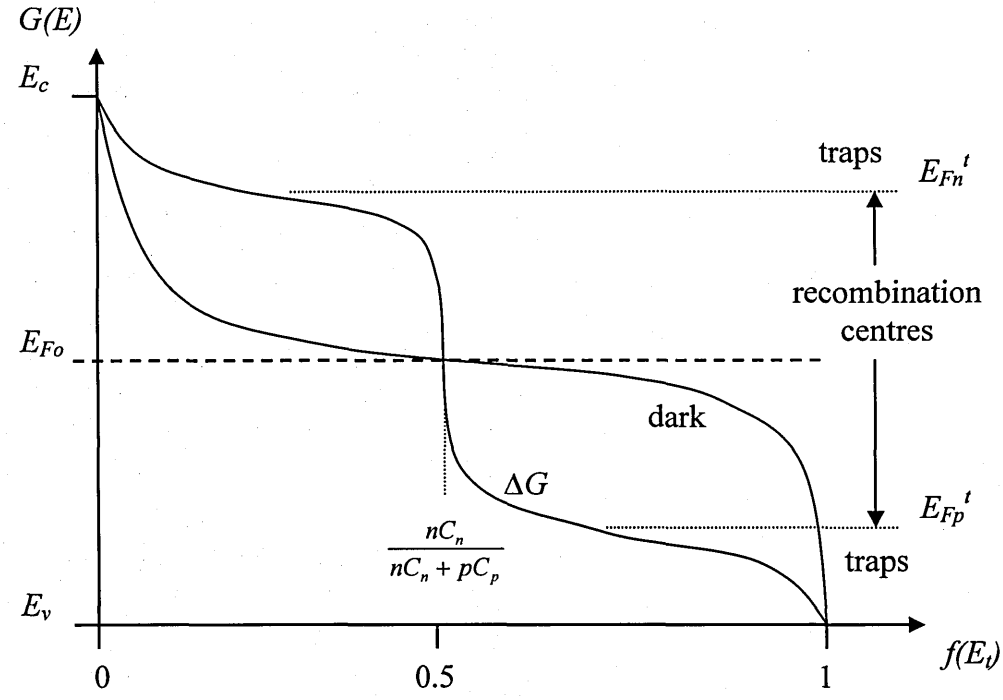

Figure 2.4 Occupation function for localized states in an amorphous semiconductor under illumination (Simmons and Taylor). Illustrated are the electron (hole) trap quasi Fermi levels E_{Fn}^{t} (E_{Fp}^{t}) which mark the transition between localized states acting as trap or as recombination centre.

In figure 2.4 the occupation function $f(E_t)$ is illustrated under dark conditions and under illumination which produces the excess generation rate ΔG. It is said that the dark Fermi level *splits* under illumination and with increasing excess generation rate ΔG the trap quasi Fermi levels move away from each other towards the mobility edges and an increasing amount of the gap states become recombination centres.

2.3 Sublinear excitation dependence – Rose factor

In chapter 2.2 monomolecular (equation 2.6) and bimolecular (equation 2.8) recombination was introduced where recombination depends either on one or both of the excess density of one recombining species. In frequently observed cases photoconductivity excitation dependence is found to be intermediate between monomolecular and bimolecular recombination and in many cases the following expression is used to describe this phenomenon

$$\Delta n \propto \Delta G^{\gamma} \text{ with } 0.5 < \gamma < 1 . \tag{2.20}$$

A simple model proposed by Rose (Rose 1963) is used to describe this dependency. When the excess generation rate ΔG increases Δn also increases which shifts the free electron quasi Fermi level E_{Fn} towards the trap quasi Fermi level E_{Fn}^{t} which are now assumed to be equal. The electron lifetime decreases as ΔG increases. Charge neutrality demands that the increased electron charge trapped below E_{Fn}^{t} is *balanced* by the increased hole occupation of the recombination centres. The occupancy is assumed to be *f(E)=1* below E_{Fn}^{t} and 0 above – i.e. a 'zero-temperature' approximation. The conduction band tail density has an assumed exponential form which is described by

$$g_c(E) = g_c(E_c)\exp(-\frac{E_c - E}{kT_c}) . \tag{2.21}$$

The occupied trap density can be calculated from

$$n_t = \int_{E_{F0}}^{E_{Fn}} g_c(E)dE . \tag{2.22}$$

Substitution of equation 2.21 into 2.22 and approximation results in

$$n_t = kT_c g_c(E_c)\left[\exp\left(-\frac{E_c - E_{Fn}}{kT}\right)\right]^{T/T_c} (= p_t \rightarrow \text{charge neutrality}). \tag{2.23}$$

Now substitution of equation 2.23 using

$$\Delta n = \Delta G \, \tau = \frac{\Delta G}{C_r p_t} = \frac{\Delta G}{C_r n_t} \tag{2.24}$$

and

$$\exp(-\frac{E_c - E_{Fn}}{kT}) = \frac{\Delta n}{N_c}\,, \tag{2.25}$$

results in following relationship between Δn and ΔG

$$\Delta n = \frac{\Delta G^{\left(\frac{T_c}{T_c+T}\right)}}{\left[C_r k T_c g_c(E_c) N_c^{-T/T_c}\right]^{\left(\frac{T_c}{T_c+T}\right)}}. \tag{2.26}$$

This approximation is valid for $0 < T < T_c$, and with $\gamma = T_c / (T_c + T)$ equation 2.26 can be expressed by equation 2.20. The exponent γ is often referred as the *Rose-Factor*.

In high quality a-Si:H material (undoped) where the band tail density is very low and E_{Fo} is above mid gap, γ is close to 1. In low quality material with extensive band tail densities and the majority of recombination occurs via band tails γ is between 0.5 and 1 → the Rose model applies.

2.4 Recombination via Dangling Bonds

Recombination via *Dangling Bonds* is more complex than for the above described 'one-electron' states by the Shockley-Read mechanism generalized by Simmons and Taylor for a distributed density of states where only two charge conditions were used. Recombination via Dangling Bonds uses three possible charge conditions – empty (D^+), singly occupied (D^0) and doubly occupied (D^-) (Okamoto et al, 1984, Main et al, 1987, 1991).

There are essentially two distinct paths for recombination via Dangling Bonds available as illustrated in figure 2.5.

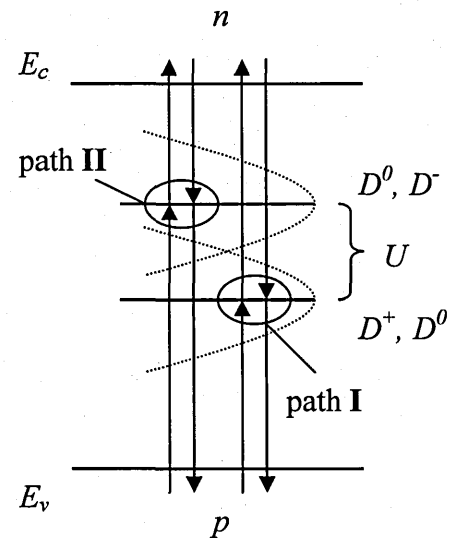

Figure 2.5 Transition diagram for the recombination via Dangling Bond showing the possible transitions for the three charge conditions D^0, D^+ and D^-.

path **I**: $e + D^+ \rightarrow D^0$ and $h + D^0 \rightarrow D^+$

path **II**: $e + D^0 \rightarrow D^-$ and $h + D^- \rightarrow D^0$

The occupation of the dangling bonds depends on the position of the Fermi level and hence also on the quasi-Fermi levels. Usually the position of the $D^{+/0}$ transition from path **I** is found to be slightly below the middle of the bandgap while the position of the $D^{0/-}$ transition from path **II** is above the mid gap. The energies of the D^0 state from path **I** is not the same from path **II** because of Coulomb interaction between the electrons of the singly occupied states. The energy difference between these two states is referred as the *correlation energy U* which is, in the case of a-Si:H, positive.

The correlation energy is defined as

$$U = q^2 / 4\pi\varepsilon\varepsilon_0 r - W, \tag{2.27}$$

where the first term describes the Coulomb interaction with q as the elementary charge, r the effective separation of the two electrons, and the second term arises from lattice relaxation energy at the defect which is described by W (Street, 1991, p100).

To describe the detection mechanism of the constant photocurrent method – CPM, the Shockley-Read mechanism generalized by Simmons and Taylor to the distributed density of states will be used.

2.5 Description of the Constant Photocurrent Method – CPM

The determination of the *absorption coefficient* $\alpha(E_{ph})$ (also referred to as the spectral distribution of photoionization cross section for electrons) from photoconductivity measurements can be described as follows (Grimmeis and Lebedo, 1975, Vaněček et al, 1981): Considering a single energy level E_t with the impurity density N_t in the upper half of the band gap $E_g=E_c - E_v$ of an n-type semiconductor, under steady-state conditions the concentration of photogenerated electrons Δn (assume that $\Delta n >> n_0$) is given by

$$\frac{d\Delta n}{dt} = e_n n_t - C_n(N_t - n_t)\Delta n = 0, \tag{2.28}$$

where e_n is the emission probability for electrons under the photon flux $\Phi(E_{ph})$, n_t is the density of trap levels N_t occupied by electrons and C_n the capture rate for electrons. The emission probability e_n can also be written as

$$e_n = \sigma_n(E_{ph})\ \Phi(E_{ph}), \tag{2.29}$$

where $\sigma_n(E_{ph})$ is the photoionization cross-section for electrons.

Substitution of 2.28 into 2.29 results in

$$\sigma_n(E_{ph})\Phi(E_{ph})n_t - C_n(N_t - n_t)\Delta n = 0. \quad (2.30)$$

This approach is only valid if the excitation is homogenous ($\alpha d << 1$), the thermal emission rate e_n^0 can be neglected and for photon energies $E_{ph} < E_t - E_v$ which excludes two-step excitation.

The equation 2.30 shows that the steady state photogenerated electron density Δn can be kept constant during the change of the photon energy E_{ph} by altering the photon flux $\Phi(E_{ph})$ of the exciting light. If there is no spectral dependence of the electron mobility of the photogenerated electrons, the photo current I_{ph} is constant. This means that also the density of photogenerated electrons is constant and therefore the occupancy of the gap-levels is kept unchanged which results in a constant electron lifetime τ.

For $\sigma_n(E_{ph}) = \alpha(E_{ph})$ and from equation 2.30 the density of the impurity ('defect') levels N_t can be obtained by

$$\alpha(E_{ph}) = const / \Phi(E_{ph}). \quad (2.31)$$

A simpler approach was used by Bube et al to describe the principle of CPM (Bube et al, 1992). In its simplest form the photoconductivity $\Delta\sigma$ can be expressed as

$$\Delta\sigma = \Delta n\, e\, \mu, \quad (2.32)$$

where μ is the electron mobility and e the elementary electron charge. From equation 2.3 and with $\Delta G = \alpha(E_{ph})\, \Phi(E_{ph})\eta(1-R)$ for $\alpha d << 1$, equation 2.32 can be rewritten as

$$\Delta\sigma = \alpha(E_{ph})\, \Phi(E_{ph})\eta(1-R)\, e\, \mu\, \tau, \quad (2.33)$$

where η is the quantum efficiency and R is the reflectivity between the sample surface and the air and is assumed not to change with photon energy. By keeping the photo current constant $\Delta\sigma$, μ, τ are also constant and equation 2.33 becomes 2.31.

The photoconductivity $\Delta\sigma$ is connected to the generation rate ΔG as

$$\Delta\sigma \propto G^{\gamma} \text{ with } 0.5 < \gamma < 1, \tag{2.34}$$

where γ is the Rose factor (see chapter 2.3). Bube et al showed that the inverse relation between N_t and $\Phi(E_{ph})$ does not require a linear dependence of $\Delta\sigma$ and ΔG provided γ is not a function of photon energy. Mettler et al introduced the concept of the CPM *working point* by making the first DC-conductivity measurements as a function of the generation rate at different photon energies to investigate the spectral dependence of γ (Mettler et al, 1993, 1994, Mettler 1994).

2.6 The CPM spectrum

A standard CPM spectrum is illustrated in figure 2.6 showing the relative inverse photon flux plotted against the photon energy. The spectrum is divided in three sections corresponding to the transitions detectable by CPM in figure 2.7.

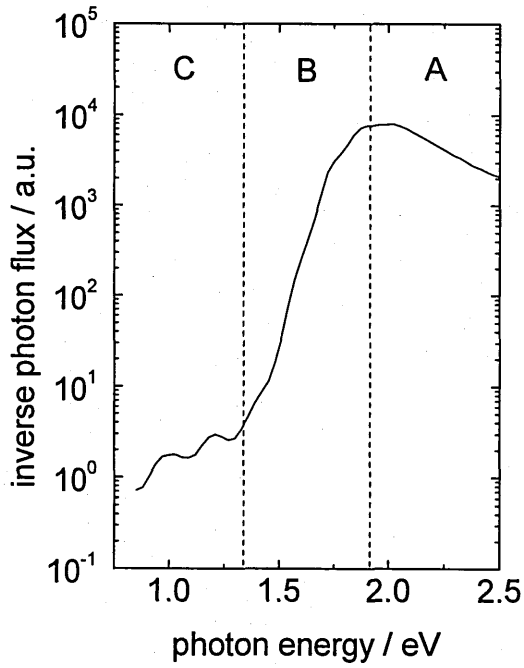

Figure 2.6 A standard CPM spectrum showing the inverse photon flux against the photon energy in a log-linear scale. Sections A, B and C showing areas of different transition types depending on the photon energy.

Note that in the standard approach reported in the literature, only transitions which bring an electron above E_c are being detected by the CPM method (contributing to the photocurrent I_{ph}, but this thesis, Chapter 4 shows that other transitions may be important too).

In the section *A* of the CPM spectrum, shown in figure 2.7 the CPM curve is in saturation because $\alpha d \geq 1$. This means the excitation is not homogenous because the generation rate falls exponentially and significantly with increasing depth into the sample (i.e. surface absorption). The transitions occurring in this regime are mostly band-band transitions because of $E_{ph} > E_g$ but because of the CPM curve being in saturation other measurement methods (i.e. optical transmittance) need to be used to obtain the real $\alpha(E_{ph})$ in this region.

Section *B* shows a steep exponential decay in the spectrum which is generated by transitions from valence band into conduction band tail states and from valence band tail states into the conduction band.

Section *C* shows the defect tail of the CPM spectrum, the transitions here are mainly occurring from the valence-band into the defect tails around mid-gap and above the Fermi-level and from defect tails just below the Fermi-level into the conduction band. Transitions from occupied defect states below Fermi-level into empty defect states above Fermi-level are not detectable because the probability is too small.

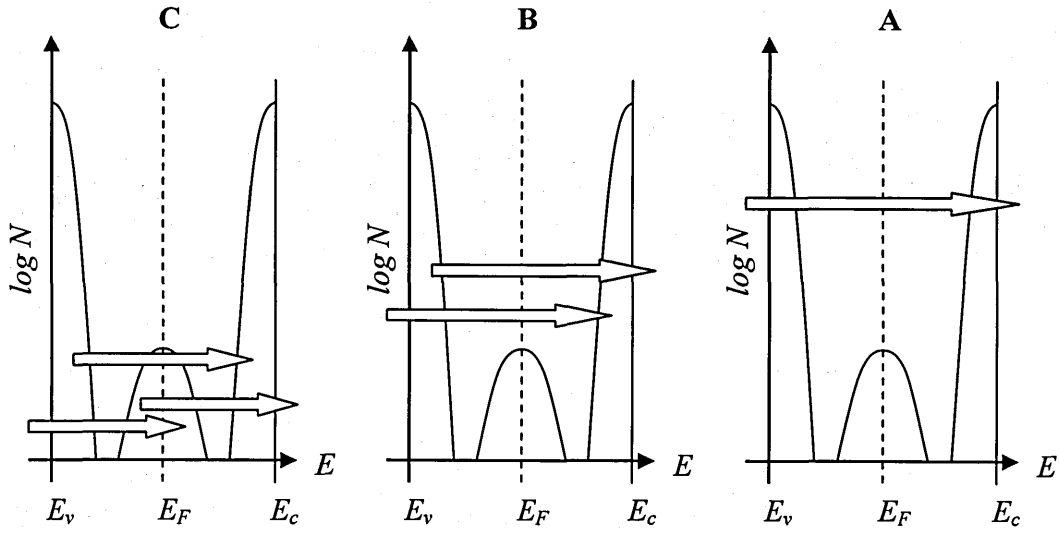

Figure 2.7 Possible optical transitions occurring in a CPM measurement when varying the photon energy. The transition types are described in the text above.

2.7 The absolute $\alpha(E_{ph})$ spectrum – absolute CPM

In the previous section figure 2.6 a CPM spectrum was shown, where the relative inverse photon flux was plotted against the photon energy. To measure an absolute absorption coefficient spectrum it requires knowledge of the exact value for the constant in equation 2.31. To scale the measured standard CPM spectrum to an absolute scale, separate measurements on the high energy side of $\alpha(E_{ph})$ like transmittance and reflectance need to be used. In some cases even the calculation of $\alpha(E_{ph})$ at one photon energy at the high energy side (1.7 eV – 1.8 eV) is sufficient enough to scale the CPM spectrum to an absolute scale but this is not a very precise method to use especially if the CPM measurement shows interference fringes as illustrated in the defect tail of figure 2.6.

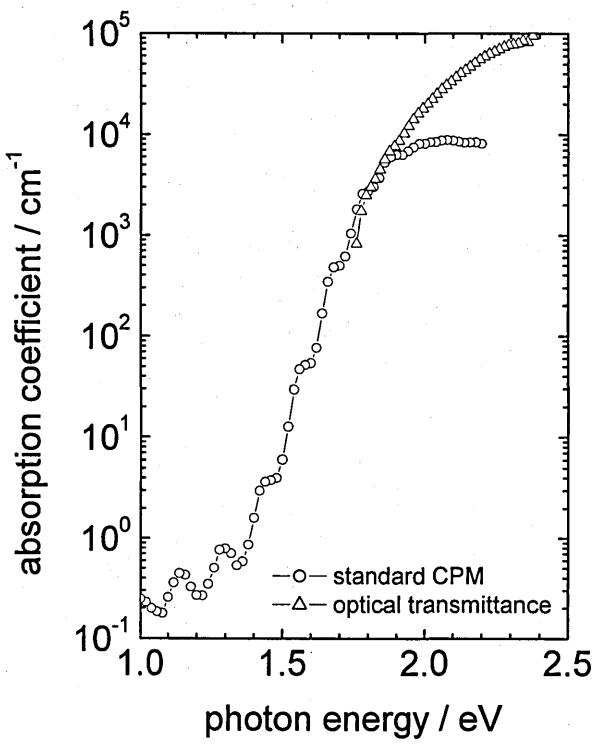

Figure 2.8 Example of scaling a standard CPM spectrum to absolute scale by using the absolute absorption coefficient calculated from optical transmittance measurement.

Vaněček et al developed a new way to obtain the absolute $\alpha(E_{ph})$ directly from the CPM measurement. Based on the work of Ritter and Weiser (Ritter and Weiser, 1986) and Sasaki et al (Sasaki et al, 1994) they called this new method the *absolute CPM technique*

(Vaněček et al, 1995, Feifar et al, 1996). Ritter and Weiser developed a method to minimise interference fringes in calculations of α from absorption measurements on thin films. The result is know as the Ritter-Weiser-Equation

$$\alpha(E_{ph})\, d = ln0.5\{(1-R_2)(1+A/T)+[(1-R_2)^2(1+A/T)^2+4R_2]^{1/2}\}, \qquad (2.35)$$

where d the thickness of the film, R_2 is the reflectivity of the back interface of the film, A the absorptance, and T the transmittance of the film.

Sasaki et al suggested measuring the CPM spectrum in *transmission mode* by placing the detector measuring the photon flux behind the sample to suppress interference fringes in the measured CPM spectrum (Sasaki et al, 1994). While measuring the CPM spectrum in transmission mode the shape of the signal is proportional to the absorptance to transmittance ratio A/T. The resulting 'transmission-CPM' (T-CPM) spectrum needs to be normalized to a reference photon energy where the transmittance of the sample is chosen to be, say 5 % because the absorption in this region ($\alpha d>1$) is high enough to suppress interference fringes. At this reference photon energy the value for A/T is thus 13.8. The value of R_2 is 0.21 which is assumed to be constant (spectrally independent). Using the equation 2.35 and knowing the thickness of the sample the absolute absorption coefficient can be calculated. In figure 2.9 the comparison between the results from the Vaněček at al method and the results from optical transmittance are illustrated. The agreement between both measurements is very good. There is a noticeable suppression of the inference fringes visible when compared with figure 2.8.

The author would like to point out that in the present work, more comparison measurements were performed and as a result the absolute CPM method was mainly used in this thesis.

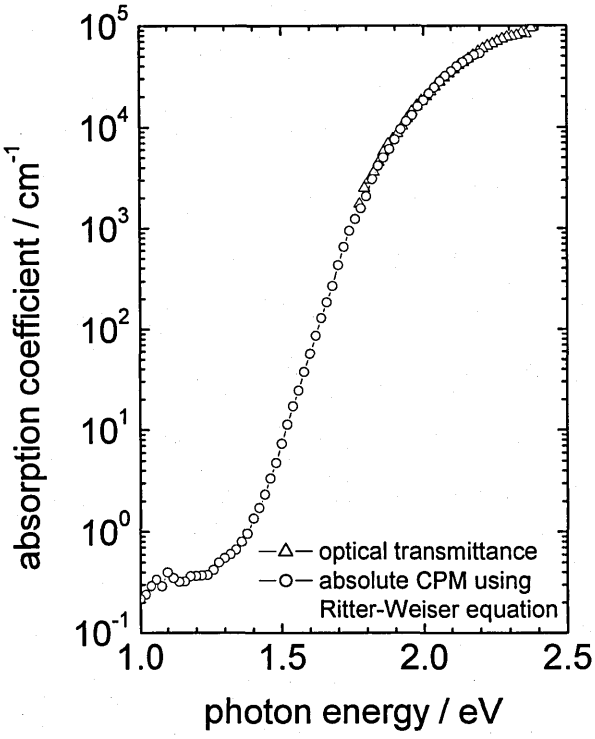

Figure 2.9 Absorption coefficient spectra showing a comparison between the new absolute CPM method by Vaněček at al and $\alpha(E_{ph})$ calculated from optical transmittance. There is a very good agreement between $\alpha(E_{ph})$ from transmittance and from absolute CPM. Also the suppression of the interference fringes is noticeable.

2.8 The relationship between $\alpha(E_{ph})$ and the density of states – DOS

The density of states – DOS of a-Si:H material is of great interest because it directly provides information about the quality of the a-Si:H material. The CPM spectrum gives indirect information about the distribution of the DOS in the vicinity of the valence band tail.

A simple method to obtain the DOS from a CPM spectrum was presented by Hata and Wagner (Hata and Wagner, 1991) based on Pierz et al (Pierz et al, 1985) using differentiation of $\alpha(E_{ph})$ over $E_{ph} = E_c - E$ as

$$N(E)f(E) = \left[\frac{d\alpha}{dE_{ph}}\right]_{E_{ph}=E_c-E}, \tag{2.36}$$

where *N(E)* the density of states and *f(E)* is the occupation function. An enhancement to the method of Hata and Wagner was introduced by Marshall et al (Marshall et al, 1991) with the assumption of an exponential valence band tails and a Gaussian distribution of the mid gap states. Poruba and Schauer (Poruba and Schauer, 1994) developed an iterative method based on the standard derivative method (Marshall et al, 1991).

The method of Pablo Jensen (Pablo Jensen 1990) claims to calculate the DOS directly from CPM spectrum without the need to use an iterative way to model a chosen DOS to get a good agreement (Kočka et al, 1987). The relationship between the spectral dependence of the absorption coefficient and the DOS is given by the convolution integral of the initial density of states within the gap g_v and the final density of states g_c above E_c so $\alpha(E_{ph})$ can be written as

$$\alpha(E_{ph}) = \frac{C}{E_{ph}} \int_{E_c - E_{ph}}^{\infty} g_v(E) f(E) g_c(E + E_{ph}) \times [1 - f(E + E_{ph})] dE , \qquad (2.37)$$

where C is a constant and equal to 4.34×10^{-38} cm^5 eV^2, f the occupancy and E_{ph} the photon energy. For $G_v(E) = g_v(E)f(E)$ -the density of filled states - equation 2.37 transforms into

$$G_v(E_c - E_{ph}) = \frac{1}{g_c(E_c)} \frac{dA}{dE_{ph}}(E_{ph}) - \frac{1}{g_c(E_c)} \int_{E_c - E_{ph}}^{\infty} G_v(E) \frac{\partial g_c}{\partial E}(E + E_{ph}) dE , \qquad (2.38)$$

where $A(E_{ph}) = (1/C)E_{ph}\,\alpha(E_{ph})$, already given by the CPM experiment and $g_c(E) = 8.05 \times 10^{21}(E - E_c + 0.2)^{1/2}$ cm^{-3} eV^{-1} i.e. assumed to vary as $E^{1/2}$ close to E_c (Pablo Jensen 1990).

Chapter 3 - CPM – Experimental setup

3.1 Overview

A major advantage of CPM is its relatively easy setup. The basic layout consists of a monochromatic light source, an optical arrangement to focus the probe beam onto the sample, an ammeter for monitoring the photocurrent of the sample and a detection and monitoring device for the photon flux in a feedback loop with the ammeter to keep the photocurrent constant and of course a photoconductive sample.

The majority of groups (Sasaki et al, 1994, Vaněček et al, 1995, Bube et al, 1992, Mettler 1995) describe in their work a similar setup which only differs slightly, in the arrangement, the detection devices and monochromatic light sources used. In this thesis the basic CPM setup follows the experimental description of Vaněček at al (Vaněček et al, 1995) which provides the possibility to perform standard and absolute CPM in the same setup. The next chapter describes the actual CPM setup used in this thesis followed by the experimental procedure and controlling software performing the measurement. Following this, some details will be given explaining the measurement mode in AC and DC and the consequences, investigated in this project, for the CPM spectrum.

3.2 Experimental setup

A schematic description of the CPM setup is illustrated in figure 3.1 which shows the *standard CPM* layout. The monochromatic light source consists of a 75 W halogen lamp connected to a software controlled power supply from a 'TTi' model 'TSX 3510P' and a software controlled double monochromator from 'Jobin-Yvon' model 'SPEX DH10' with two 600 g/mm mirror-gratings covering the wavelength range from 400 nm (3.1 eV) up to 1600 nm (0.775 eV). The entrance slit has a width of 2.5 mm (for maximum light input) and the exit slit of 1 mm which results in a dispersion of 8 nm/mm. The focal length is 100 mm and the aperture is f/3.5 for this device.

To eliminate monochromatic light of 2nd and higher orders edge filter were used in a filter wheel placed at the exit of the monochromator. The edge filters were moved into the probe beam at the following wavelength positions: at 540 nm (RG490), at 750 nm (RG750), at 850 nm (RG850) and at 1350 nm (RG1000). From 400 nm to 540 nm no edge filter was used.

The standard CPM setup was operated in AC mode, in which case a 'Scitec B640' chopper wheel was placed immediately after the monochromator (see next sub-section for explanation) running at a frequency of 5 Hz.

A biconvex lens with 25 mm focal length was used to focus the probe beam onto the sample. The glass material of the lens, and hence the focal length, had no significant spectral dependence (chromatic variation) in the wavelength range of interest. To avoid imaging the filament shape from the halogen lamp on the sample the probe beam was defocused to achieve homogeneous illumination.

A beam splitter made out of quartz glass (for spectral dependence reasons) was placed between the lens and the sample to redirect a small part of the probe beam towards the detector measuring the magnitude of the photon flux. The detection device for the photon flux consists of a 'Hamamatsu' two-colour SiGe detector and a 'Standford Research' lock in amplifier model 'SR530' remote controlled by software.

The sample was placed in an 'Oxford Optisat' cryostat for temperature dependent CPM measurements. A Brandenburg model '477' high voltage power supply was used to create the electric field between the sample's coplanar contacts. The sample photocurrent was measured by a digital DSP lock in amplifier model 'EG&G 7260' also remote controlled by software.

The CPM measurement procedure was controlled by software which was written in a special program language called TestPoint® version 3.0 for Windows. The measurement devices were connected via GPIB (IEEE488) to an 'IOTech 488' GBIP ISA card installed in an Intel Pentium 133 MHz PC running Microsoft® Windows 98 Second Edition.

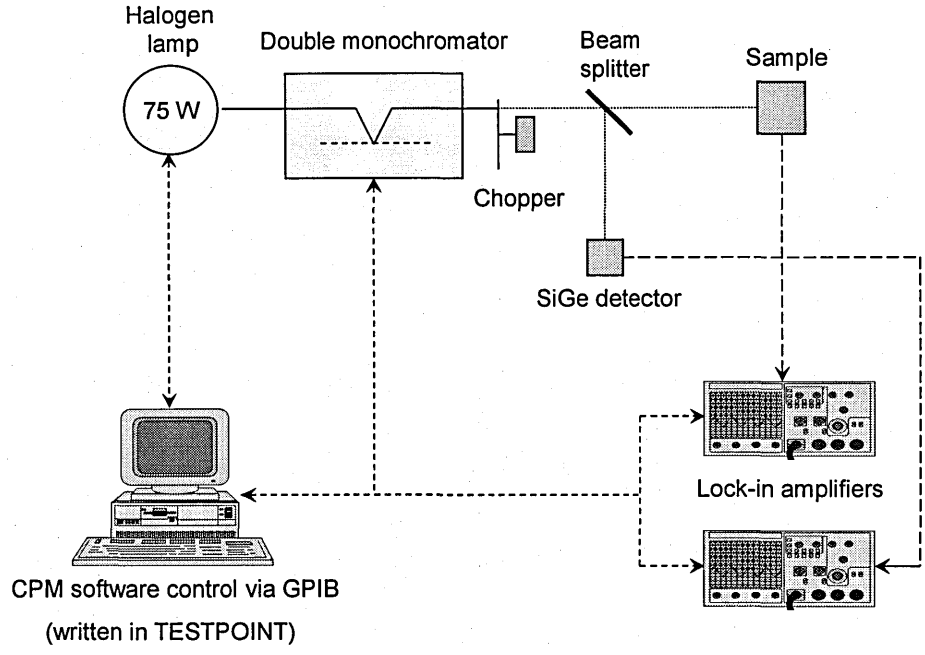

Figure 3.1 A schematic diagram for the *standard* CPM experimental setup.

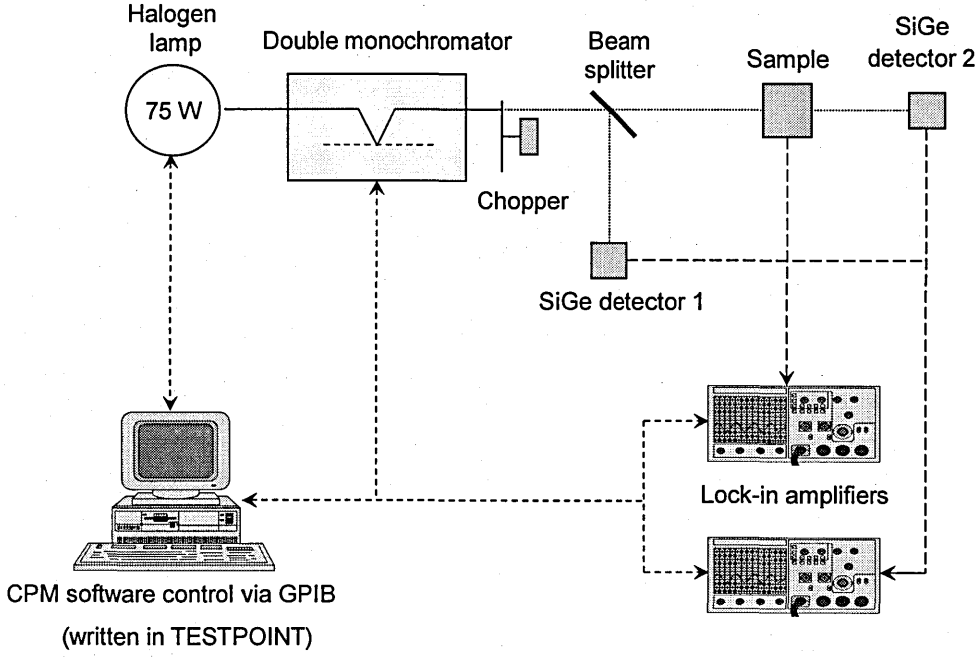

Figure 3.2 A schematic diagram for the *transmission* CPM experimental setup. The difference in comparison with figure 3.1 lies in the second detector behind the sample which measures the transmitted light through the sample.

The transmission CPM (also referred to as absolute CPM) experimental setup is illustrated schematically in figure 3.2. Actually it is nearly identical to the standard CPM setup except there is a second SiGe detector placed behind the sample, which measures the transmitted photon flux through the sample. This detector connects to the SR530 lock in amplifier too. Both detectors were operated in short circuit mode, to minimise current noise.

Both experimental setup versions were calibrated using a pyroelectric detector from 'Scitec' - model 'P2613M-06' with built-in pre-amplifier. The response of a pyroelectric detector is sensitive to the incident radiation power and not the number of absorbed photons. This fact allows calibration of a spectrally dependent detector like the SiGe detectors to measure the true photon flux $\Phi(E_{ph})$ of the probe beam at all wavelengths. It would have been a possibility to use pyroelectric detectors for CPM measurement also, but due to their slow response and lower sensitivity we decided to use the SiGe detectors instead.

In the case of standard CPM (figure 3.1) the system was calibrated by placing the pyroelectric detector at the sample's position and obtaining the ratio between SiGe detector and the pyroelectric detector which was then incorporated into the controlling software as baseline. In the case of transmission CPM (figure 3.2) the pyroelectric detector was placed at the position of "SiGe detector 2" where a baseline was obtained different from the previous one. The calibration procedure was repeated several times to ensure reliable measurement conditions.

The transmission CPM setup allowed 2-beam optical transmittance measurements as well where "SiGe detector 1" was measuring the reference light and "SiGe detector 2" measured the transmitted light. The ratio of transmitted/reference light gives the transmittance spectrum.

3.3 The CPM measurement procedure

The aim of the CPM measurement is to keep the photocurrent of the sample constant by altering the intensity of the incident light for all photon energies. In order to do so first of all a sample photocurrent value has to be selected before the measurement begins. This is actually a process which is more related to experience with previous CPM measurements and sample qualities than like a fail-proof method. Note the following descriptions are the same for standard and transmission CPM.

The actual CPM setup has an upper and a lower limit for the photon flux it can provide. The upper limit is set by the maximum power of the halogen lamp and the lower limit is set by the lowest stable lamp power possible within the limits of the control system. At the beginning it is advisable to measure the photocurrent of the sample at a high photon energy where $E_{ph} > E_g$ with approx. 40 % of the possible lamp power and then scan to a low photon energy at about 1 eV or as far as a photocurrent is detectable and measures the photocurrent at maximum lamp power. These results give a first indication of the photocurrent's photon flux dependency over the photon energy range of interest.

Ideally, the measurement would involve setting an initial photocurrent I_{CPM} at high photon energies, and then progressively increasing the lamp power, and hence photon flux, as the photon energy is reduced, keeping I_{CPM} constant all the way through. In practice, this was not possible, since for suitably measurable I_{CPM} values, prohibitively high lamp power would be needed at low photon energies.

Thus, the CPM measurements have always been started at a high photon energy where $E_{ph} > E_g$ with a initial *CPM photocurrent* I_{CPM} at about 40 % of the lamp power and have been finished at lower photon energy when either the lowest practically measurable I_{CPM} has required the maximum photon flux possible from the equipment, and/or the specified end photon energy position of the measurement has been reached. For the majority of samples measured for this thesis, the strategy adopted was to change I_{CPM} in overlapping ranges, several times during a CPM measurement so as to reach the lowest $\alpha(E_{ph})$ possible.

How often the I_{CPM} needed to be changed was very much dependent on the quality and type of the sample. When the initial I_{CPM} reached the maximum possible photon flux $\Phi(E_{ph})$ at the photon energy E_{ph} the measurement was paused and rolled back for four increments of ΔE_{ph}. A new value for I_{CPM} was setup which necessarily must be lower in value than that previously used and the measurement continued until the maximum $\Phi(E_{ph})$

has been reached again and/or the measurement reached its specified final point (see also Sladek et al, 1995). Special software was written in Testpoint® which to control the measurement loop. The measurement routine is shown in figure 3.3 as a simple schematic flow chart diagram.

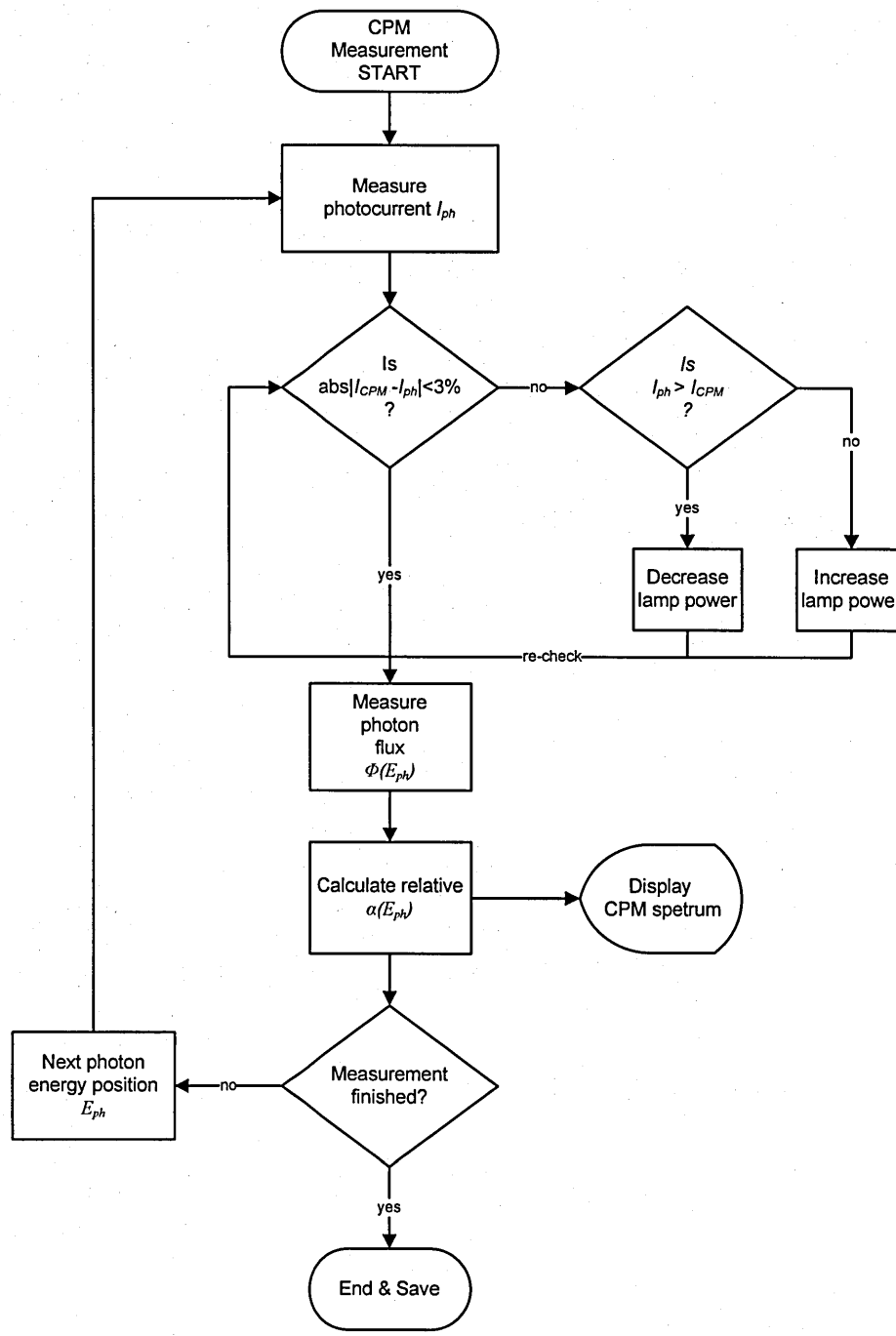

Figure 3.3 A schematic flow chart diagram explaining the measurement routine of the CPM software written in Testpoint®.

The measurement routine works as follows: At the beginning of the CPM measurement the program needs to be setup with the values for I_{CPM} which will be kept constant during the measurement, the photon energy increment (e.g. 0.03 eV), the measurement tolerance in I_{CPM} which sets limits between which the measured photocurrent I_{ph} is close enough to I_{CPM} to be regarded as constant, i.e. 5 % (it is impossible to match the exact value of I_{CPM} because of signal noise otherwise the measurement loop would run indefinitely), the accuracy for the detector signal response, i.e 0.5 %, the start position and the end position of the photon energy range to be measured and whether it is a standard CPM or a transmission CPM measurement being performed.

Once the measurement has started it will first measure the photocurrent of the sample and compare it with the preset required I_{CPM}. If its value is greater then I_{CPM}, the lamp power will be decreased using a proportional algorithm, while if it is smaller the lamp power will be increased. After each change to the intensity of the probe beam the photocurrent will be checked again until it is within its given tolerance range.

If the next step after the condition "abs ($I_{CPM} - I_{ph}$) < 5 %" is true the photocurrent of the SiGe detector is measured which gives the magnitude of the photon flux required to keep the sample photocurrent constant. The next step calculates the relative $\alpha(E_{ph})$ which is plotted in a window. If the measurement did not reach the end condition the loop will be entered again unless the user cancels the CPM measurement.
The data were stored in an ASCII file and were process and analysed using the software application OriginLab Origin® for windows.

The time duration for a single CPM measurement was dependent very much on the quality of the sample – i.e. the photosensitivity, as determined by the $\mu\tau$ product. On average a CPM measurement took about 60 minutes for a good quality sample in a photon energy range from 2.5 eV up to 0.8 eV with an increment of 0.03 eV.

The above description is of the CPM measurement process in AC mode (with modulated light) but it is also possible to perform CPM in DC mode (steady illumination). The arrangement for the DC CPM setup is nearly the same as for standard AC CPM (see figure 3.1). The difference lies in the measuring devices for the sample's photocurrent. In DC mode CPM the chopper wheel was placed in front of the SiGe detector which measured only the photon flux in AC mode (for sensitivity reasons) and the sample's dark and DC photocurrent was measured by using a "Keithley 617" electrometer. The

measurement was performed manually without the assistance of the software's lamp power adjustments routine and only for standard CPM.

So what is the reason to perform the CPM measurement in AC or in DC mode? According to Bube et al (Bube et al, 1992) there is always the possibility of photon energy dependent time constant effects when performing CPM in AC mode if the photoconductivity time constant is longer than the reciprocal of the AC chopper frequency, which might lead to errors in the CPM-determined defect density. As a result if the frequency used in AC mode is chosen too high the occupancy of the defect states is not constant anymore and the CPM method – in the form outlined earlier in this chapter - does not apply. As a solution it was suggested to use either low chopper frequencies (i.e. 5 Hz) or to do CPM in DC mode. *Note that the present thesis explicitly addresses such concerns and provides an alternative view – see chapter 4.*

CPM measurements in DC mode are very limited by the dark/photo - current ratio of the sample. It is necessary for the photocurrent to be of the same order as, or greater than the dark current under illumination. In poor material this causes great difficulty, with achievable DC photocurrents very much lower than dark currents, so that only an AC CPM could be used as a solution. On the other hand measurement results from DC-CPM compared with AC-CPM can show a significant discrepancy of up to 1.5 orders of magnitude in the mid-gap of the CPM spectrum. Previous authors would dismiss the AC measurements for reasons given above, leaving one with a difficult measurement situation.

However, in the present work, this problem has been tackled 'head-on'. In this thesis both CPM measurement modes were been used and analysed and some crucial insights have been gained about the discrepancy between the AC and DC CPM which lead to a new point of view about which is the 'correct type' of measurement mode which will be discussed in chapter 4, 5 and 6.

3.4 Summary

The experimental setup of standard and transmission (absolute) CPM differs only by one additional SiGe detector, which was placed in the transmission CPM setup behind the sample measuring the transmitted photon flux. The CPM measurement procedure (both types) is in principle a feedback loop (see figure 3.3) between the lock in amplifier

measuring the photocurrent of the sample, which is kept constant, and the lock in amplifier measuring the photocurrent of the calibrated detector (before and/or after the sample), which is proportional to the photon flux. To keep the photocurrent constant the size of the photon flux is altered by varying the power of the halogen lamp for each wavelength (photon energy) step. The measurement loop was controlled by special software written in Testpoint® and was performed in AC mode at 5 Hz modulation frequency whilst the DC CPM measurement was performed manually (no software support). By comparing the results from DC and AC CPM a significant discrepancy of up to 1.5 orders of magnitude in the mid-gap of the CPM spectrum was discovered which led to a more precise investigation presented in the following chapters.

Chapter 4 - New insights into AC & DC-CPM discrepancy

4.1 Introduction

CPM measurements have been performed in AC and in DC mode on a-Si:H samples produced by both PECVD and HWCVD deposition techniques, showing in each case a clear discrepancy in the absorption spectrum obtained by AC and DC methods. The difference is up to 1.5 orders of magnitude for photon energies $E_{ph} < 1.4$ eV, i.e. below the Urbach tail, where the DC mode consequently returns the higher value. A typical example is illustrated in figure 4.1.

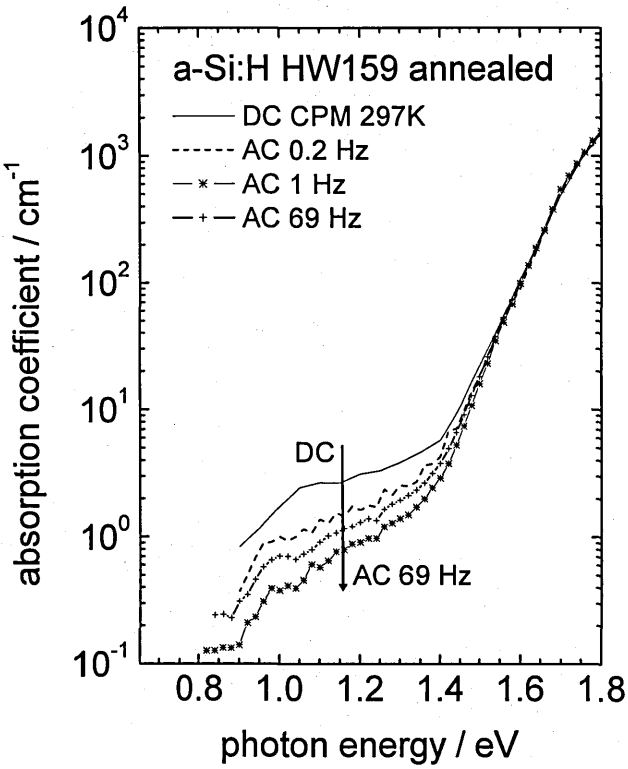

Figure 4.1 Measured DC and AC CPM for annealed HWCVD sample at 297K. The DC value exceeds the high frequency AC value at 1 eV by a factor of 6.

Similar discrepancies have indeed been already reported by several groups. Conte et al (Conte et al, 1993) noted the difference without explanation. Sladèk and Thèye (Sladèk and Thèye, 1993) note that the response time of the photocurrent reduces with E_{ph}, so that maintaining constant AC photocurrent conditions, requires increasing photon flux, hence

returning lower values for absorption coefficient. This is explained as resulting from changes in recombination efficiency arising from the different occupancy statistics of deep states for super- and sub-gap excitation. Similar results are also reported by Mettler where the AC mode shows up to 25% lower results than the DC mode (Mettler, PhD thesis 1995). In explanation he assumes a spectrally dependent response time which affects the occupation of the deep defect levels as reported and suggested already by Bube et al (Bube at al, 1990). Schmidt et al reported a photon energy dependence of the electron lifetime which affects the DC CPM spectrum in the mid gap and leads to underestimation of the true absorption coefficient in this region (Schmidt et al, 2000). Hasegawa et al report a *two order of magnitude* discrepancy in defect absorption between DC and AC methods, and also noted that this resulted from an increase in response time for low values of E_{ph} (Hasegawa et al, 1996). One possible explanation is briefly mentioned, involving, *incorrectly*, optical transitions from deep electronic states. It is evident that these authors meant thermal transitions.

The author concurs that the AC-DC discrepancy is associated with a wavelength-dependent response time, and figure 4.2 demonstrates the difference in response to square-wave excitation observed in the experiments, for super- and sub-gap excitation. The explanation of the origin of this effect, developed and presented in the present work, differs from that of Sladèk and Thèye and, whilst agreeing with the largely empirical observation by Hasegawa et al, is a novel and original development. In essence, the explanation presented here uses those thermal transitions usually ignored in previous analyses of CPM!

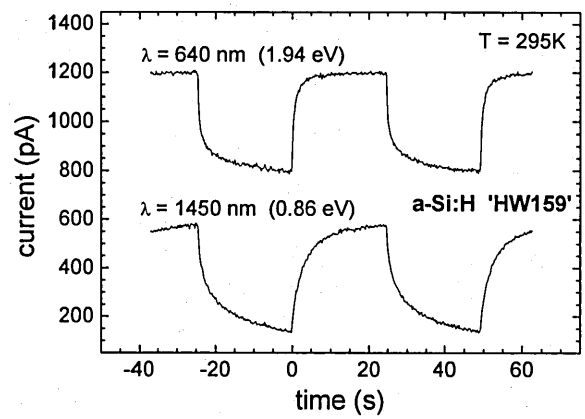

Figure 4.2 Photocurrent response of same HWCVD sample to chopped excitation at 640 nm (super-gap) and 1450 nm (sub-gap), showing slower response at longer wavelength (Note the graphs were separated vertically for clarity).

In a different context, that of Modulated Photoconductivity (MPC), such transitions have been included in DC and AC analyses by several authors (Oheda, 1980, Abe et al, 1988, Naito, 1996) without completing the link to the CPM DC-AC discrepancy. The transitions in question entail optical excitation from valence band or valence band tail states, into unoccupied defect states, with subsequent thermal emission to the conduction band, this latter transition producing a delay in the response, depending on the depth of the state. Such transitions are usually discounted in CPM studies for several reasons (Wyrsch et al, 1991); the initial optical excitation does not produce a free electron; any free holes produced have a low mobility. In this thesis this possibility will be included in the analysis, and allow for it in experiment by using low excitation rates such that quasi-Fermi level splitting is minimal, so that thermal emission from deep states is a probable process when compared with recombination.

At this point the author would like to acknowledge the contribution from Charlie Main, Steve Reynolds and Amar Merazga in validating this new theory describing the DC-AC discrepancy, which has resulted to date in three publications (Main et al, 2003, 2003a, 2004).

4.2 Theory

4.2.1 Sub-gap AC CPM – Simple analysis for single level

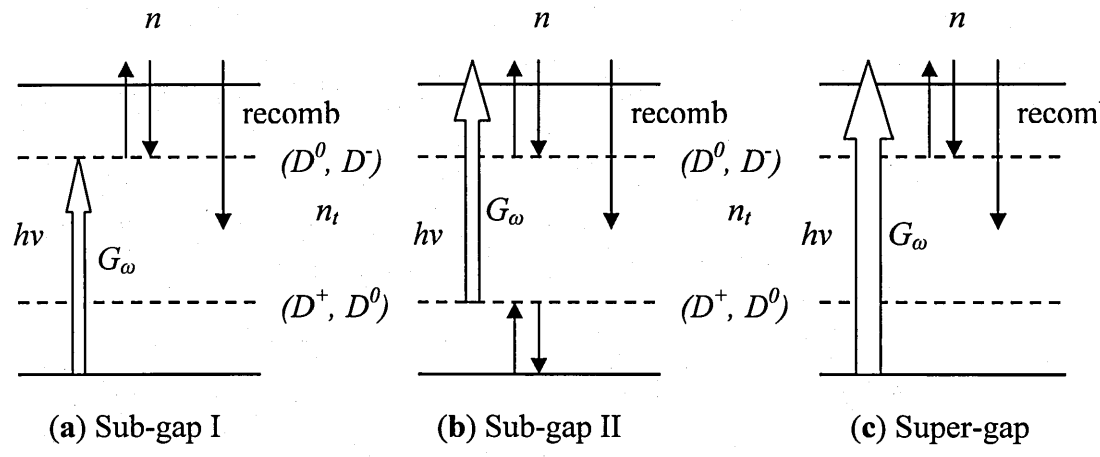

Figure 4.3 Energy level scheme for the analysis of sub-gap (a & b) and super-gap (c) excitation. Optical and thermal transitions are shown for three levels.

We wish to examine the frequency response of the free electron density n to AC excitation G_ω – i.e. optical excitation modulated at frequency ω, in the three cases shown in figure 4.3.

Case (**a**) Sub-gap optical excitation generated by transition from the valence band to D^0 state, followed by (slow) thermal emission from D^- into conduction band.

Case (**b**) Sub-gap optical excitation direct from D^0 state into conduction band.

Case (**c**) Super-gap band to band optical excitation.

Note in this analysis only defect states are shown. Other states (tail, etc.) will be included later. Case (a) and case (b) are two possible alternative paths, shown in figure 4.3, which may occur simultaneously, for low energy excitation. Case (c) is the 'standard' MPC super-gap excitation. In all cases low level excitation is considered, so that the state occupancies are not significantly perturbed. The contribution made by free holes is neglected. It follows that case (b) and case (c) are equivalent, as far as free electron frequency response is concerned. The AC component of the generation rate in each case is termed as G_ω but this will differ in detail between the different cases.

From case (a) the rate equation for free electron density $n(\omega)$ for sub-gap transitions maybe written as

$$\frac{dn(\omega)}{dt} = -\frac{dn_t(\omega)}{dt} - \omega_r n(\omega) \tag{4.1}$$

and for the trapped electrons

$$\frac{dn_t(\omega)}{dt} = -\omega_e n_t(\omega) + \omega_t n(\omega) + G_\omega \tag{4.2}$$

where $n_t(\omega)$ is the trapped electron density as a function of the frequency ω, and ω_t, ω_e, ω_r are the characteristic trapping and emission frequencies and a recombination frequency (equal to the inverse lifetime) respectively.

We expect solutions of the form $n(\omega) \propto exp[j(\omega t+\varphi)]$ and $n_t(\omega) \propto exp[j(\omega t+\varphi_t)]$ which allows us to substitute in equation 4.1 and 4.2 as follows,

$$\frac{dn(\omega)}{dt} = j\omega n, \qquad \frac{dn_t(\omega)}{dt} = j\omega n_t . \tag{4.3}$$

Substituting equation 4.3 into equation 4.1 and 4.2 results in

$$j\omega n = -j\omega n_t - \omega_r n + G_\omega \tag{4.4}$$

and

$$j\omega n_t = \omega_t n - \omega_e n_t . \tag{4.5}$$

From equation 4.5 we can write

$$n_t = \frac{\omega_t n}{\omega_e + j\omega}, \tag{4.6}$$

and substituting for n_t in equation 4.4 we can eliminate n_t and obtain

$$n(\omega)=\frac{G_\omega}{(1+j\omega/\omega_e)\left(j\omega-\dfrac{\omega_t}{1+j\omega/\omega_e}+\omega_t+\omega_r\right)} \tag{4.7}$$

which can be further rationalised to give

$$n(\omega)=\frac{G_\omega}{\left[\omega_r-\dfrac{\omega^2}{\omega_e}+j\omega\left(1+\dfrac{\omega_t+\omega_r}{\omega_e}\right)\right]}. \tag{4.8}$$

For the super-gap excitation in case (c) the rate equation for the free electrons can be written as

$$\frac{dn(\omega)}{dt}=-\frac{dn_t(\omega)}{dt}-\omega_r n(\omega)+G_\omega \tag{4.9}$$

and for the trapped electrons

$$\frac{dn_t(\omega)}{dt}=-\omega_e n_t(\omega)+\omega_t n(\omega). \tag{4.10}$$

By a similar procedure as shown for case (a) it is possible to eliminate $n_t(\omega)$ to obtain $n(\omega)$

$$n(\omega)=\frac{G_\omega}{\left(j\omega-\dfrac{\omega_t}{1+j\omega/\omega_e}+\omega_t+\omega_r\right)}. \tag{4.11}$$

Note the difference between equation 4.11 and equation 4.7, which only contains the additional factor $(1+j\omega/\omega_e)$ in the denominator. This adds an extra 'pole' to the frequency response in case (a) – i.e. above $\omega=\omega_e$, there is an additional fall-off factor in the response.

This is a consequence of the slow thermal emission from D^- states which must occur before any free electrons are produced, in case (a).

It is useful to note that this implies that it is possible to treat 'case (a)' as equivalent to the super-gap excitation in 'case (c)', which just describes the standard MPC, with the simple addition of a pole at $\omega=\omega_e$, in the frequency spectrum of the optical excitation. Equation 4.11 may also be rationalised further to give

$$n(\omega)=\frac{G_\omega}{\left(\omega_t+\omega_r-\frac{\omega_t}{1+(\omega/\omega_e)^2}+j\omega\left(1+\frac{\omega_t/\omega_e}{1+(\omega/\omega_e)^2}\right)\right)}. \tag{4.12}$$

In a CPM experiment, at super-gap excitation, it is expected equation 4.11 to hold. At sub-gap excitation, it is possible that processes (a) and (b) occur in parallel. Further the results of cases (b) and (c) – for *free electrons* – may be formally equivalent if ignoring the contribution of holes and thermal transitions between defects and the valence band, and for low excitation which does not perturb occupancies. The net result may be that the frequency responses for sub-gap excitation will be an appropriately weighted linear superposition of case (a) and case (b).

4.2.2 Simulation results for a single level

To make the implication from the equation 4.4 and 4.11 more clear to understand, a simulation has been performed and is presented in figure 4.4. The parameter list used for the simulation is as follows

$N_c = 10^{20}\ cm^{-3}$

$v\sigma = 10^{-8}\ cm^3\ s^{-1}$

$\nu = N_c\ v\sigma = 10^{12}\ s^{-1}$

$T = 300\ K$

$E_l = 0.7\ eV$

$N_t = 10^{16}\ cm^{-3}$

$\tau_r = 10^{-7}\ s$

$\omega_r = 1/\tau_r$

Ratio of optical generation rates $G_a/G_b = 100$

$\omega_t = N_t\ v\sigma = 10^8\ s^{-1}$

$\omega_e = n_u\ exp(-E_t/kT) = 1.8\ s^{-1}$

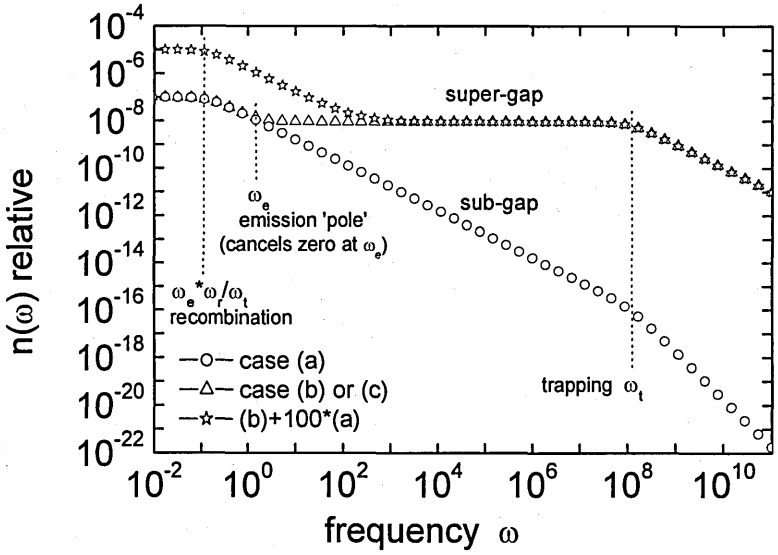

Figure 4.4 Sub-gap MPC simulation for case (a), (b) and (c) as a result from equation 4.7 and 4.11.

The demonstration shown in figure 4.4 could be used to qualitatively explain the discrepancy between DC and AC CPM results, in the low – energy region.

If case (b) only applied and recalling that this is equivalent in frequency response to super-gap excitation, then in the frequency range in question (or in any frequency range), the AC photo signal, as photon energy is reduced, will be independent of chopping frequency, and will simply be a reduced amplitude version of the DC case, since the density of states from which the optical transitions start, is smaller than the band-density.

If case (a) only applied for sub-gap excitation, then as the chopping frequency is increased, the signal level will follow curve (a), continuously falling with frequency. This does not happen in practice, as the absorption curves 'coalesce' at higher chopping frequencies.

In the 'realistic' case of (a) and (b) occurring together, for sub-gap excitation, the response first falls with frequency, and then reaches a plateau. This should explain both the change in CPM absorption spectrum with AC excitation, and the coalescence of the curves at high chopping frequencies.

If process (a) slows the response at low photon energies, this then requires an increase in the excitation level to maintain a 'constant' signal level. This is interpreted as a lower absorption.

Note including the effect of a range of shallow conduction band tail states on the frequency response is very simple, if they are formally included as being only involved in trapping and thermal (not optical) transitions.

Including the effect of distributed valence band tail states and defects is rather more difficult, but the basic concept would still apply.

4.2.3 Sub-gap AC CPM – Distributed States

Figure 4.5 shows the 'case (a)' situation, extended from figure 4.1 to include the distribution of excitation paths.

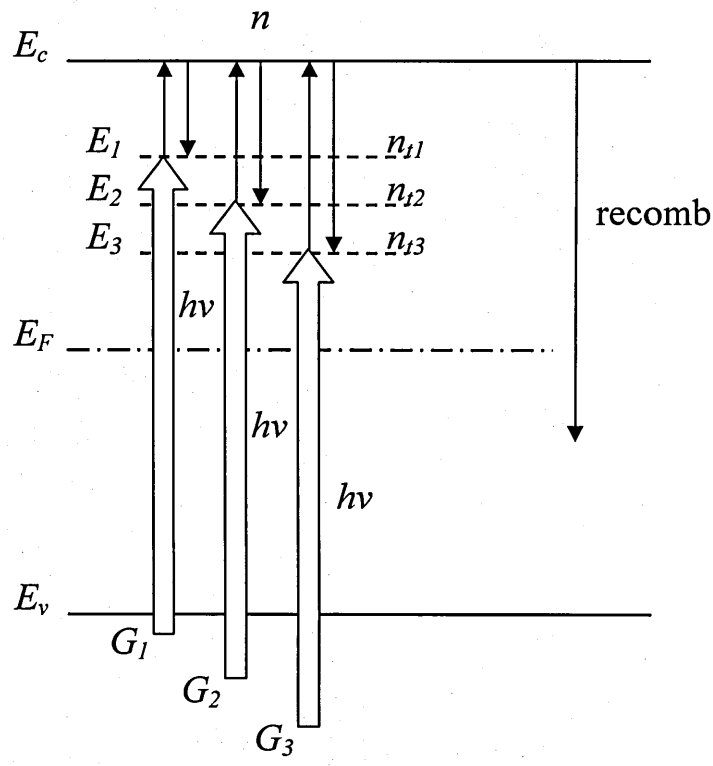

Figure 4.5 Energy level scheme for the analysis of sub-gap excitation. Optical and thermal transitions are shown for three levels. Typically, several hundred levels were employed in calculations.

The situation looks rather more complicated to analyse. The rate equation 4.1 and 4.2 for 'case (a)' conditions, i.e. optical excitation followed by thermal emission, become

$$\frac{dn(\omega)}{dt} = -\sum_i \frac{dn_{ti}(\omega)}{dt} - \omega_r n(\omega) \tag{4.13}$$

and

$$\frac{dn_{ti}(\omega)}{dt} = -\omega_e n_{ti}(\omega) + \omega_t n(\omega) + G_{\omega,i}, \tag{4.14}$$

where the DOS is represented by a fine discrete array. The level-to-level sinusoidal excitation rates $G_{\omega i}$ are assumed proportional to the joint density of states for the occupied initial and empty final states ('*i*'), separated by the photon energy E_{ph} – i.e. assuming a fixed optical transition matrix element. Further, the emission frequency $\omega_{ei} = \nu \exp(-E_{ti}/kT)$, where ν is an attempt-to-escape frequency (value 10^{12} Hz assumed), E_{ti} is the trap depth, k the Boltzman's constant and T the absolute temperature.

Recalling the result from equation 4.7 it is possible to convert each separate generation rate $G_{\omega i}$ into a 'super-gap' rate with an appropriate pole in its frequency spectrum. This converts the problem into a 'case (c)' super-gap excitation situation (just MPC!), simply summing all the converted optical generation rates. The AC solution for the above equation system is then given as

distributed poles

$$n(\omega) = \left\{ \frac{\sum_k G_{\omega,k} / (1 + j\omega/\omega_{ek})}{\left(j\omega + \sum_i \left(\omega_{ti} - \frac{\omega_{ti}}{1 + j\omega/\omega_{ei}} \right) + \omega_r \right)} \right\}. \qquad (4.15)$$

mpc (super-gap) result

Note that the 'k' summation is over states involved in sub-gap transitions, while the 'i' summation is over all gap states. It is expected for the measured AC photocurrent that $I_{ph}(\omega) \propto n(\omega)$.

4.2.4 Simulation results for distributed states

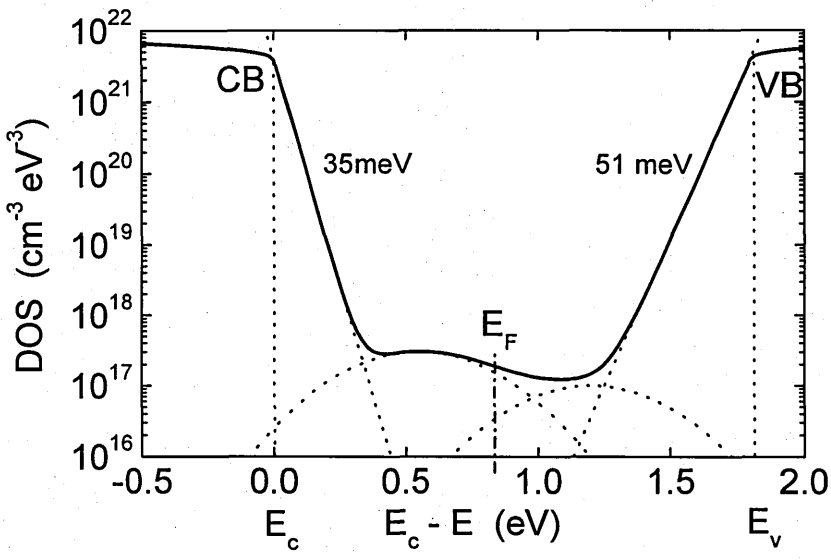

Figure 4.6 Model DOS used to compute DA and AC CPM using equation 4.15.

Equation 4.15 was applied to the simple model DOS of figure 4.6, containing two band-tails, two broad Gaussian defect distributions and parabolic variation above the mobility edges to compute the DC and AC CPM plots of α vs E_{ph} for a range of frequencies. Figure 4.7 shows the computed results. There is a reasonably good agreement with the experimental data of figure 4.1. At this stage it should be mentioned that such a good agreement has not been obtained for the alternative of MPC magnitude and phase for sub-gap excitation.

The reason for the difference between the DC and the AC α plots is that the DC measurement includes the transitions into unoccupied defect states which require a further thermal release to produce free carriers. This process is too slow – i.e. the associated poles are at low frequencies below 10 Hz in the case studied. An important corollary of this is that the AC response should ignore such transitions, and should arise only from transitions from occupied defects into the conduction band (or shallow tail states). In fact, this is usually the assumption made in deconvolution approaches to computing the DOS from CPM! It is now evident from the present analysis, that such an assumption, and its results, could be quite erroneous.

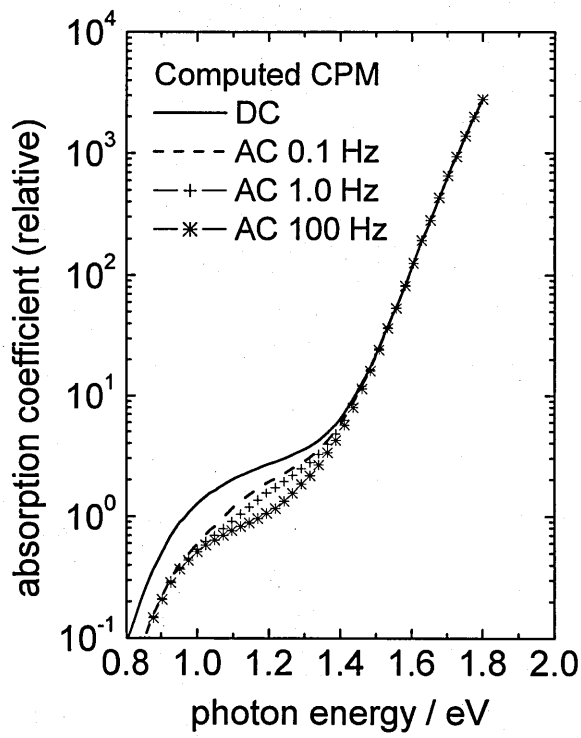

Figure 4.7 Computed DC and AC CPM for the DOS model of figure 4.5. The higher values for the DC α at low photon energies are associated with phonon-assisted transitions involving the unoccupied, upper defect distribution (D^{0}).

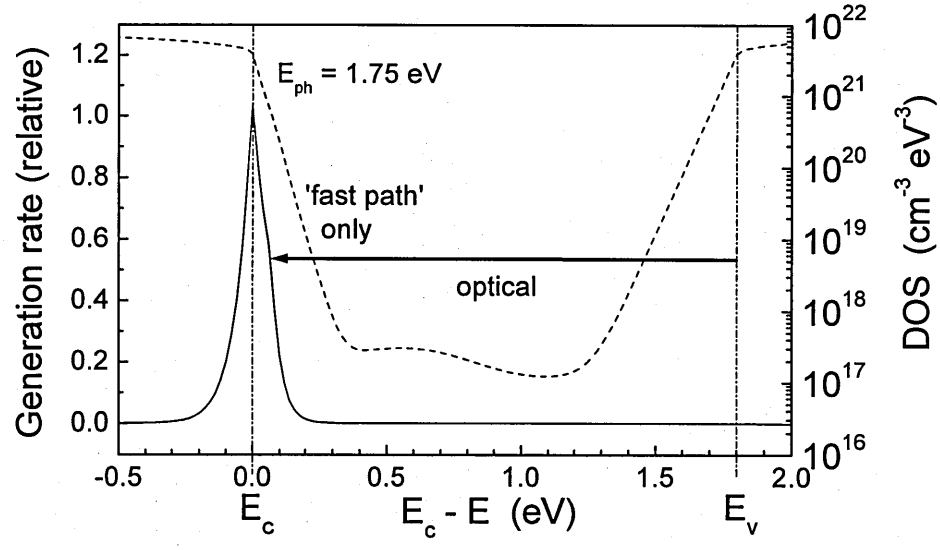

Figure 4.8 Computed distribution of transitions for E_{ph} = 1.75 eV. Only optical transitions (fast) from E_v to E_c are occurring (the dotted curve represents the DOS).

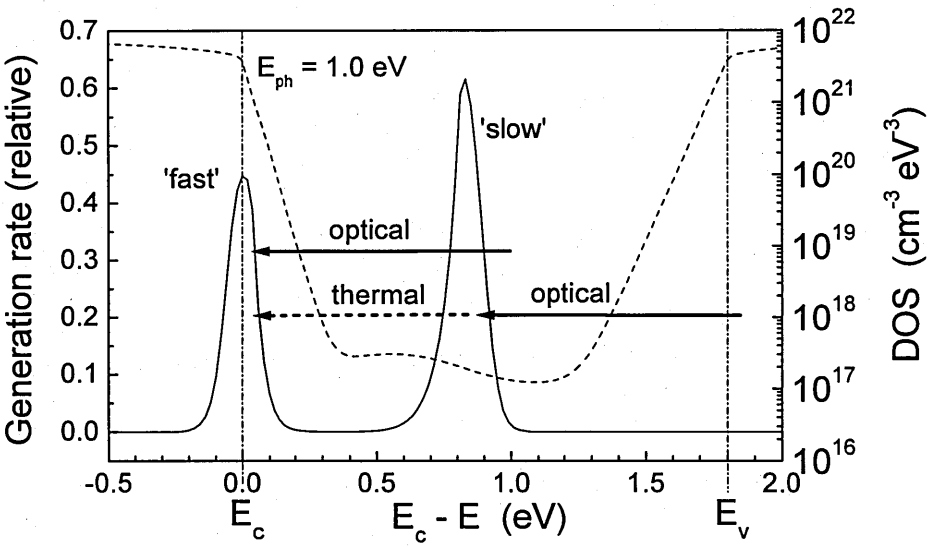

Figure 4.9 Computed distribution of transitions for E_{ph} = 1.0 eV. The number of slow transitions, which consist of optical transitions (fast) from the valence band into empty defects above the Fermi energy followed by thermal release (slow) into the conduction band, grows as the photon energy reduces. The fast component consists of optical transitions from occupied defects directly into the conduction band.

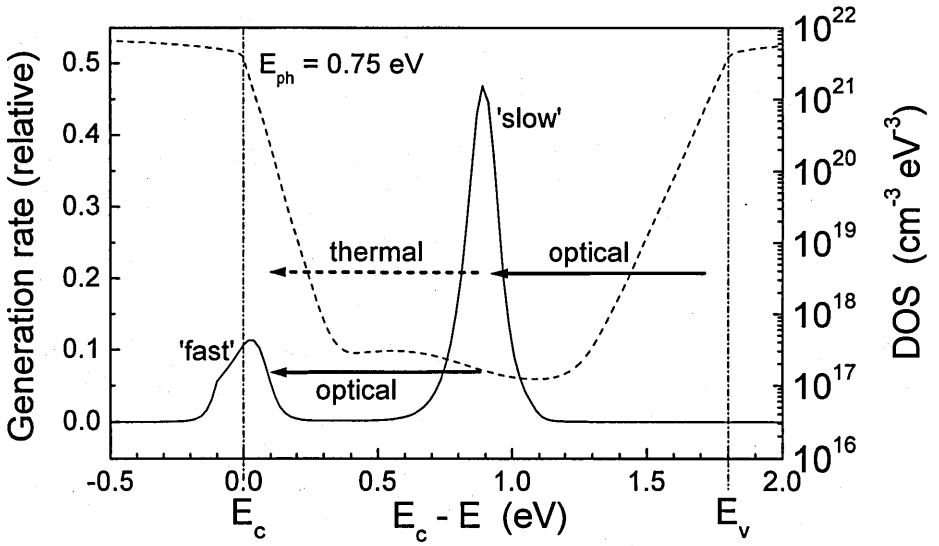

Figure 4.10 Computed distribution of transitions for E_{ph} = 0.75 eV. The slow transitions type (optical followed by thermal) is the major path of transitions for photon energies E_{ph} < 1 eV.

Figure 4.8 shows the computed distribution of transitions occurring for E_{ph} = 1.75 eV. As seen only optical transitions occur, from the valence band E_v into the conduction band E_c and the conduction band tail states, classified as the 'fast path'. No important thermal transitions are occurring. As E_{ph} reduces, the number of optical transitions from E_v into unoccupied defects above E_F followed by thermal transition (slow) into E_c increases, in parallel with a decreasing number of optical (fast) transitions directly into E_c (figure 4.9). For photon energies E_{ph} < 1 eV the slow path dominates the computed distribution of transitions as shown in figure 4.10. Comparing the figures 4.8 to 4.10 with the computed DC and AC CPM spectra shown in figure 4.7, the DC CPM curve splits away from the AC CPM curve at E_{ph} = 1.4 eV indicating that it is taking the 'slow path' for transitions in account as the AC CPM curve ignores them.

As an example, consider the rather extreme model case presented in figure 4.11, in which there is a high density of unoccupied defect states, and relatively few occupied defects. Figure 4.12 shows the computed CPM spectra for the DC and AC (100 Hz) cases.

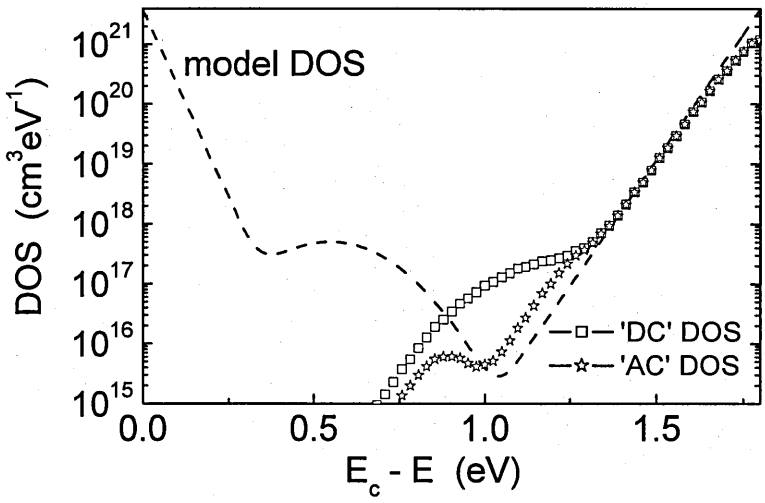

Figure 4.11 Illustrative model DOS with high density of unoccupied states above mid-gap, with superimposed computed DOS from DC and AC CPM spectra. The AC – derived DOS is much closer to the actual DOS.

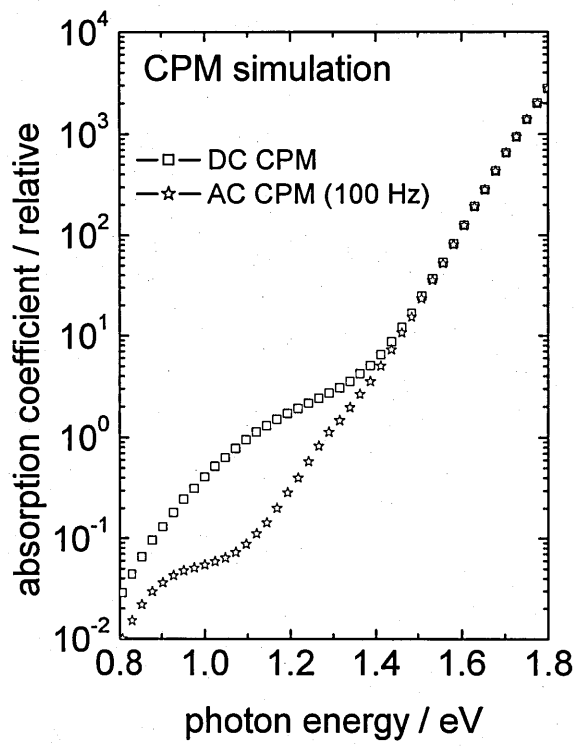

Figure 4.12 DC and AC CPM spectra computed from the model DOS of figure 4.11.

In figure 4.12 the DC simulation shows an apparent defect 'shoulder' at photon energies below 1.4 eV, while the AC simulation continues down the Urbach slope to E_{ph} = 1.1 eV. The computed DOS for each case is superimposed on the model DOS in figure 4.11, where it is clear that the DC case which includes the phonon assisted transitions, is incorrectly interpreted by the deconvolution process as a deep *occupied* set of defects. On the other hand, the AC CPM spectrum gives a DOS much closer to the actual DOS.

A different case illustrated in figure 4.13 shows a model DOS with only occupied defects below the Fermi-level. As a result mainly optical transitions ('fast path') are generating the photocurrent. Figure 4.14 shows the computed DC and AC CPM spectra resulting from figure 4.13. There is only a very small gap noticeable between both CPM spectra.

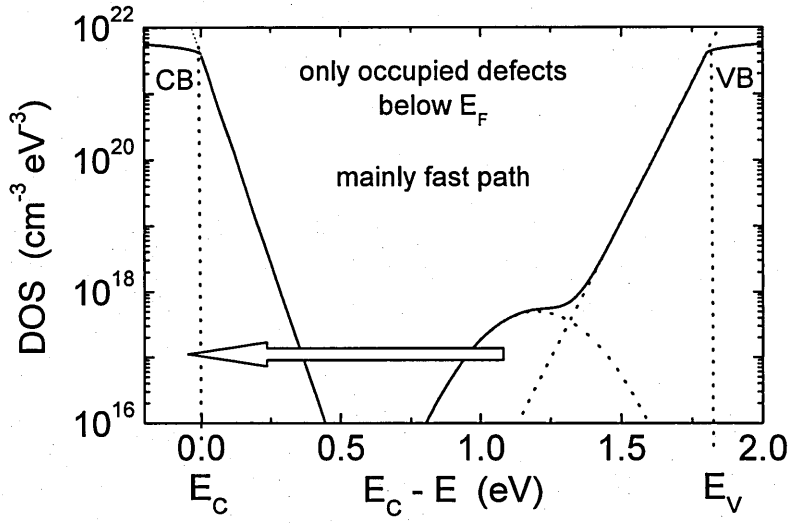

Figure 4.13 Illustrative model DOS with high density of occupied states below the Fermi-level. Photocarrier generation is mainly dominated by optical transitions ('fast path').

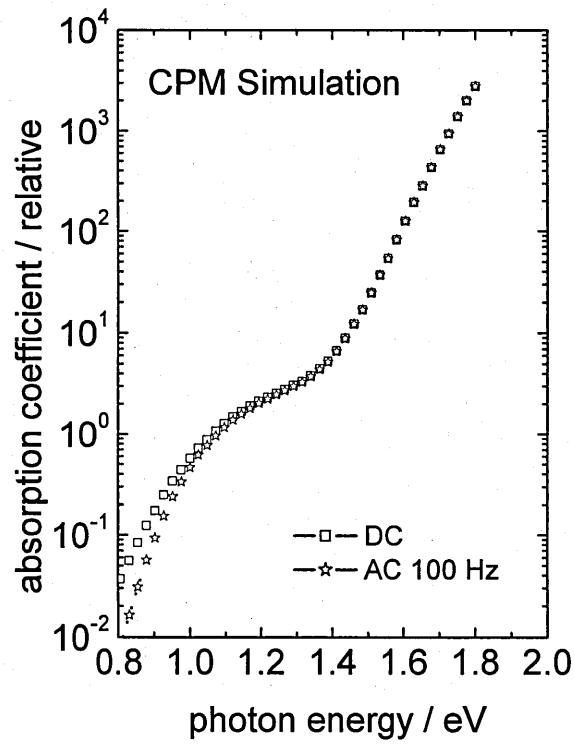

Figure 4.14 DC and AC CPM spectra computed from the model DOS of figure 4.13. The difference between DC and AC is very small.

4.3 Summary

- DC and AC CPM show differences in intrinsic a-Si:H. (Expect no difference in n-type material because the Fermi-level is too close to the conduction band!)
- Origin - 'slow' phonon assisted free carrier creation via unoccupied defects (optical transition into unoccupied defect followed by thermal release).
- Simple analysis for AC CPM - transformed into 'weighted MPC'.
- AC CPM selects 'fast' transitions from occupied defects - hence better for DOS determination.

The next chapter will compare experimental results with the model predictions for DC and AC CPM. In chapter 6 a new method will be presented for obtaining the DOS below and above mid gap by subtracting the AC and DC values for $\alpha(E_{ph})$.

Chapter 5 - DC & AC CPM – Experiment and model comparison

DC and AC CPM experiments have been performed on PECVD and HWCVD produced samples, which reveal a range of behaviours. These results will be compared with the results and predictions obtained from simulations based on equation 4.15.

5.1 Sample preparations

The HWCVD film 'HW159' was prepared in a laboratory system with: gas flow rate 8 sccm, chamber pressure 220 mTorr, tungsten wire temperature 1500 °C, substrate temperature 200 °C, thickness 3 μm. The PECVD film 'ISB4' was prepared in an industrial reactor with: 5% hydrogen dilution, chamber pressure 500 mTorr, substrate temperature 200 °C, thickness 1.7 μm. Chromium T-shape contacts with 5 mm in length and 1 mm gap size between were been deposited onto both films. These films were measured after annealing at 180 °C for 3 hours, and again following exposure to simulated AM1 radiation for 1000 minutes. CPM spectra were obtained following the procedures explained in chapter 3. The voltage applied to the sample creating the electric field in the gap was 300 V.

The AC CPM measurements were performed by using the 'absolute' CPM method and a chopper frequency of 5 Hz if not otherwise stated. The DC CPM measurements were performed by measuring the total photocurrent for the I_{CPM} and giving the dark current enough time to relax after each photon energy step. The photon flux was typically less than 10^{13} $cm^{-2}s^{-1}$ so that the AC and the DC photocurrents were usually of the same order of magnitude as the dark current. The $\mu\tau$-products were measured at photon energy E_{ph} = 1.96 eV and a steady photon flux $\Phi = 10^{14}$ cm^{-2} s^{-1}. The DOS was obtained using the method described by P. Jensen (see chapter 2.8).

5.2 Experimental results for the annealed state

The CPM spectrum shown in figure 5.1 should be taken as a test measurement to verify the 'absolute' CPM method while comparing it with the result for the absorption coefficient from optical transmittance measurements. The absolute CPM measurement was performed in AC mode at 5 Hz on the ISB4 PECVD sample. The $\mu\tau$-product measured for this sample after annealing is $1.31 \cdot 10^{-5}$ V cm^{-2}, which indicates a very good intrinsic material as it also shows a very low defect shoulder below $E_{ph} < 1.4$ eV. As shown in this diagram there is a very good agreement between the $\alpha(E_{ph})$ from A-CPM and from the optical transmittance for photon energies above 1.7 eV.

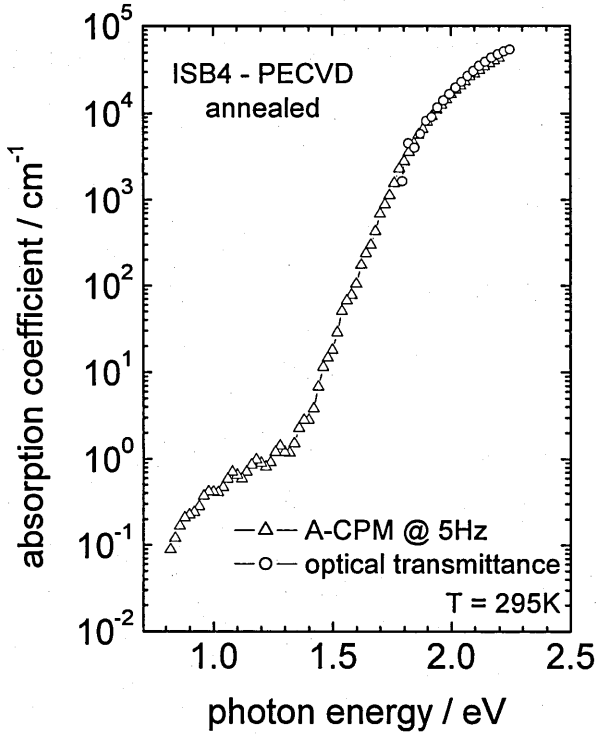

Figure 5.1 Absolute CPM (A-CPM) spectrum for the ISB4 PECVD (annealed) in comparison with $\alpha(E_{ph})$ obtained from optical transmittance. The overlap between both measurements is nearly perfect. This result is used as verification for the absolute CPM method.

In figure 5.2 the DC CPM result was added to the AC A-CPM result shown in figure 5.1. The DC spectrum was shifted to match the Urbach part of the $\alpha(E_{ph})$ spectrum. It is

noticeable that the DC and AC spectra differ by up to a factor 3 for photon energies below 1.4 eV.

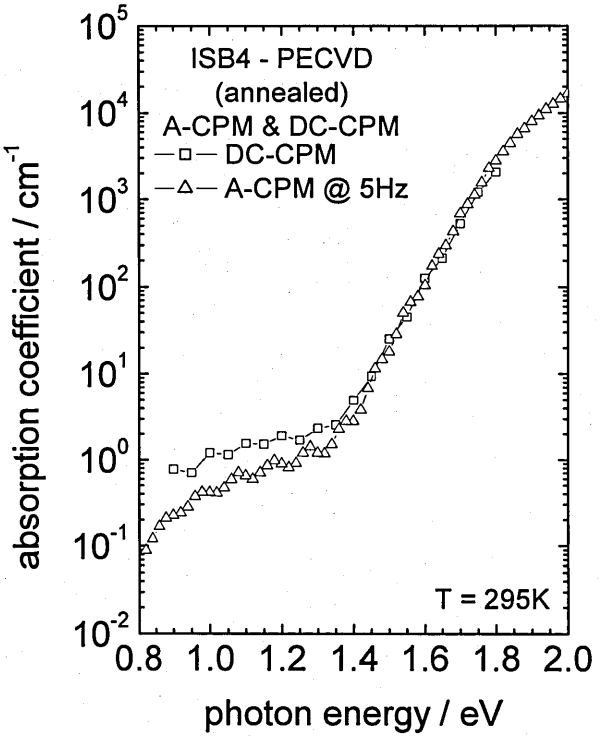

Figure 5.2 Comparison between A-CPM and DC-CPM results for the ISB4 PECVD sample (annealed). Very noticeable the gap between both absorption curves for photon energies E_{ph} < 1.4 eV. Note the DC-CPM measurement was shifted to absolute scale at overlap with the Urbach part from A-CPM.

Figure 5.3 shows the DC and A-CPM result for the 'HW159' HWCVD sample. The difference between the DC and A-CPM results is up to a factor of 5 for photon energies below 1.5 eV. This is even larger than for the PECVD sample. The $\mu\tau$-product measured for the HWCVD sample after annealing was $5.78 \cdot 10^{-6}$ V cm^{-2}, which indicates a good intrinsic material too.

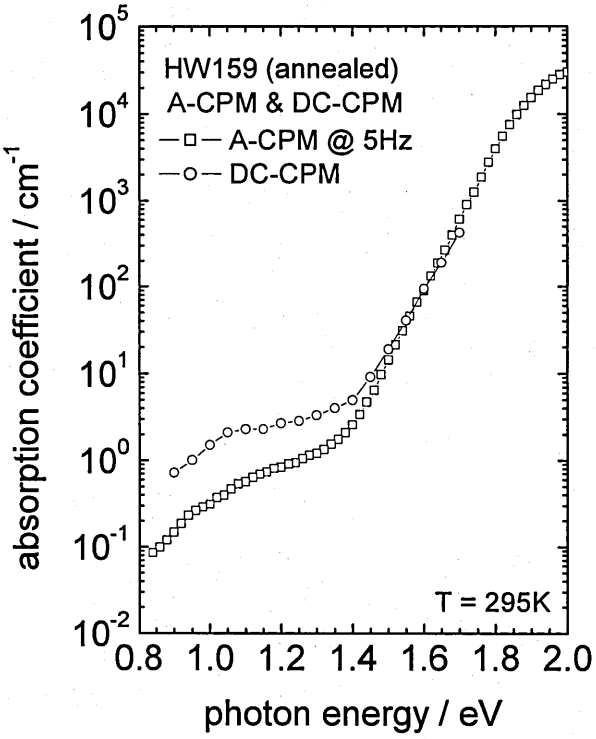

Figure 5.3 Comparison between A-CPM and DC-CPM results for the HW159 HWCVD sample (annealed). Very noticeable is the gap between both absorption curves for photon energies $E_{ph} < 1.4$ eV which is even larger than in figure 5.2.

Figure 5.4 and 5.5 show the comparison between DC and AC-CPM results performed at chopper frequencies from 0.2 Hz, 0.5 Hz, 1 Hz, 5 Hz, 27 Hz and 69 Hz. The chopper frequencies below 5 Hz were established by using a 'solenoid' device and operating the Lock-In amplifier measuring the CPM photocurrent I_{CPM} in 'DC-Coupling' mode. Figure 5.4 shows the result for the 'ISB4' PECVD sample and figure 5.5 the result for the 'HW159' HWCVD sample. The chopper frequency set was chosen to cover the available range in roughly logarithmic spacing but avoiding getting too close to 50 Hz because of possible interference with the mains power frequency. The AC CPM measurements were performed in 'standard' CPM (S-CPM) mode and were shifted to absolute scale by using the A-CPM result shown in figure 5.2 and 5.3.

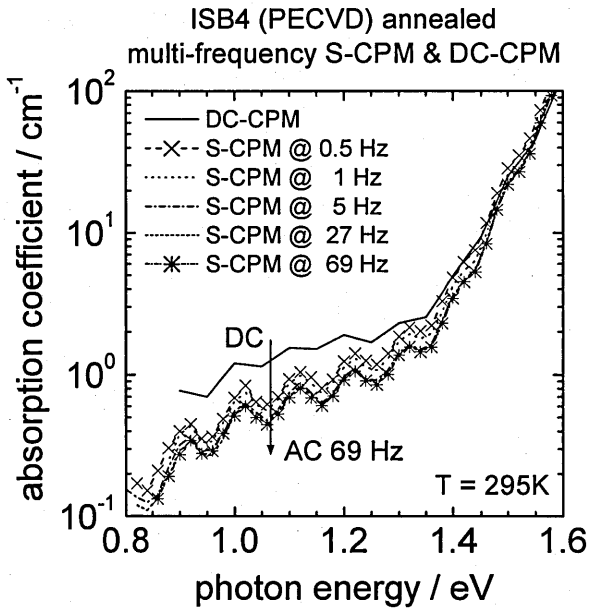

Figure 5.4 Comparison between DC-CPM and S-CPM performed for 5 different chopper frequencies for ISB4 PECVD sample (annealed). Starting from DC the absorption curves converging towards 69 Hz chopper frequency. The S-CPM and DC-CPM were shifted to absolute scale by using the absolute CPM result in figure 5.2.

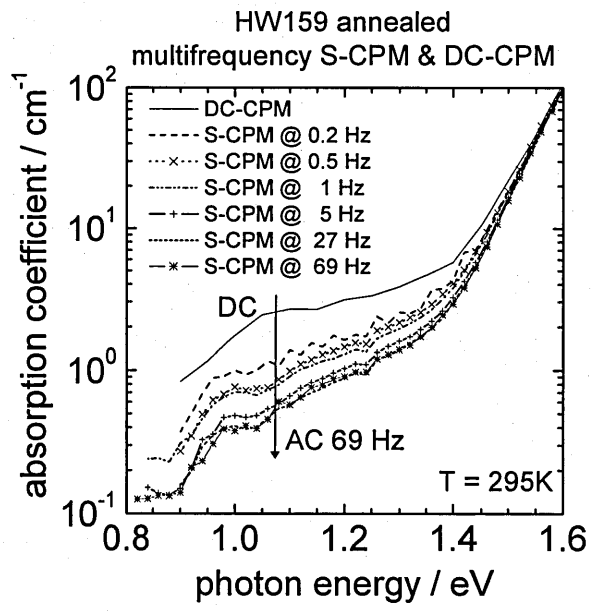

Figure 5.5 Comparison between DC-CPM and S-CPM performed for 6 different chopper frequencies for HW159 HWCVD sample (annealed). Starting from DC the absorption curves converge towards the 69 Hz chopper frequency. The S-CPM and DC-CPM were shifted to absolute scale by using the A-CPM result in figure 5.3.

Figure 5.4 and 5.5 both show a split between the DC CPM curve from photon energy E_{ph} = 1.5 eV towards lower photon energies. At E_{ph} = 0.9 eV the difference between the AC CPM at 69 Hz chopper frequency is up to a factor of 3 for the PECVD sample and up to a factor of 5 for the HWCVD sample. In both figures the CPM curves begin to converge for chopper frequencies above about 5 Hz. Comparing the results for 27 Hz and 69 Hz chopper frequency there is nearly no difference visible anymore in both sets.

The figure 5.6 shows a set of simulated CPM curves for DC, 0.1 Hz, 1 Hz, 10 Hz and 100 Hz, based on the model DOS presented in chapter 4.2.4, figure 4.6. Superimposed is the experimental result from the HW159 sample shown in figure 5.5 for DC and AC 69 Hz only. In figure 5.7 a similar result is presented for the ISB4 PECVD sample.

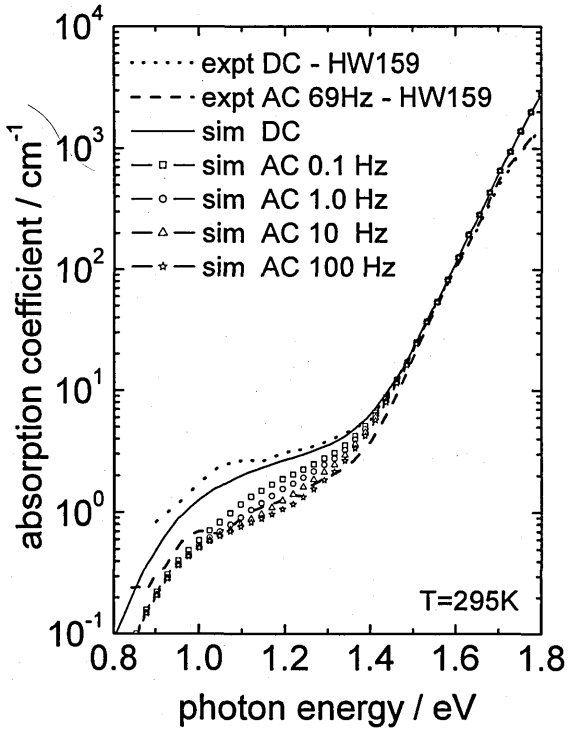

Figure 5.6 Set of simulated CPM curves for DC and AC. Superimposed the results for DC and AC-CPM (69 Hz) for the HW159 sample. Both simulation and experiment agree reasonably well.

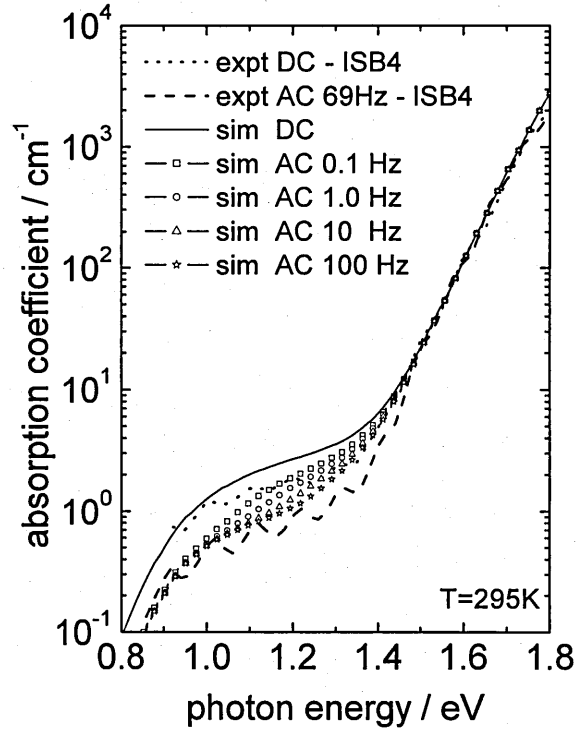

Figure 5.7 Set of simulated CPM curves for DC and AC. Superimposed - the results from DC and AC-CPM (69 Hz) for the PECVD sample.

Figure 5.8 and 5.9 presents the density of states obtained using the Jensen analysis – Equation 2.38, from the experimental CPM data from figure 5.4 and 5.5. There is a similar discrepancy between the DC and AC-derived DOS for the PECVD and HWCVD sample as shown in figure 5.8 and 5.9.

Figure 5.8 shows that the DC method overestimates the DOS by a factor of 2 compared with the AC method for the PECVD sample and in figure 5.9 the DC method overestimates the DOS by a factor of 4 compared with the AC method. This leads, in this case, according to the theory presented in Chapter 4, to the prediction that the HWCVD sample has a higher density of defect levels above the mid-gap than the PECVD sample and that the DC-CPM has a greater component of slow transitions for the HWCVD sample. The AC derived DOS for both samples compared are very similar. In fact, it turns out that *further* information on the DOS can be obtained than has been described thus far; this will be dealt with in Chapters 6 and 7.

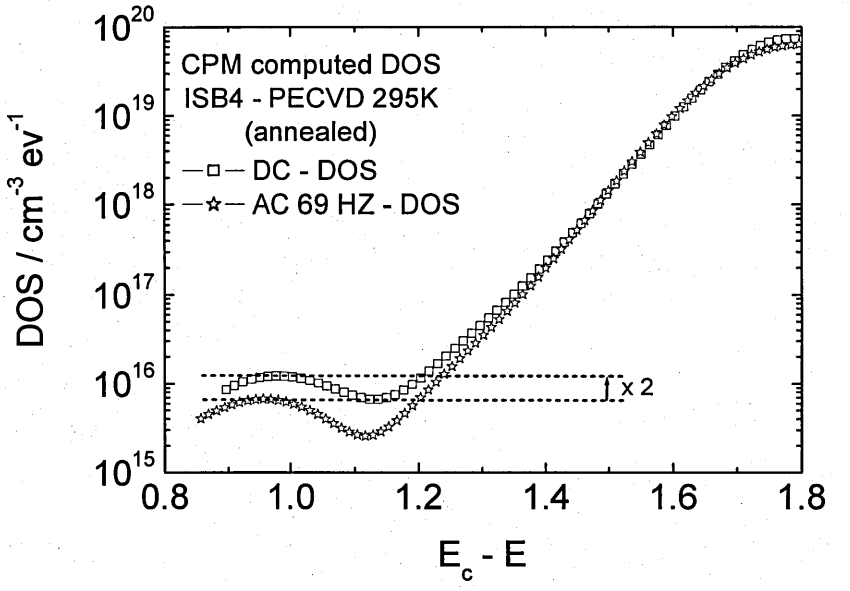

Figure 5.8 DOS derived from DC and AC CPM (69 Hz) measurements of figure 5.4 for the PECVD sample. The DC method overestimates the DOS by a factor of 2.

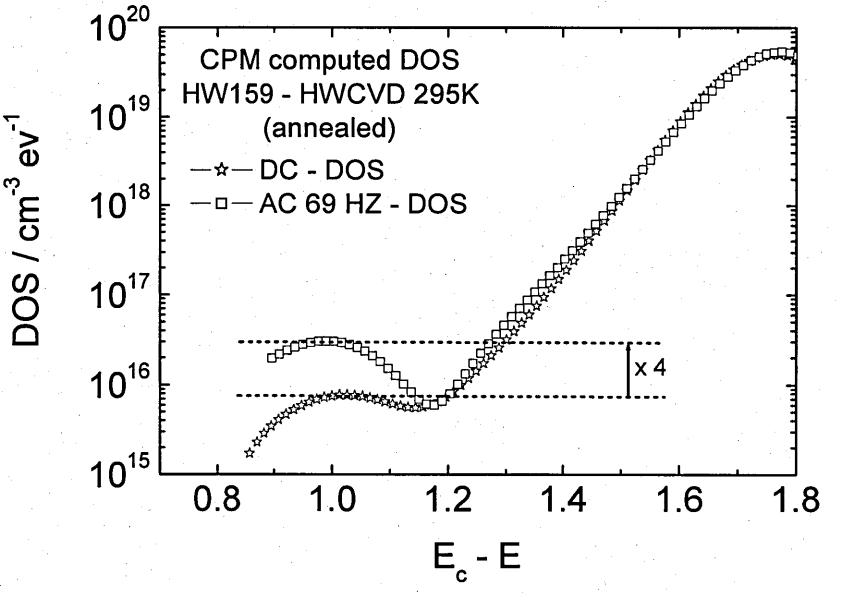

Figure 5.9 DOS derived from DC and AC CPM (69 Hz) measurements of figure 5.5 for the HWCVD sample. The DC method overestimates the DOS by a factor of 4.

5.3 Experimental results for light-soaked state

Here the samples were exposed to AM1 radiation for 1000 min. to increase the defect density to examine possible changes in the DC-AC discrepancy. Figure 5.10 shows the results for DC and AC-CPM (5 Hz) for the ISB4 PECVD sample after annealing and light-soaking. The difference between the annealed and light-soaked state in AC mode is bigger than in DC mode. Also the discrepancy between the light-soaked DC and AC-CPM curves has nearly disappeared.

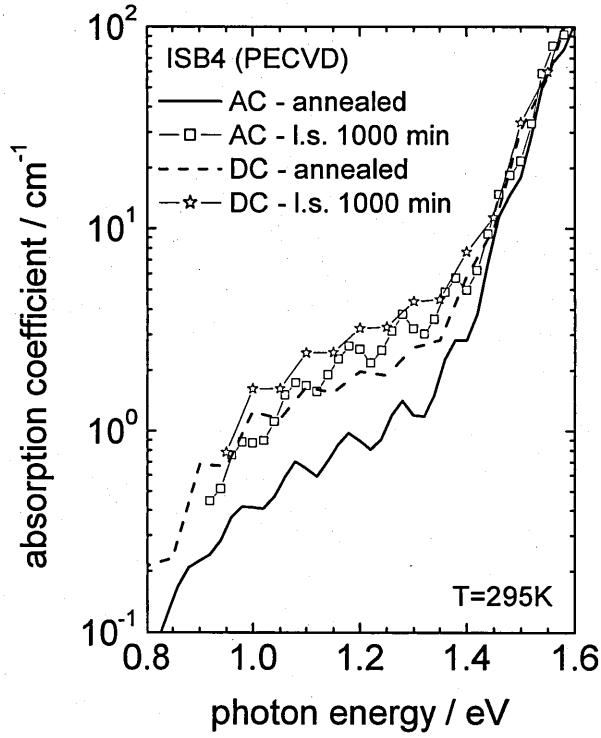

Figure 5.10 DC and AC-CPM (5 Hz) measurements for the ISB4 (PECVD) sample after annealing and light-soaking (l.s.) for 1000 min under simulated AM1 condition.

The light-soaking results for the HWCVD sample are presented in figure 5.11. There is only a small increase in the absorption coefficient spectra for both CPM methods after light-soaking but as reported in figure 5.10 the DC and the AC-CPM curves are closer after light-soaking.

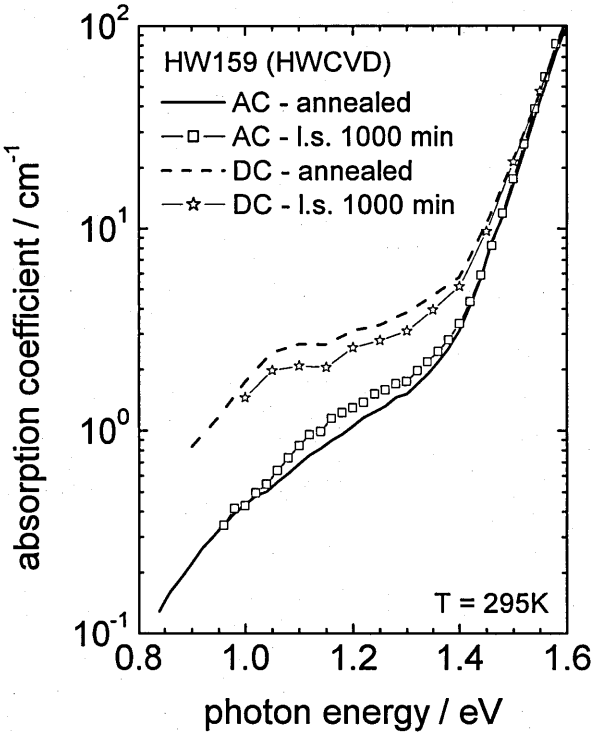

Figure 5.11 DC and AC-CPM (5 Hz) measurements for the HW159 (HWCVD) sample after annealing and light-soaking (l.s.) for 1000 min under simulated AM1 condition. The DC and AC CPM curves are getting closer after light-soaking as in figure 5.10.

As a possible explanation for the results in figure 5.10 it can be argued that for the PECVD sample, light-soaking preferentially increases the density of the occupied defect states immediately above the valence band tail (see figure 4.13 and 4.14). For the HWCVD sample in figure 5.11 a possible explanation might be that light-soaking increased the density of the occupied states immediately above the valence band tail too but also reduced the number of unoccupied defects above mid-gap.

For additional examination DC and AC-CPM measurement were performed at different temperatures. The reason for this action is to investigate the temperature dependency of the 'slow path' which contains the temperature parameter in the thermal release.

5.4 Temperature dependency of the AC-DC discrepancy

By increasing the temperature it is expected from the theory for the thermal release component of the 'slow' path to accelerate the release of the carriers into the conduction band so that the AC-DC discrepancy should either reduce or disappear from the CPM spectra. The CPM measurements have been performed at 350 K and 400 K after annealing and light-soaking with simulated AM1 exposure for 1000 min. The AC CPM spectra were obtained at a chopping frequency of 5 Hz. Figure 5.12 shows the temperature dependence for the ISB4 PECVD sample.

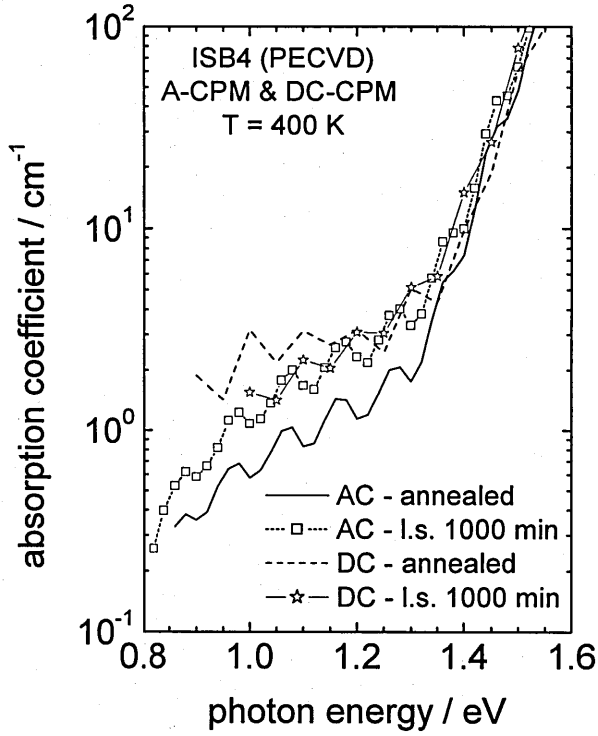

Figure 5.12 ISB4 (PECVD) sample annealed and light soaked (l.s.) for 1000 min under simulated AM1 condition. CPM measurements were performed at 400 K. The increase of the temperature decreases the DC alpha for light-soaked state and the AC-DC discrepancy disappeared after light-soaking.

As seen in figure 5.12 after light-soaking and measurements performed at 400 K the AC-DC discrepancy disappeared from the absorption coefficient spectrum but still remains for the annealed state. Also to be noted is a decrease in the light-soaked DC CPM result

compared with the annealed DC. An explanation would be that by increasing the temperature, a proportion of the slow path transitions are converted into fast path transitions as well as an increase of the occupied defect density just above the valence band by light-soaking. By comparing the AC-DC discrepancy after annealing measured at 400 K with figure 5.10 for room temperature no significant change is observed, only a shift towards low photon energies of the whole spectra, which is due to the temperature change.

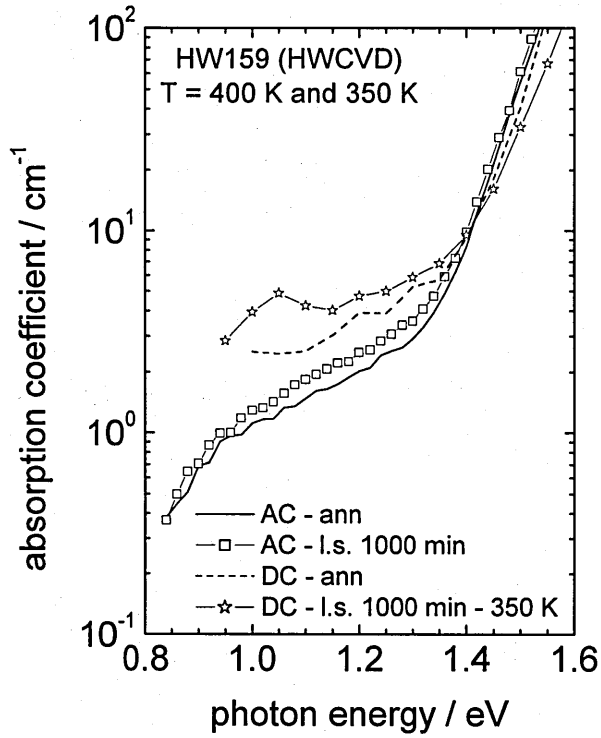

Figure 5.13 HW159 (HWCVD) sample annealed and light soaked (l.s.) for 1000 min under simulated AM1 condition. CPM measurements were performed at 400 K and 350 K. DC-CPM for the light-soaked state could only be performed at 350 K. This result should be only used as an indication.

In the case of the HWCVD sample shown in figure 5.13, in the annealed state the AC-DC discrepancy decreases at 400 K compared with figure 5.11 at room temperature but after light-soaking the AC-DC discrepancy is bigger than at room temperature. Note that the DC CPM measurement after light-soaking was performed at 350 K because at higher temperatures no CPM signal was detectable because of noise. This result could still be used as an indication and for 400 K it is expected for this DC CPM curve will rise even more.

As a result, from figure 5.12 and 5.13 it may be asserted that increasing the temperature has indeed an effect on the AC-DC CPM discrepancy and as predicted the gap between AC and DC mode either gets smaller or even disappears after light soaking in the case of the PECVD sample. For the HWCVD sample the predictions only work for the annealed state but in the light-soaked state it is assumed that the temperature was too low to see the expected effect, since very deep states with long emission times, even at 400K, are involved.

In a different set of measurements during the DC CPM procedure the AC photocurrent was obtained for every photon energy step while keeping the DC photocurrent (and hence carrier lifetime) constant. This corresponds to 'standard' MPC measurements. The aim of these measurements is to monitor the AC photocurrent history during a DC CPM measurement. The AC photocurrent was obtained for 5 Hz, 27 Hz and 69 Hz (where possible).

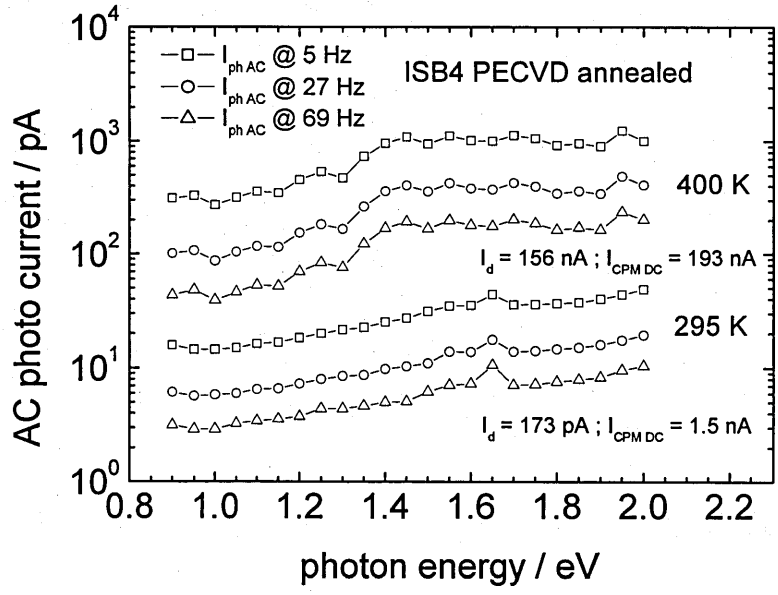

Figure 5.14 Standard MPC-like measurements for the ISB4 PECVD sample after annealing. The DC photocurrent was kept constant throughout the whole energy range and the AC photocurrent was measured for three chopping frequencies. Measurements were performed for room temperature (295 K) and for 400 K.

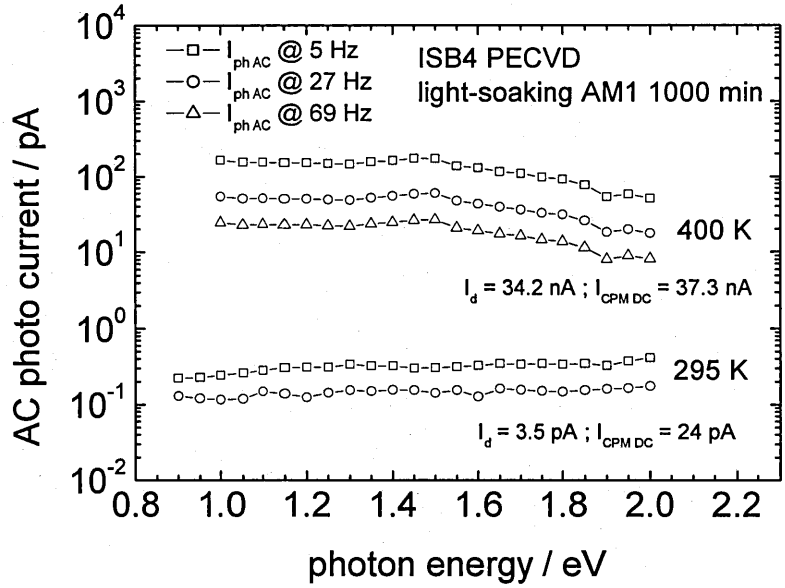

Figure 5.15 Standard MPC like measurements for the ISB4 PECVD sample after light-soaking under simulated AM1 condition. The DC photocurrent was kept constant throughout the whole energy range and the AC photocurrent was measured for three chopping frequencies (where possible). Measurements were performed for room temperature (295 K) and for 400 K.

Figure 5.14 shows a continuous rise of the AC photocurrent with increasing photon energy for measurements at room temperature while at 400 K the AC photocurrent stays roughly constant for photon energies above 1.4 eV. This difference corresponds to the AC-DC discrepancy observed in the annealed state from figure 5.10 (295 K) and 5.14 (400K). In figure 5.15, after light-soaking the AC photocurrent stays constant for the whole photon energy range at room temperature and drops slightly for photon energies above 1.5 eV at 400 K. Comparing with figure 5.10 and 5.12 the AC-DC discrepancy has nearly disappeared at room temperature and disappears at 400 K. There is no noticeable change in the shape of the different chopping frequency curves; only a change in the amplitude when changing the chopping frequency.

As a consequence this leads to the observation if the AC photocurrent is not changing with photon energy during a DC CPM measurement there should be no AC-DC discrepancy visible in the absorption coefficient spectrum.

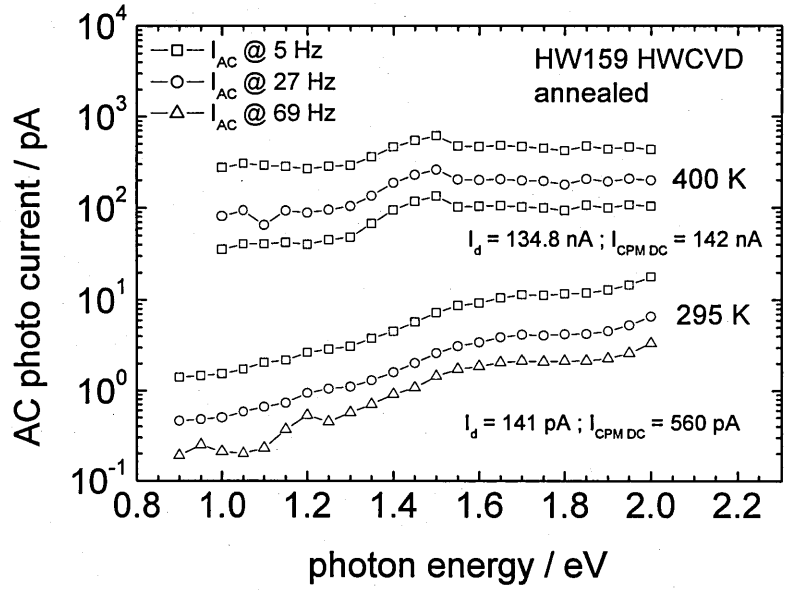

Figure 5.16 Standard MPC-like measurements for the HW159 HWCVD sample after annealing. The DC photocurrent was kept constant throughout the whole energy range and the AC photocurrent was measured for three chopping frequencies. Measurements were performed for room temperature (295 K) and for 400 K.

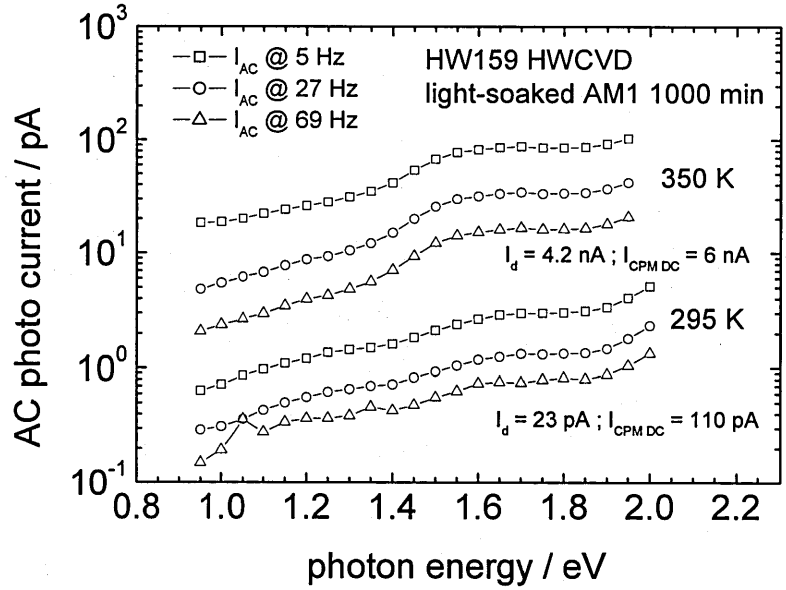

Figure 5.17 Standard MPC-like measurements for the HW159 HWCVD sample after light-soaking under simulated AM1 condition. The DC photocurrent was kept constant throughout the whole energy range and the AC photocurrent was measured for three chopping frequencies. Measurements were performed for room temperature (295 K) and for 400 K.

Figure 5.16 shows the MPC results for the HWCVD sample in the annealed state where again the AC photocurrent rises continuously with the photon energy at room temperature but is remains nearly constant for photon energies above 1.5 eV at 400 K. Comparing figure 5.13 and 5.11 it is noticeable that the gap size between DC and AC CPM decreases with increasing temperature for the annealed state (straight and dotted curves).

Figure 5.17 shows that after light-soaking the AC photocurrent increases continuously with increasing photon energy at room temperature and at 350 K, where at the higher temperature the increase of the AC photocurrent is stronger.

Comparing figure 5.13 with 5.11, the size of the AC-DC discrepancy is increased (square and star symbol curves). It is not yet clear why light-soaking increases the AC-DC discrepancy for the HWCVD sample, especially at higher temperatures. It is assumed that light-soaking preferentially increases the unoccupied defect density above the Fermi-level which might explain the big discrepancy.

As a result the observation made for the PECVD sample applies to the HWCVD sample, too. If there is no change in the AC photocurrent during a DC-CPM measurement, no discrepancy should be visible between an AC and DC-CPM measurement which leads to the suggestion that when AC photocurrent does not change with photon energy, the transitions observed are mainly dominated by the 'fast path' (optical transitions).

In the next chapter a new method will be presented and analyzed in obtaining information about the DOS above the Fermi level from the AC-DC discrepancy.

5.5 Summary

The AC and DC CPM results for the annealed PECVD and HWCVD samples show a significant discrepancy in the low energy part of the CPM spectrum, resulting in a derived DC DOS which overestimates the 'true' AC DOS by a factor of 2 for the PECVD and a factor of 4 for the HWCVD sample.

Modulation frequency dependent CPM measurements show that the CPM curves begin to converge for chopper frequencies above about 5 Hz. At chopper frequencies higher than 27 Hz no change between the CPM curves is noticeable, which also agrees with the simulation results.

At higher temperatures it is expected that the thermally activated transitions become faster and therefore the resulting AC CPM curve should move towards the DC CPM curve. This tendency could be observed for the PECVD sample where the DC and AC CPM curves fully overlapped at 400 K after light soaking, but could not be observed for the HWCVD sample, where it is assumed that the measurement temperature was too low to see the effect.

If an AC photocurrent measured during a DC CPM sweep does not change with the photon energy – i.e at the same photon flux as for the DC measurement – there should be no discrepancy visible between the AC and DC CPM absorption results.

Chapter 6 - Extension to the DC & AC CPM theory – Calculation of the DOS above E_F

6.1 Introduction

This chapter will demonstrated that it is possible not only to extract information from the respective CPM 'absorption' spectra, on the DOS below the Fermi level – i.e. occupied states, but also on the density of unoccupied states above the Fermi level. The ability to discriminate between these two groups of states by using DC and AC modulated sub-gap light arises from the frequency dependence of the different excitation pathways by which free electrons can be produced. AC modulated excitation will reveal absorption associated with transitions from occupied states into the conduction band, while DC excitation will include transitions from the valence band into unoccupied defect states, followed by slow thermal emission to the conduction band.

The temperature dependence of the CPM spectra will be examined and a simple analysis of the DC and AC absorption spectra will be presented, which allows the two regions of the DOS, above and below the Fermi level, to be determined.

6.2 Theory extension based on previous MPC-CPM model

In chapter 4 a model was presented offering a simple explanation for the differences often observed between sub-gap absorption spectra in a-Si:H as measured by DC and AC-CPM techniques. Essentially, the DC method monitors the photoconductivity arising from free electrons which reach the conduction band in two ways; (a) by optical transition from valence band states into unoccupied gap-states above E_F, followed by a thermal emission step, into the conduction band ('slow' path), and (b) by optical transition into the conduction band from occupied gap-states below the Fermi energy E_F ('fast' path. On the other hand, an AC measurement made with modulated sub-gap excitation, even at frequencies as low as 1 Hz, may not register the (a) component if the thermal transition rates involved are much slower than the frequency of modulation. The two processes are illustrated in figure 6.1.

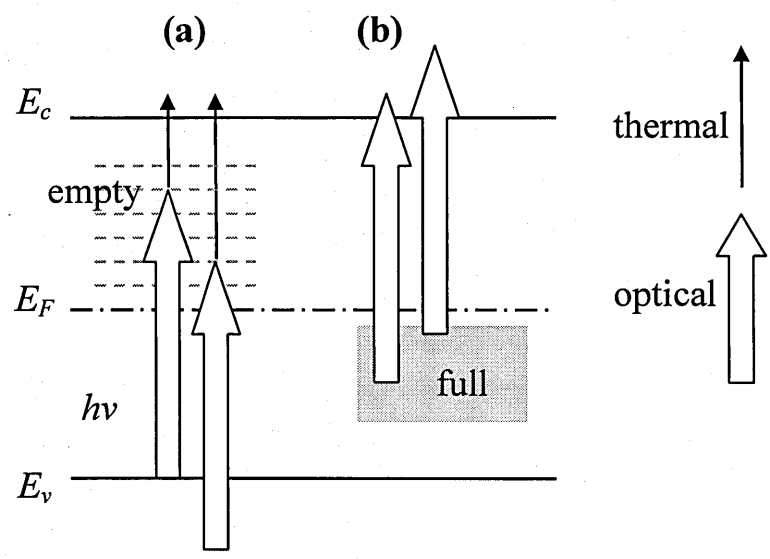

Figure 6.1 Schematic diagram of the two paths by which sub-gap excitation produces free electrons.

The small signal rate equations for free electrons, and gap states, for sub-gap excitation, may be adapted from Chapter 4 and written,

$$\frac{dn(\omega)}{dt} = -\sum_i \frac{dn_{ti}(\omega)}{dt} - \omega_r n(\omega) + \sum G_{\omega,l}\,, \tag{6.1}$$

$$\frac{dn_{tk}(\omega)}{dt} = -\omega_{ek} n_{tk}(\omega) + \omega_{tk} n(\omega) + G_{\omega,k}\,, \tag{6.2}$$

where the DOS is represented by a discrete array, $n(\omega)$ represents the excess free electron density as a function of the frequency ω, $n_{ti}(\omega)$ is the trapped electron density in level i, and ω_{ti}, ω_{ei}, ω_r are characteristic trapping and thermal emission frequencies for trap 'i' and a recombination frequency respectively. The sinusoidal excitation rate $G_{\omega,k}$ is proportional to the joint density of states for the occupied valence band states and empty trap 'k' states, separated by photon energy E_{ph}, and hence is part of the '*slow*' process (a). $\sum G_{\omega,l}$ is the summation of transitions from occupied gap states into the conduction band, and hence is the rate of 'fast' process (b).

Emission frequency is as before,

$$\omega_{ek} = \nu \exp(-E_{tk}/kT), \tag{6.3}$$

where ν is assumed = 10^{12} Hz, E_{tk} is the trap depth, k is the Boltzmann's constant and T is the absolute temperature. The model allows for optical transitions and multi-trapping thermal transitions. The AC solution for equations 6.1 and 6.2 follows the same procedure as already described in chapter 4.2.3, but here explicitly includes both 'slow' and 'fast' transitions and is obtained as

$$n(\omega) = \left\{ \frac{\overset{(b)}{\sum_l G_{\omega,l}} + \overset{(a)}{\sum_k G_{\omega,k}/(1 + j\omega/\omega_{ek})}}{\left(j\omega + \sum_i \left(\omega_{ti} - \frac{\omega_{ti}}{1 + j\omega/\omega_{ei}} \right) + \omega_r \right)} \right\}, \tag{6.4}$$

where $\sum G_{\omega,l}$ represents the generation rate sum of the 'fast' process (b) transitions, directly into the conduction band, and $\sum G_{\omega,k}$ is the sum of the 'slow' process (a) transitions starting in the valence band. The denominator represents the effect of multiple trapping in all states above E_F, on the AC response, and applies to both components. For a given photon energy E_{ph}, the two ranges of gap states involved in the response lie between E_c - E_{ph} and E_F, for process (a), and between E_F and $E_v + E_{ph}$ for process (b).

The AC photocurrent, $I_{ph}(\omega) \propto n(\omega)$. The response described by equation 6.4 contains a component arising from process (b) which is the *same* as for super-gap excitation, i.e. 'MPC' as reported earlier in chapter 4.2.3, equation 4.15, and a component arising from process (a) which contains additional multiple 'poles', effectively in the generation rate, corresponding to trap emission frequencies.

As modulating frequency $\omega \rightarrow 0$, this results in

$$n(\omega) = \frac{\sum_l G_{\omega,l} + \sum_k G_{\omega,k}}{\omega_r}, \tag{6.5}$$

which is the DC photoresponse, including both slow and fast processes, and for $\omega > \omega_{kh}$,

$$n(\omega) \rightarrow \left\{ \frac{\sum_l G_{\omega,l}}{\left[j\omega + \sum_i \left(\omega_{ti} - \frac{\omega_{ti}}{1 + j\omega/\omega_{ei}} \right) + \omega_r \right]} \right\}, \tag{6.6}$$

where ω_{kh} is the emission frequency of the shallowest unoccupied trap into which electrons are optically excited by photon energy E_{ph}, i.e. at energy depth E_c-(E_v+E_{ph}) below the conduction band edge (see figure 6.1). This is actually the MPC response for the fast process (b).

Thus, CPM measurement in AC mode, using a chopping frequency above ω_{kh}, will yield an absorption coefficient $\alpha_{AC} = \alpha_{(b)}$ corresponding to $\sum_l G_{\omega,l}$ and fast process (b), while the denominator of equation 6.6 is independent of the photon energy. A DC measurement will yield an absorption coefficient $\alpha_{DC} = (\alpha_{(a)} + \alpha_{(b)})$, where $\alpha_{(a)}$ arises from the slow process.

These results lead to two limiting cases, of α_{DC} and α_{AC}. At sufficiently high photon energy or at high temperatures, the inequality $\omega > \omega_{kh}$ may not be met experimentally, and the CPM measurement may yield an intermediate value for α which will contain the temperature dependence inherent in the set of poles associated with process (a).

6.3 Obtaining the DOS below and above the Fermi level

The general expression for absorption coefficient and density of states relationship can be written as (see chapter 2.8)

$$\alpha(E_{ph}) = \frac{c}{E_{ph}} \int_{-\infty}^{\infty} g_1(E) f(E) g_2(E + E_{ph}) (1 - f(E + E_{ph})) dE \tag{6.7}$$

Case (**I**) for $E + E_{ph} > E_c$, the absorption coefficient $\alpha_1(E_{ph})$ depends on transitions from occupied states below E_F into extended states from the conduction band and can be written as

$$\alpha_1(E_{ph}) = \frac{c}{E_{ph}} \int_{E_F - E_{ph}}^{E_F} g_1(E) f(E) g_2(E + E_{ph}) \left(1 - f(E + E_{ph})\right) dE \tag{6.8}$$

which results in

$$\alpha_1(E_{ph}) = \frac{c}{E_{ph}} \int_{E_F - E_{ph}}^{E_F} g_1(E) g_c(E + E_{ph}) dE\,, \tag{6.9}$$

and is directly measured by AC CPM, $\alpha_{AC} = \alpha_{(a)} = \alpha_1(E_{ph})$.

Case (**II**) for $E + E_{ph} > E_F$, the absorption coefficient $\alpha_2(E_{ph})$ depends on transitions from extended states in the valence band into localized states above E_F and is calculated as

$$\alpha_2(E_{ph}) = \frac{c}{E_{ph}} \int_{E_V - E}^{E_V} g_v(E) g_2(E + E_{ph}) dE\,, \tag{6.10}$$

which is being measured by DC CPM, $\alpha_{DC} = \alpha_{(a)} + \alpha_{(b)} = \alpha_1(E_{ph}) + \alpha_2(E_{ph})$. To obtain the DOS above the Fermi level it is possible to use the *difference* between the two measurements, $\alpha_{DC} - \alpha_{AC} = \alpha_2(E_{ph})$.

Using the simple derivative method of Pierz et al. (Pierz at al., 1985) to compute the density of states (DOS) from the absorption spectrum, assuming that $g(E_c)$, $g(E_v)$ are both step functions, the 'standard' DOS $g_1(E)$ below E_F can be obtained as

$$g_1(E) \propto d\alpha_1(E_{ph}) / dE_{ph}\big|_{E_{ph} = E_C - E} \tag{6.11}$$

and the DOS $g_2(E)$ above E_F can be calculated as follow.

$$g_2(E) \propto d\left[\alpha_{DC}(E_{ph}) - \alpha_{AC}(E_{ph})\right] / dE_{ph}\big|_{E_{ph} = E - E_V} \tag{6.12}$$

6.4 Temperature dependency of AC and DC CPM - Simulation results

Figure 6.2 shows the form of the CPM spectra obtained by Sládek and Thèye (Sládek and Thèye 1994), for DC and AC measurements at a relatively low chopping frequency of 7 Hz, and at temperatures of 300 K and 77 K. The results show a difference over the 'middle' photon energy range 0.8 eV to 1.2 eV, between α_{DC} and α_{AC} at 300 K, as predicted by the above analysis, but also the coincidence of the DC and AC spectra at low temperatures.

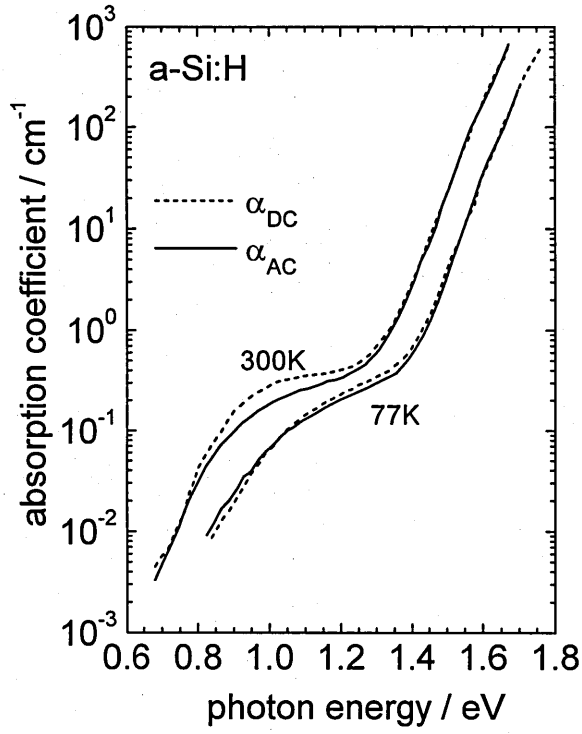

Figure 6.2 AC and DC CPM absorption spectra for a-Si:H film at 300 K and 77 K (after Sládek and Thèye, 1994).

The authors explain this second result in terms of changes in the transport process. However, the analysis presented here suggests a natural explanation. In any reasonable measurement time, at temperatures below about 150 K, emission times from states involved in process (b) for the above photon energy range, are much longer than the measurement time, so the (b) term in equation 6.4 is 'frozen out'.

Computer modelling of the absorption spectra using the present analysis bears this out. Figure 6.4 shows the CPM spectra computed for the DOS of figure 6.3, at 77 K, 300 K and 450 K. The DC case is modelled using a frequency of 10^{-9} Hz, representing a suitably lengthy measurement time. The AC limiting spectra are also shown, and the AC spectra for modulating frequency of 100 Hz. It can be seen that the '100 Hz spectrum' rises to meet the DC spectrum at 450 K, while the DC spectrum falls to meet the AC spectrum at 77 K. It is possible that other factors may influence low temperature measurement, such as changes in conduction mechanism, and wider splitting of quasi-Fermi levels, but the present explanation appears both simple and adequate.

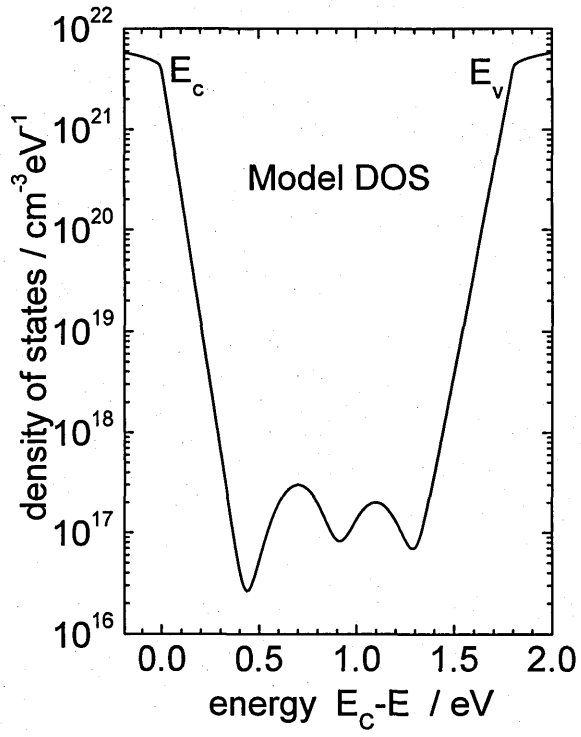

Figure 6.3 Model DOS used for CPM simulation in figure 6.4.

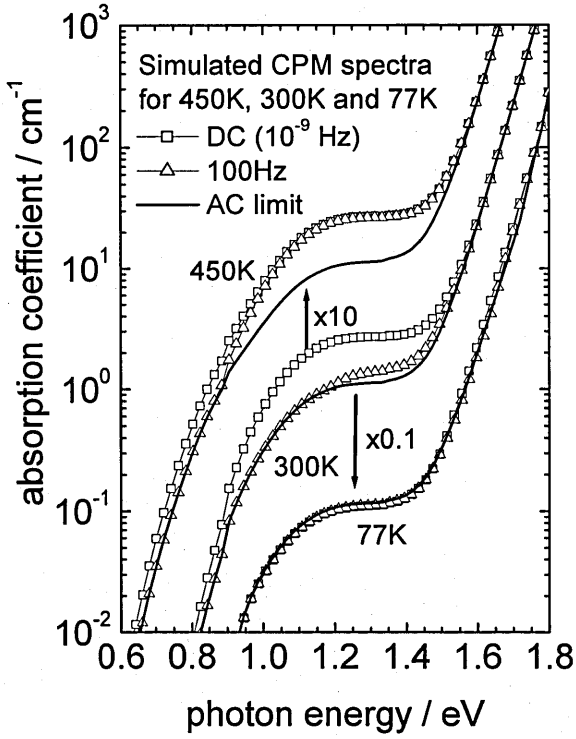

Figure 6.4 Simulated DC and AC CPM absorption spectra for DOS of figure 6.3, for 77K, 300K and 450K.

A similar effect could also be seen in the experimental results presented in chapter 5.4 for the PECVD sample in the light-soaked state, where the AC curve rises to meet the DC curve at 400 K (figure 5.10 and 5.12) and in the annealed state of the HWCVD sample where again the AC curve rises at 400K to reduce the AC-DC discrepancy as seen in figure 5.11 and 5.13. Why this effect is not noticeable for the annealed state of the PECVD sample and the light-soaked state of the HWCVD sample is not clear. However it is assumed that this depends strongly on the size and location of the defect density in the mid-gap of the material. It could also be argued that the temperature was not high enough to see this effect in the measurement results, but any temperature above 450 K would actually result in annealing the material.

6.5 DOS calculation above Fermi level – Simulation and experimental results

Figure 6.5 shows the computed DC and AC CPM spectra. The DC simulation produces a defect shoulder for photon energies below 1.4 eV, while the AC simulation continues down the 'Urbach' slope to E_{ph} = 1.1 eV. The computed DOS, using the Pierz et al. method for each spectrum, is superimposed on the model DOS shown in figure 6.6, which demonstrates a rather extreme case of a high density of unoccupied defect states above E_F (dotted curve). Figure 6.6 shows clearly that the DC case is incorrectly interpreted as a deep *occupied* set of defects below E_F, while the AC analysis is much closer to the actual DOS. Also included in figure 6.6 is the DOS obtained from the *difference* between DC and AC α spectrum, reflected across the mid-gap, to reproduce the original distribution of *unoccupied* defects.

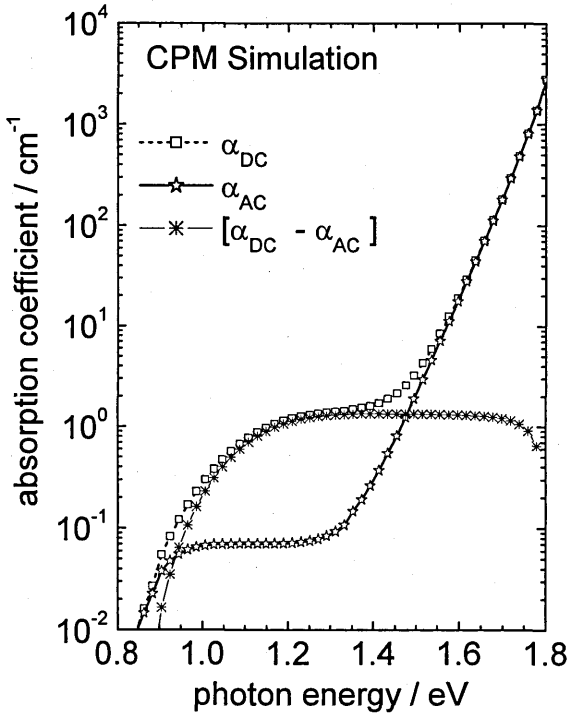

Figure 6.5 Simulated DC and AC CPM absorption spectra including DC-AC alpha for DOS shown in figure 6.6.

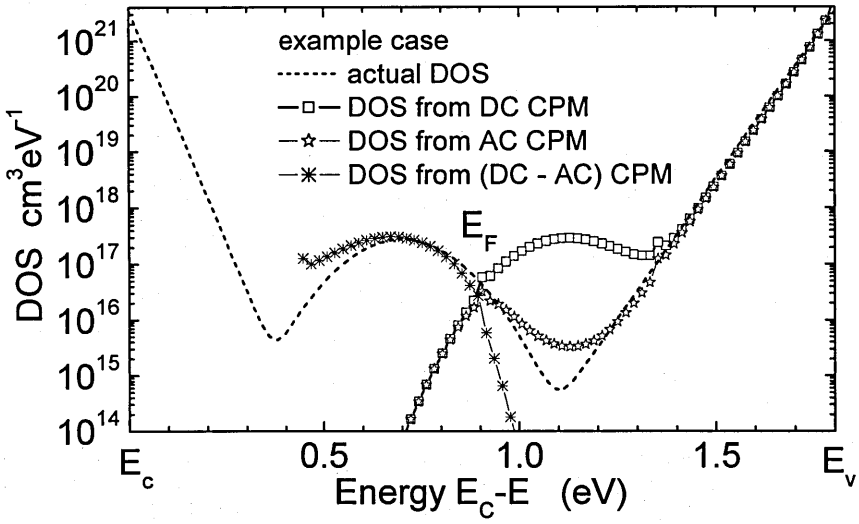

Figure 6.6 Model DOS with high density of unoccupied defects above mid-gap, with computed DOS from DC and AC CPM spectra, and from the *difference* between DC and AC spectra, demonstration that CPM can provide spectroscopy of occupied and unoccupied states.

Figure 6.7 presents the first experimental information in support of the above. The experimental DOS was calculated from the CPM results of the ISB4 PECVD sample in the annealed state at room temperature as shown in figure 5.10. Additionally the DOS obtained from TPC measurement was superimposed onto figure 6.7 to compare with the DOS obtained from the DC-AC approach. The TPC DOS was scaled vertically to match the defect density of the DOS obtained from DC-AC approach. The mobility gap E_g = 1.69 eV was obtained by using a Tauc-plot.

As a first approach the coincidence between the TPC DOS and the DC-AC DOS is remarkable. As seen in figure 6.7 for the energy range $(E_c\text{-}E)$ = 0.55 eV – 0.7 eV both DOS curves are in very good agreement but for energies $(E_c\text{-}E)$ < 0.55 eV the (DC-AC) DOS tends to higher Urbach energy values than the TPC DOS, and for energies $(E_c\text{-}E)$ > 0.7 eV the (DC-AC) DOS gives information about the density of states in the mid gap up to 0.8 eV, and including the DOS from the A-CPM nearly completing the whole mid gap energy range.

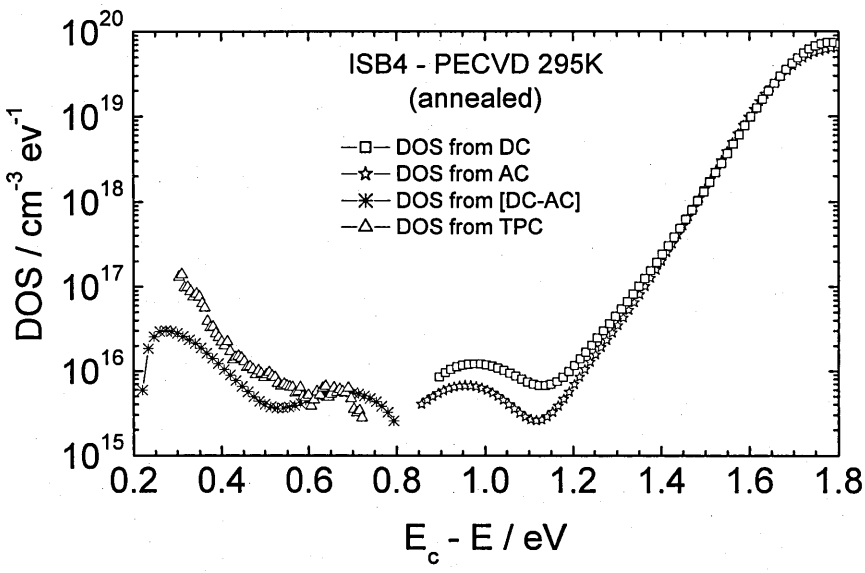

Figure 6.7 Experimental DOS for the ISB4 PECVD sample after annealing obtained from DC and AC and [DC-AC] α, with superimposed DOS from TPC measurements.

6.6 Summary

The origin of the reported differences in the absorption coefficient spectra as measured by DC and AC CPM in undoped a-Si:H, lies in 'slow' phonon assisted free electron creation, via unoccupied defects. This view is supported by an analysis of sub-gap AC photoconductivity which shows that CPM may be formally treated as super-gap MPC, with the inclusion of distributed poles in the generation rate. A consequence is that the AC CPM measurement allows a more accurate deconvolution to determine the defect DOS, and a combination of DC and AC measurements can reveal distributions of defects below and above E_F as shown in theory and experiment. Additionally, the AC CPM technique may be relatively insensitive to changes in electron lifetime. Further work is required to assess the influence of holes on this analysis.

Chapter 7 - Experimental Results Part II

7.1 Introduction

A major objective of this project was investigation of a method to produce thin film silicon material which does not suffer from degradation effects during exposure to light and therefore enable production of high stability solar cells comparable to their polycrystalline and monocrystalline counterparts. The efficiency of amorphous silicon solar cells decreases about 15 – 20 % from their initial annealed state (right after the manufacturing process) when exposed to light degradation over a few days. This degradation effect, known as the Staebler-Wronski effect, was investigated experimentally by comparison of films produced by two major deposition methods, PECVD and HWCVD. CPM measurement was the main investigation tool along with TPC and FTIR.

A further objective was an analysis of the impurity content influence, by depth profiling in HWCVD material and the influence of the filament-to-substrate distance as they determine the quality of the deposited material. The influence of the silane content during deposition on the resulting quality of microcrystalline silicon films will be presented in a separate chapter, observing the shift from amorphous to microcrystalline phase using CPM and FTIR measurements. The influence of proton irradiation on amorphous and microcrystalline films was also investigated by the CPM method. As a last part of the CPM measurement series, non-silicon material like CdTe, GaAs and multilayer films comprised of CdSe nanocrystals in an insulating matrix were measured and the usability of CPM on non-silicon materials demonstrated.

In the next two sections (7.2 and 7.3) the CPM measurement method itself was investigated; its precision, resolution and validity demonstrated.

7.2 CPM on crystalline silicon

This section will present CPM measurement performed on crystalline silicon, c-Si. The aim of these measurements is to determine the range and resolution of the CPM setup used for this project. From the literature, high quality c-Si has a band gap E_g = 1.14 eV and a defect content, actually *impurity* content, of less than 1 part in 10 billion (Neamen 2003). Due to its virtually non-existent defect density in comparison to a-Si:H the measured CPM spectrum is expected to exhibit a very rapid decrease of the absorption coefficient at about 1.1 eV.

As a sample a non-doped piece of a mono-crystalline silicon wafer (with 111 orientation) was obtained from the Institut für Physikalische Elektronik, University of Stuttgart, Germany. The thickness of the sample was 300 µm. The dark conductivity is $\sigma_0 = 8.93 \cdot 10^{-7}$ S cm^{-1} and the µτ-product is $8.92 \cdot 10^{-5}$ cm^2 V^{-1} measured at E_{ph} = 1.96 eV and $\Phi = 10^{14}$ cm^{-2} s^{-1}. The CPM measurement was performed in standard mode because the sample was too thick to be measured in transmission mode. Figure 7.1 shows the CPM result for the c-Si sample shifted to absolute scale by using α (c-Si) data from literature (Hulthén 1975).

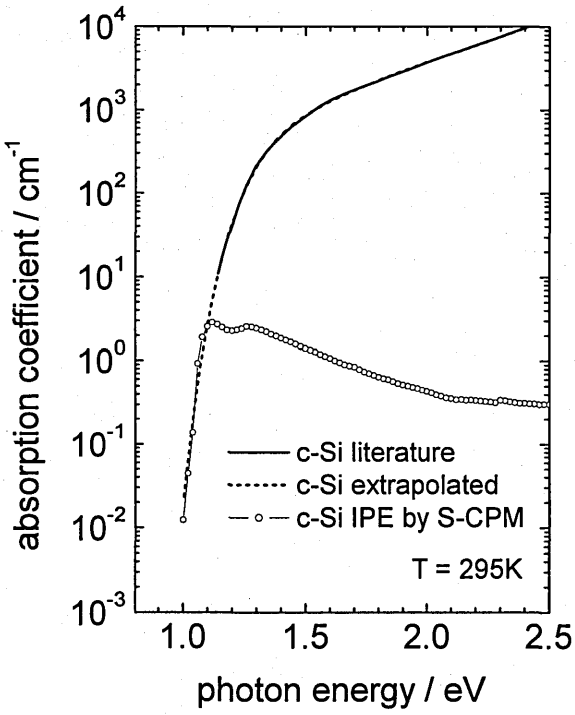

Figure 7.1 CPM measurement for c-Si sample non-doped shifted to absolute scale by using c-Si α data from literature.

Figure 7.1 shows as expected a rapid fall of the absorption coefficient at about 1.1 eV. Between the photon energies of 1 eV and 1.1 eV there is a very good agreement between the CPM result and the data obtained from literature, which were extrapolated by using a polynomial fit. For photon energies above 1.1 eV the CPM curve is already in saturation because of the thickness of the sample and therefore rendered useless for further analysis. As figure 7.1 shows, absorption coefficient data for c-Si are measurable down to 10^{-2} cm^{-1}, which is sufficient for most measurements on a-Si:H material.

7.3 Multi-CPM current and single CPM current measurements

Performing a CPM measurement with only one value for the CPM photocurrent is in most cases nearly impossible. In most cases I_{CPM} needs to be changed up to six times during the measurement until reaching the lowest photon energy (here: 0.78 eV) possible and/or losing the signal response at maximum photon flux. It is very much dependent upon the material quality to what extent in the lowest photon energy range one is able to measure the CPM spectrum. In this setup the CPM measurement was stopped when the system was not able to maintain a CPM photocurrent of 0.5 pA in AC mode. It was not possible to setup $I_{CPM} < 0.5$ pA because of signal noise.

Sladék et al showed that variation of the CPM photocurrent by 1 to 1.5 orders of magnitude during a measurement corresponds to a Fermi level shift smaller than 0.08 eV and could only cause noticeable errors in the sub-gap absorption if the I_{CPM} variations are too big (Sladék et al, 1995). Figure 7.2 shows typical raw CPM data performed in transmission mode for 'absolute' CPM on the HW159 (HWCVD) sample.

The corresponding CPM measurement with a single $I_{CPM} = 1$ pA is shown in figure 7.3. The measurement was performed in 'standard' mode and shifted to absolute scale because for $E_{ph} > 1.8$ eV only a very low photon flux is necessary to maintain the I_{CPM}, which would be too low to detect by the SiGe detector in transmission mode.

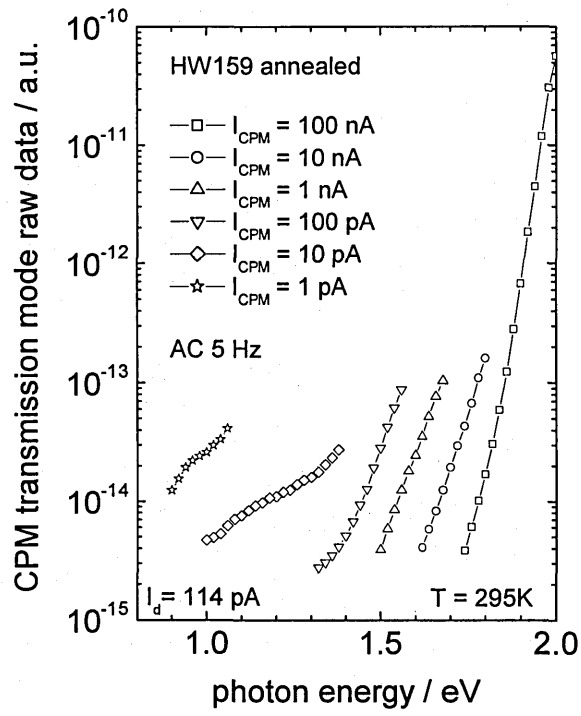

Figure 7.2 Multi I_{CPM} measurement in transmission mode before joining together and processing by the Vaněček-Ritter-Weiser method for absolute CPM.

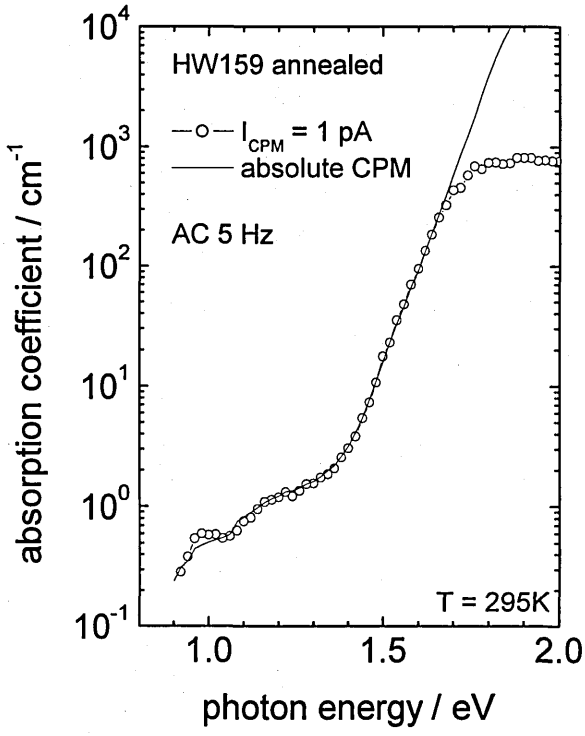

Figure 7.3 Absolute CPM result from figure 7.2 and single I_{CPM} standard CPM measurement superimposed.

The single I_{CPM} standard CPM curve in figure 7.3 shows a very good agreement with the absolute CPM curve which was calculated and 'pieced together' from the raw CPM data of figure 7.2. Figure 7.4 shows the single- and multi-I_{CPM} comparison for sample B1421 (PECVD) with thickness d = 1 μm. Both measurements are contaminated by interference fringes but still in very good agreement. The phase shift between the interference maxima and minima from absolute and standard CPM measurement can originate from a non-uniformity of the film thickness across its lateral dimensions, as has been reported by Sladék et al. In figure 7.3 interference fringes are not visible for both CPM measurement modes because the thickness of the sample is d = 3 μm.

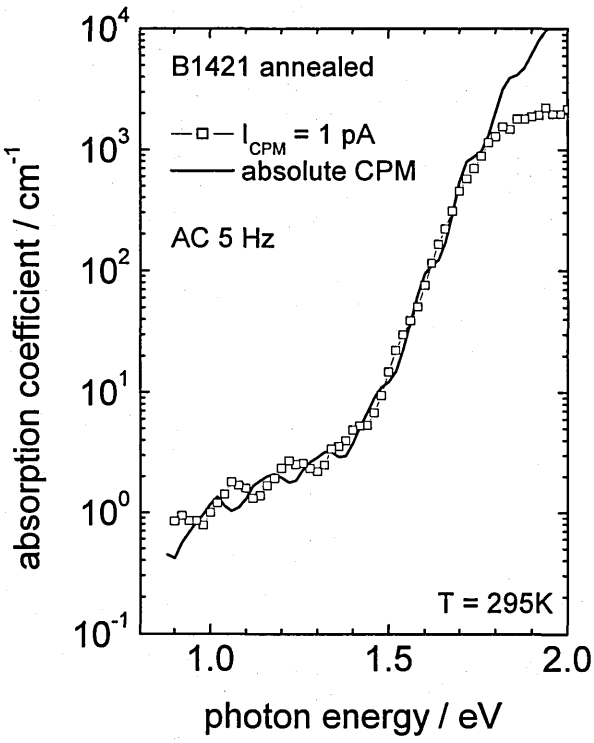

Figure 7.4 Absolute CPM and single I_{CPM} standard CPM measurement for sample B1421 (PECVD).

The results presented in figure 7.3 and 7.4 show that possible error arising from the multi CPM current method is actually very small, if not negligible, especially if interference is involved.

7.4 Comparison of PECVD & HWCVD deposited films

7.4.1 Introduction

The electronic properties of a-Si:H are strongly influenced by defects associated with the presence of dangling bonds and further, by metastable defects created by illumination. Undoped a-Si:H films can be produced at high deposition rates by the hot-wire (HWCVD) or 'catalytic' CVD method, having a smaller hydrogen content and greater electronic stability on illumination than conventional RF PECVD films (Mahan et al, 1991, Heintze et al, 1996, Itoh et al, 2001). As a part of a wider programme of commercialisation and refinement of the HWCVD technique, HWCVD and PWCVD films subjected to annealing – light soaking cycles have been investigated using transient photocurrent spectroscopy (TPC) and the absolute CPM method.

7.4.2 Material preparation

The films Hw105, HW159 and B1421 were prepared in a laboratory system in the University of Dundee, the films ISB4S2 and ISB4S4 were prepared in an industrial reactor at Intersolar UK. The sample preparation data are shown in table 7.1. For the PECVD films produced by Intersolar UK only limited preparation data were available.

Table 7.1 Sample preparation data

sample	deposition method	chamber pressure [mTorr]	substrate temperature [°C]	filament temperature [°C]	radio frequency power [W]	SiH_4 flowrate [sccm]	H_2 flowrate [sccm]	hydrogen dillution [%]	thickness [µm]	deposition time [min]
HW105	HWCVD	220	200	1500	x	8	x	0	0.38	30
HW159	HWCVD	220	200	1500	x	9.8	0.2	2	3	60
B1421	PECVD	220	~ 150	x	3	8	x	0	1.5	180
ISB4S2	PECVD	500	200	x	?	x	x	20	1.7	?
ISB4S4	PECVD	500	200	x	?	x	x	5	1.7	?

7.4.3 Sample conditioning and measurement systems

CPM measurements were performed after annealing the samples at 180°C temperature for 3h and after each exposure to simulated AM1 radiation for 1, 10, 100 and 1000 minutes. The $\mu\tau$-products were obtained at E_{ph} = 1.96 eV and $\Phi = 10^{14}$ cm^{-2} s^{1} before each CPM measurement. A voltage U = 300V was applied to each sample to create the electric field E in the gap. All measurements were performed at T = 295K. The CPM chopping frequency was 5 Hz.

The TPC measurements have been carried out by using a 4 ns pulse from a nitrogen-pumped dye laser at a wavelength of 620 nm, creating an initial carrier density of approximately 10^{15} cm^{-3}. Data were recorded typically between 1 ns and 10 s after creating the excitation with the laser pulse. The methods employed in calculating the DOS from current-time data have been described by Reynolds et al. (Reynolds et al, 2000).

7.4.4 Steady state measurements

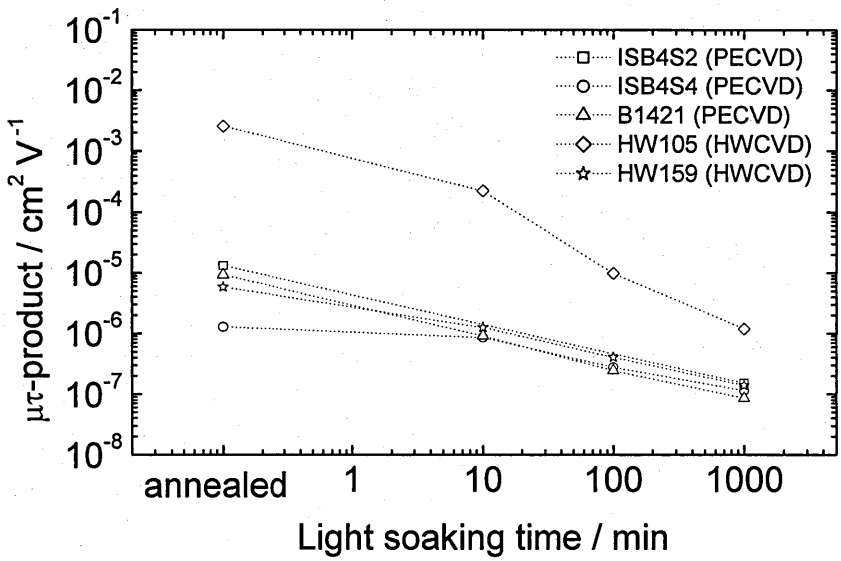

Figure 7.5 $\mu\tau$-products for the PECVD and HWCVD samples after annealing and light-soaking for 10, 100 and 1000 min under simulated AM1 conditions.

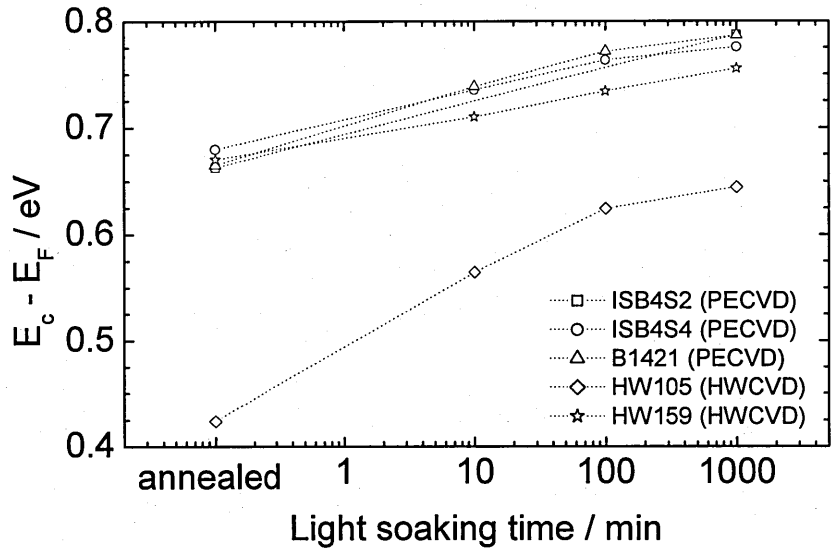

Figure 7.6 Fermi level positions for the PECVD and HWCVD samples after annealing and light- soaking for 10, 100 and 1000 min under simulated AM1 conditions.

Figure 7.5 and 7.6 presents the Fermi level positions and $\mu\tau$-products obtained for the PECVD films and are typical of literature values for intrinsic amorphous silicon (Brüggemann, 1998, Morgado, 2002). The position of the Fermi-Level relative to the conduction band edge was estimated from the measurements of the dark conductivity at room temperature by using the conductivity prefactor $\sigma_0 = 200$ S cm^{-1} as

$$E_c - E_F = -kT\left(\frac{\sigma_d}{\sigma_0}\right). \tag{7.1}$$

For the HW105 (HWCVD) film the $\mu\tau$-product is promisingly high but the position of the Fermi-level indicates clearly that the sample is inadvertently n-type. Thus the high values cannot be attributed to a fundamental improvement in electronic properties. The source of contamination has not yet been determined. As a second attempt the HW159 (HWCVD) film shows similar values to the PECVD samples for Fermi position and $\mu\tau$-product although the changes in the Fermi energy position are smaller with light-soaking time than for the PECVD samples which might indicate a better resistance against light-soaking.

7.4.5 TPC measurements results

TPC measurements were performed only for the ISB4S4 (PECVD) and HW105 (HWCVD) films after annealing and light-soaking. In the PECVD sample, the effect of light soaking is revealed in figure 7.7 as a more rapid fall in current at approx. 10^{-7} s, associated with trapping into an increased density of defects. The annealed HWCVD sample (figure 7.8) displays the shallow decay associated with transport in n-type material (Main et al, 1990). However, with increasing light soaking, E_F moves to a more intrinsic position and the decays more closely resemble the PECVD data.

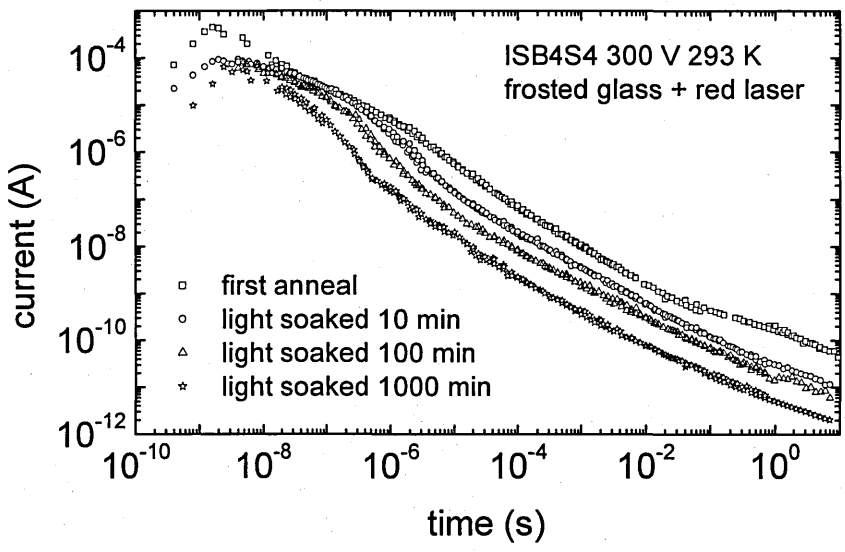

Figure 7.7 Raw TPC data obtained for the ISB4S4 (PECVD) sample after annealing and light-soaking.

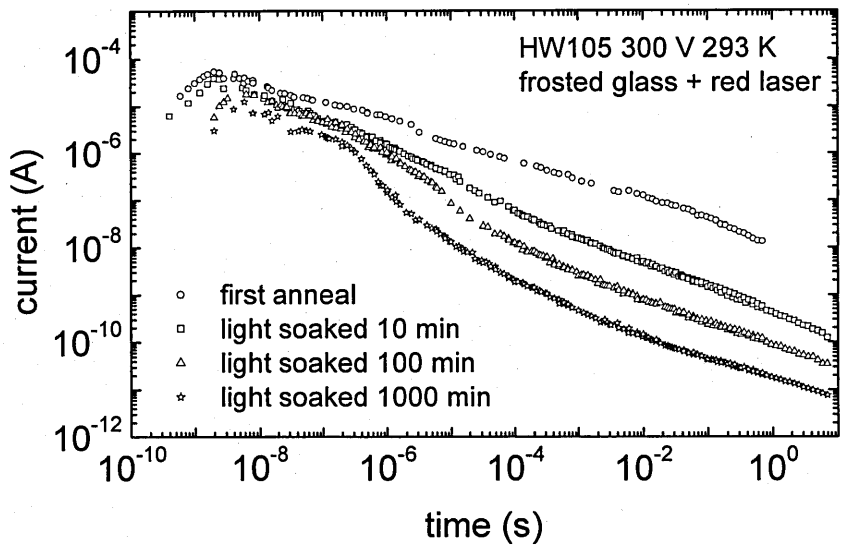

Figure 7.8 Raw TPC data obtained for the HW105 (HWCVD) sample after annealing and light-soaking.

7.4.6 Absolute CPM results

The following figure 7.9 to figure 7.14 show the absolute CPM results and the DOS calculations for the PECVD samples after annealing and light-soaking. The sample ISB4S4 shows the lowest density of defects after annealing (figure 7.9 and 7.10) and a change in the density of defects of up to a factor of 5 after light-soaking for 1000 min. The results for the sample ISB4S2 are similar to sample ISB4S4 but showing a slightly higher density of defects after annealing, which is similar after light-soaking for 1000 min (figure 7.11 and 7.12). The sample B1421, which was produced in an experimental reactor, shows similar results to its commercial produced counterparts but has the highest density of defects after annealing, which is expected because no additional hydrogen gas flow was incorporated during the deposition process (figure 7.13 and 7.14). The change in the density of defects after light-soaking is up to a factor of 4.

The increase in the density of defects during light-soaking for each PECVD sample is connected to a decrease in the $\mu\tau$-products and a Fermi-level shift towards the gap centre, which also can be observed from figure 7.5 and 7.6 (Morgado 2002).

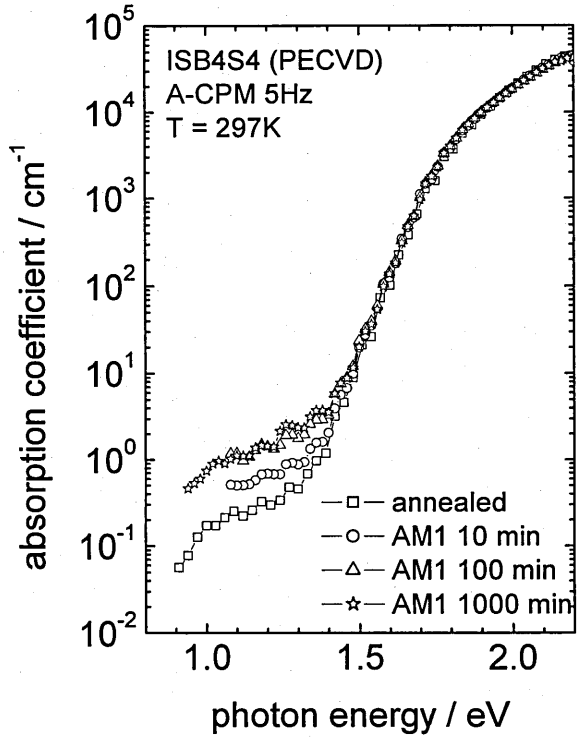

Figure 7.9 A-CPM spectra for ISB4S4 (PECVD) sample after annealing and light-soaking with simulated AM1 for 10, 100, 1000 minutes.

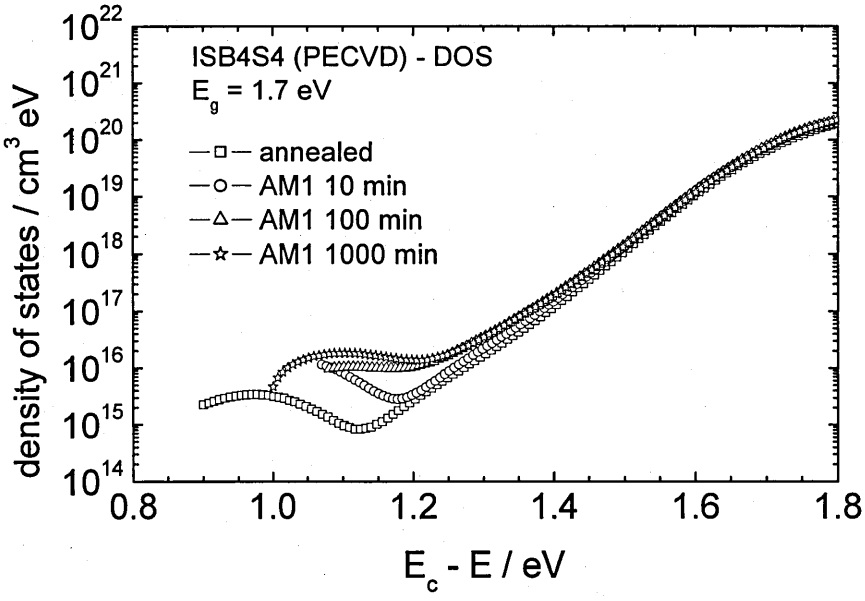

Figure 7.10 DOS calculation from the A-CPM results shown in figure 7.9 for the ISB4S4 (PECVD) sample.

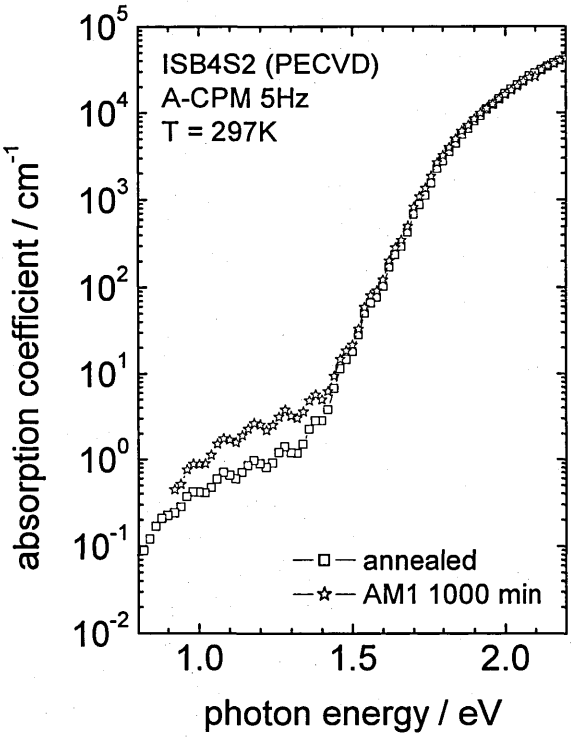

Figure 7.11 A-CPM spectra for ISB4S2 (PECVD) sample after annealing and light-soaking with simulated AM1 for 1000 minutes.

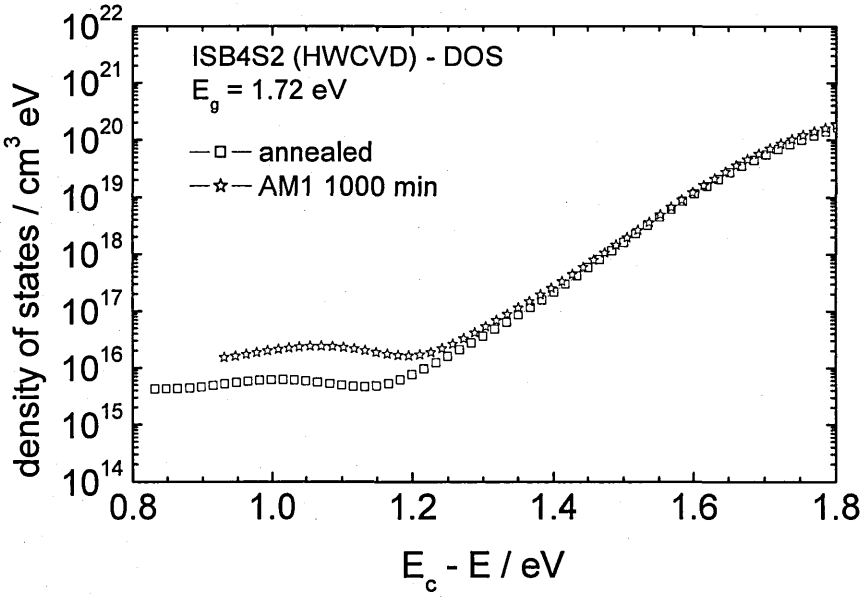

Figure 7.12 DOS calculation from the A-CPM results shown in figure 7.11 for the ISB4S2 (PECVD) sample.

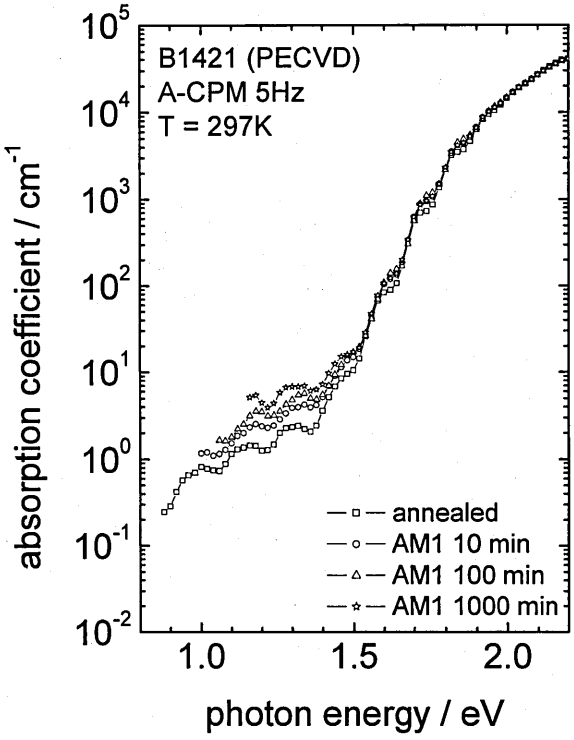

Figure 7.13 A-CPM spectra for B1421 (PECVD) sample after annealing and light-soaking with simulated AM1 for 1, 10, 100, 1000 minutes.

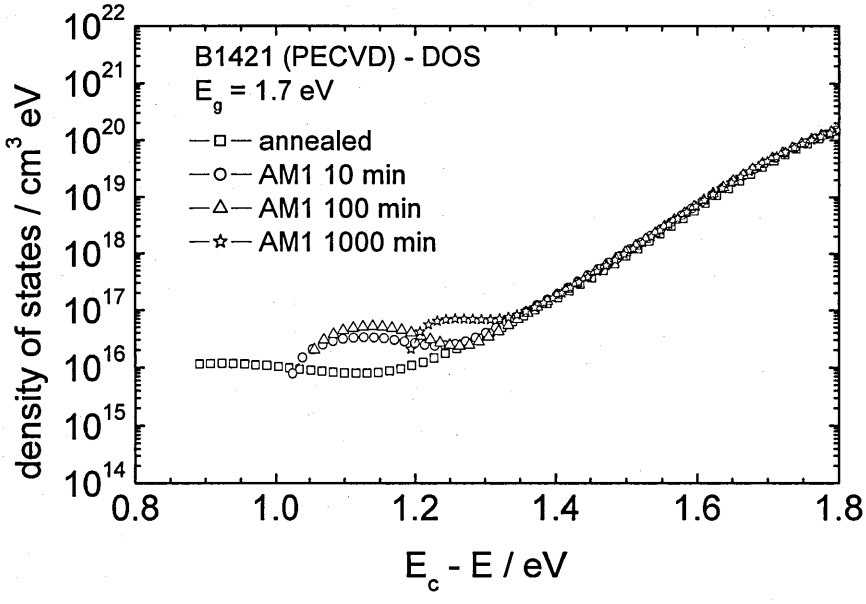

Figure 7.14 DOS calculation from the A-CPM results shown in figure 7.13 for the B1421 (PECVD) sample.

For HWCVD produced a-Si:H films it is expected that the change in the density of defects before and after light-soaking is at least equal to or smaller than for PECVD produced films. It was already shown in figure 7.5 that the $\mu\tau$-products for the HW159 (HWCVD) sample before and after light-soaking are similar to the PECVD films, where the shift in the Fermi-level position is not as great as for the PECVD samples (figure 7.6).

From figure 7.15 it appears that the quality of the HW105 (HWCVD) sample is poor in comparison to the PECVD material, with greater low energy absorption and a shallower Urbach tail. The fractional increase in absorption on light-soaking is again similar to that of the PECVD samples. Figure 7.16 shows the combined DOS profile over most of the mobility gap, with the TPC data providing the upper (conduction band CB) and CPM data for the lower (valence band VB) portion, for the ISB4S4 (PECVD) and HW105 (HWCVD) samples after annealing. Figure 7.17 shows the DOS profile after light-soaking for 1000 min.

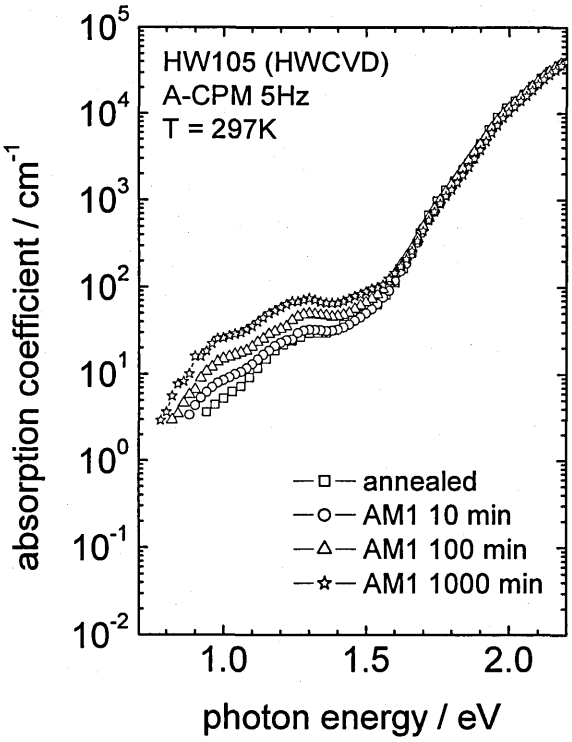

Figure 7.15 A-CPM spectra for HW105 (HWCVD) sample after annealing and light-soaking with simulated AM1 for 10, 100, 1000 minutes.

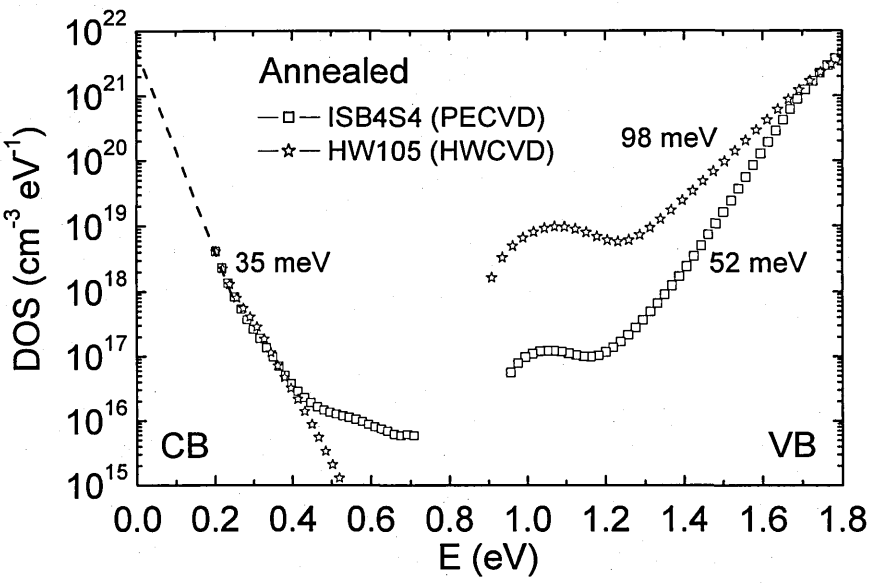

Figure 7.16 DOS plots obtained by combination of TPC and A-CPM data for the ISB4S4 (PECVD) and HW105 (HWCVD) samples after annealing.

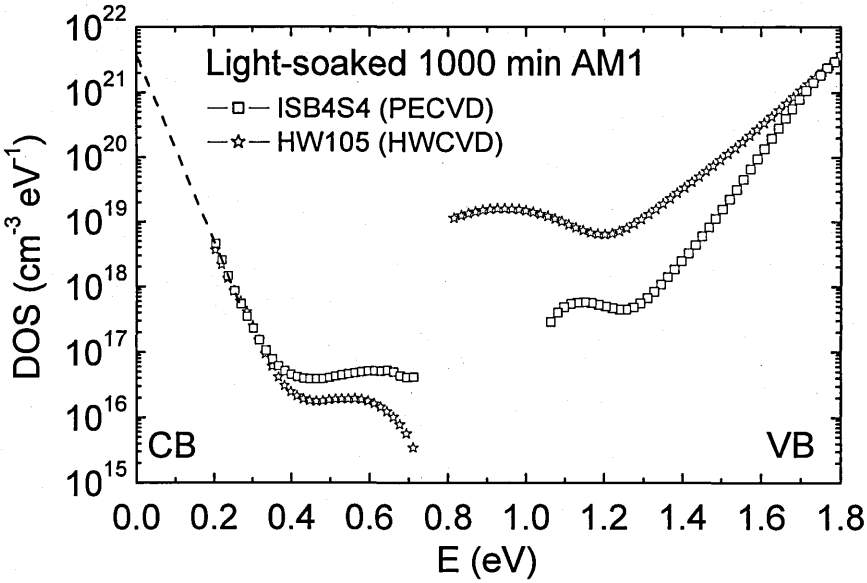

Figure 7.17 DOS plots obtained by combination of TPC and A-CPM data for the ISB4S4 (PECVD) and HW105 (HWCVD) samples after light-soaking.

The DOS scale shown in figure 7.16 and 7.17 is not calibrated. The band edge densities have been adjusted to be equal at $4 \cdot 10^{21}$ cm^{-3} eV^{-1}. In figure 7.16 the conduction band tails for HW105 and ISB4S4 samples have a similar slope, approximately 35 meV. The valence band tail for the HW105 sample is much broader, 98 meV compared with 52 meV, and the defect density is about two orders of magnitude higher. Both observations are consistent with its n-type character (Ley 1998). Light soaking the PECVD material increases the defect density by a factor of 5 over both portions of the DOS. Interpretation of the TPC result for the annealed HWCVD sample is limited by the shallow Fermi energy position (0.5 eV, see figure 7.6) as DOS calculations below E_F are invalid (Reynolds et al, 2000). After light-soaking the range of validity of the DOS extends to 0.65 eV, the TPC data indicate similar defect densities in both HWCVD and PECVD materials. This contrasts markedly with the CPM data. As the energy regions probed do not overlap, the defect density could increase very rapidly in the HWCVD material between 0.6 and 0.8 eV, in accordance with the defect pool model which predicts a large D^- contribution in n-type material deep in the gap.

Figure 7.18 shows the absorption spectrum for the HW159 (HWCVD) sample, which has similar electronic properties to the PECVD samples shown in figure 7.5. In contrast to the HW105 sample no evidence of n-type character could be observed. The absorption coefficient at low photon energies for the annealed state is similar to the commercially produced PECVD samples, which indicates a good intrinsic material. The increase of the defect density after light-soaking for 1000 min is about a factor of 2.5. The fractional increase in absorption on light-soaking is smaller than for the PECVD samples. Similar results can be obtained from the DOS plot shown in figure 7.19, where the defect density is in the same order of magnitude as for the commercially produced PECVD samples before and after light-soaking.

Due to DC and AC frequency dependent CPM measurement, described in chapter 5 & 6, the HW159 (HWCVD) film was annealed and light-soaked (AM1, 1000 min) for two more times. The results are presented in figure 7.20 and 7.21.

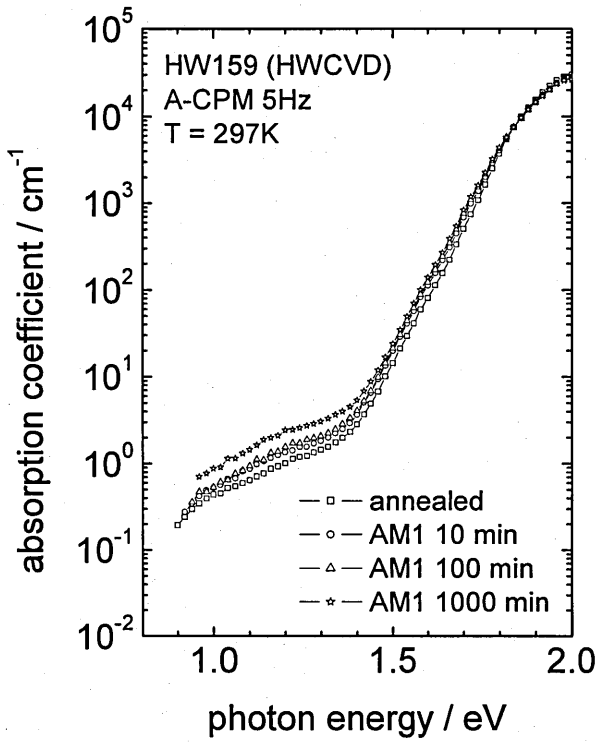

Figure 7.18 A-CPM spectra for HW159 (HWCVD) sample after annealing and light-soaking with simulated AM1 for 1000 minutes.

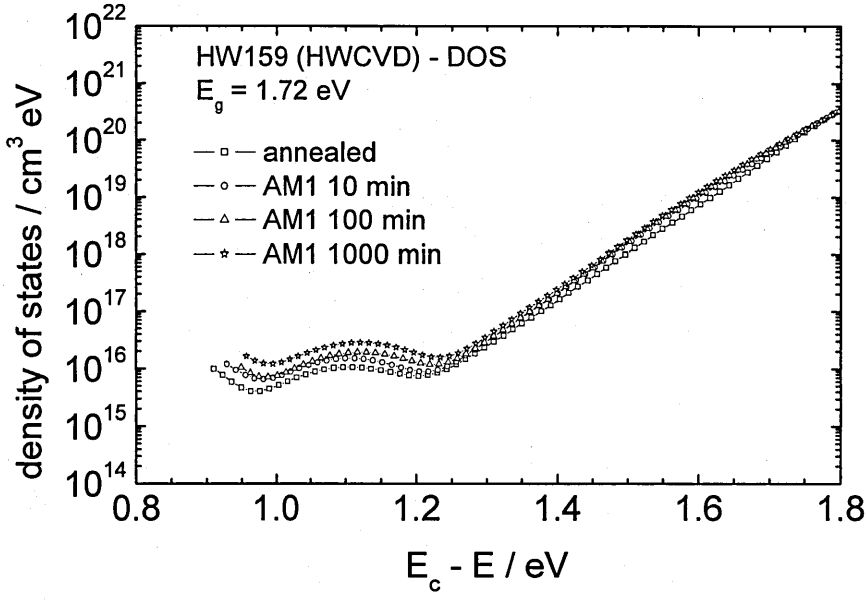

Figure 7.19 DOS plot for the HW159 (HWCVD) sample obtained from CPM data shown in figure 7.18.

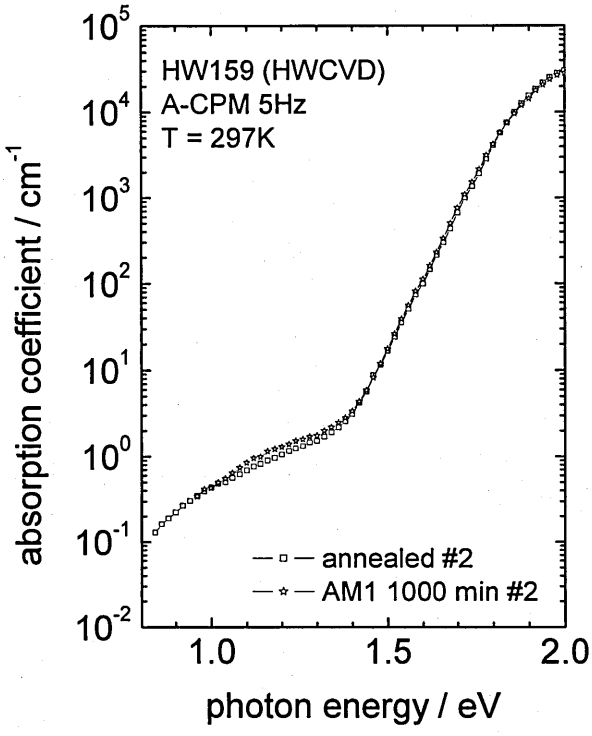

Figure 7.20 A-CPM spectra for HW159 (HWCVD) sample after second time annealing and light-soaking with simulated AM1 for 1000 minutes.

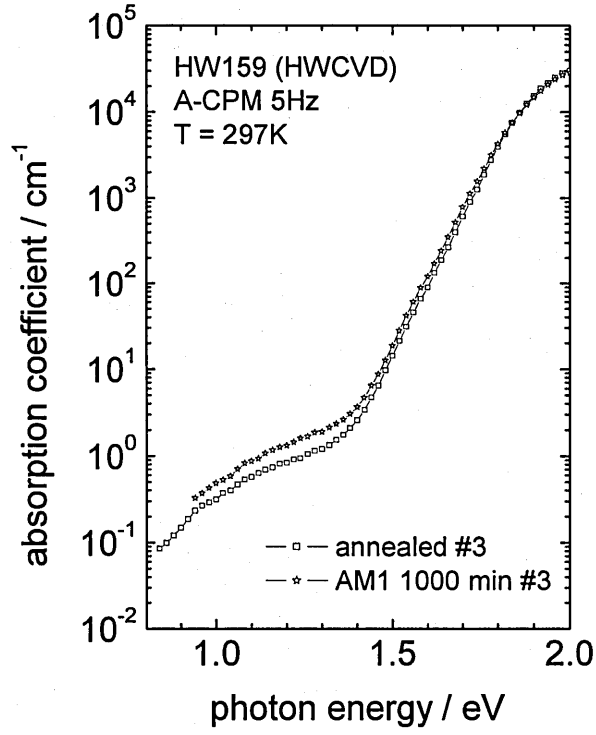

Figure 7.21 A-CPM spectra for HW159 (HWCVD) sample after third time annealing and light-soaking with simulated AM1 for 1000 minutes.

The figure 7.20 shows the absorption spectrum after the second annealing and light-soaking. There is only a very small difference visible in the defect part between both absorption curves. One can assume that the sample was not properly annealed and did not return to its initial state, that the light-soaking procedure was less than 1000 min or that the simulated AM1 radiation was incorrect. Figure 7.21 shows the absorption spectrum after the third annealing and light-soaking. The difference in the defect part here is indeed much smaller than that shown in figure 7.18 which shows the absorption spectrum after the first annealing and light-soaking, but not as small as in figure 7.20. The author assumes that for the result presented in figure 7.20 either the light-soaking time was less than 1000 min or the AM1 setup calibration was incorrect. However, a similar pattern can be obtained from the $\mu\tau$-products, which never return to initial values after the annealing and light-soaking cycle as shown in figure 7.22. The same result can be obtained for the Fermi-level position too, where the difference between the annealed and light-soaked state becomes smaller. One can conjecture that after light-soaking not only were additional defects created but also that this could have caused a rearrangement of defects, causing a relaxation of the amorphous structure which then, after the next annealing process, leaves the material with a slightly higher defect density than at its initial state. In this way the sample becomes increasingly resistant to light soaking until it reaches equilibrium.

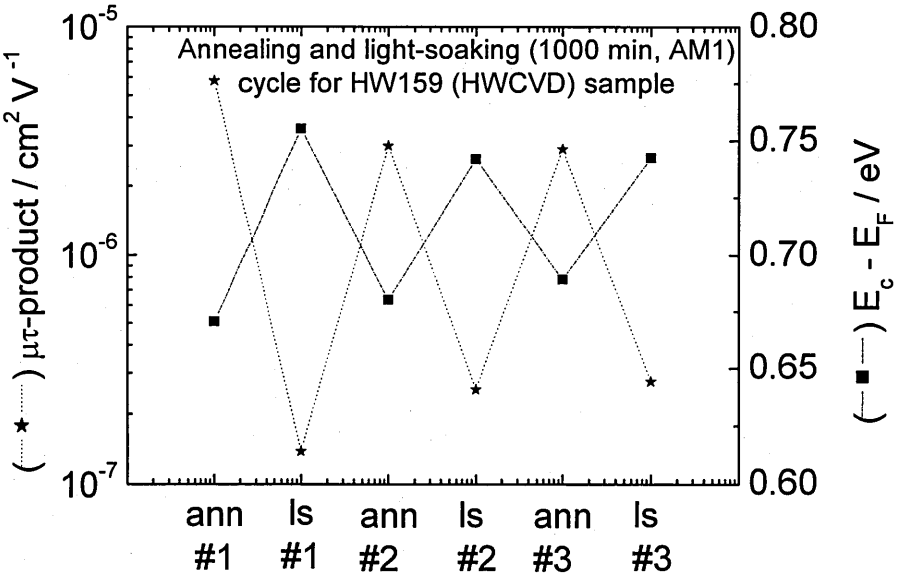

Figure 7.22 $\mu\tau$-products and Fermi-level position after each annealing and light-soaking cycle starting from left side of the diagram.

7.5 Depth profiling and the effect of contamination on the photo-electrical properties of a-Si:H films produced by HWCVD

7.5.1 Introduction

The HWCVD deposition process consists of at least three stages; the creation of reactive species, their diffusion in the substrate direction, and their incorporation into a growing silicon film on the substrate (see chapter 1.33). It has been widely accepted that the reactive species involved in film growth are the same radical precursors involved in the PECVD process. Recent work, however, on the tungsten siliconizing process (Karatyan 1997) suggests a more complex process at the surface of the hot wire involving ultimately the growing of a thin melted layer on the wire and, as a result of this, the evaporation of additional higher energy silicon atoms toward the substrate.

Moreover, tungsten wire is a potential source of contamination through outgassing, producing oxygen and carbon species. To investigate the consequences for film quality, infrared spectroscopic data are correlated here together with conductivity results and absolute CPM measurement data in an attempt to understand the physical processes involved in the growth of tungsten hot-wire deposited hydrogenated amorphous silicon.

7.5.2 Sample preparation and experimental methods

The a-Si:H films (HW98, HW131) in this study were deposited by the HWCVD method in a radial flow reactor. The tungsten wire was 0.25 mm in diameter which was used as the filament at a distance of 15 mm from the substrates. The deposition conditions are displayed in table 7.2.

FTIR results were obtained using a single beam Mattson 7000 spectrometer in the range of wavenumbers 400-5000 cm^{-1}. Absorption measurements were performed by the absolute CPM method. The voltage applied to sample was U = 300 V. $\mu\tau$-products and photoconductivity data were obtained at $\Phi = 10^{14}$ cm^{-2} s^{-1} at E_{ph} = 1.96 eV.

Table 7.2 Sample preparation data

sample	deposition method	chamber pressure [mTorr]	substrate temperature [°C]	filament temperature [°C]	SiH_4 flowrate [sccm]	thickness [μm]	deposition time [min]
HW98	HWCVD	220	300	1500	8	3.6	30
HW131	HWCVD	220	200	1500	8	1.35	30

7.5.3 Experimental results

The model of Karatyan et al, 1997, postulates that the initial processes on the surface of a hot tungsten wire exposed to silane involve the creation of thermally dissociated radicals with the subsequent production of a silicide coating from which the atomic species evaporate. To study this effect, the electronic and optical structure of the HWCVD film was compared at different depths into the film. Depth profiling by chemical etching shows particular features in the bulk and at the surfaces of the films. First, however, the validity of the siliconizing model of this case has to be established.

SEM studies of the cross section of tungsten filaments have shown that a thick silicide is formed on the wire. When a previously used filament is used as an evaporation source in the absence of silane gas at normal filament temperatures, it produces films that are highly defective, with activation energy in the range 0.7 - 0.8 eV, dark conductivity of $5x10^{-10}$ S cm^{-1} and little photoconductive response. FTIR studies in figure 7.21 show that the hydrogen bonding configuration is predominantly SiH_2.

As the silicide material continually grows on the wire it is likely that this material is incorporated into films produced by hot wire, at a rate dependent on the rate of formation of the silicide, and should therefore influence the electronic properties. As deposition proceeds a thick silicide is formed that evaporates and incorporates atomic or poorly hydrogenated silicon fragments into the growing film.

This effect on hot-wire deposition has been investigated by carrying out some depth profiling studies using 'wet chemical etching' on films grown at T_f = 1500 °C.

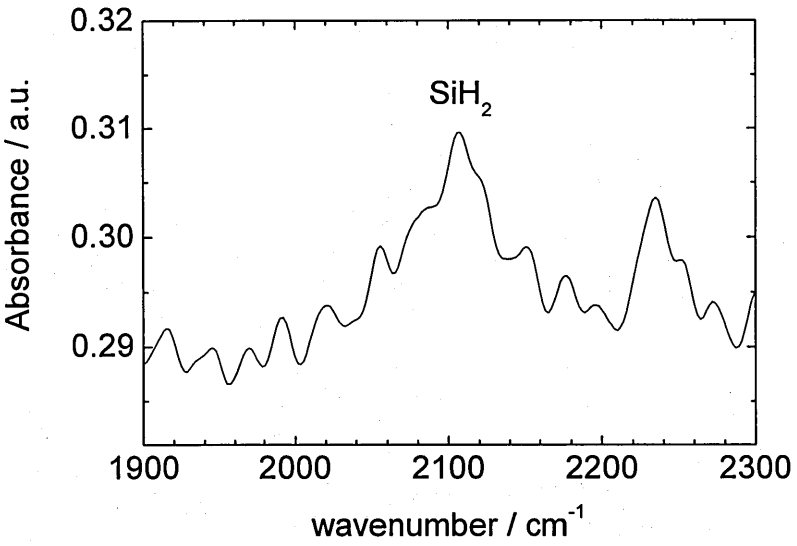

Figure 7.23 FTIR spectrum for a-Si:H film HW98, deposited from coated tungsten wire.

The oxygen and carbon concentration have been measured as a function of film depth by FTIR (Wolfe et al, 2000), which results in a dramatic decrease in impurity incorporation as the deposition proceeds. Figure 7.24 shows both the carbon and oxygen concentrations in the film.

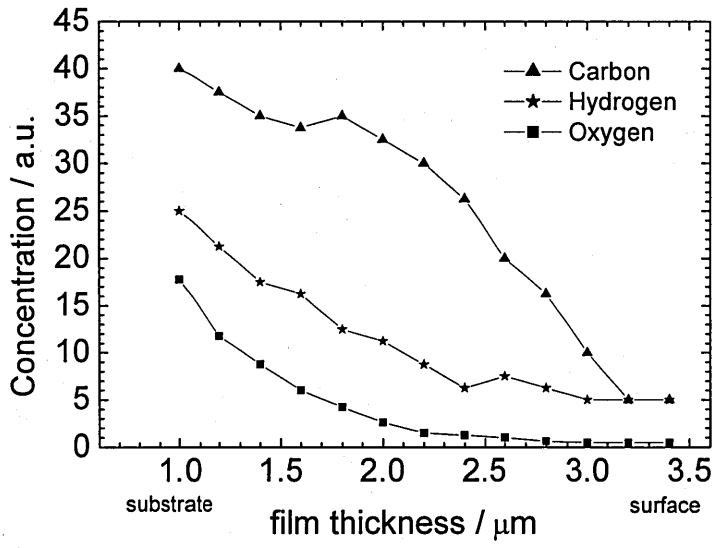

Figure 7.24 Concentration profile of carbon, hydrogen and oxygen in the film.

The hydrogen, carbon and oxygen concentrations decrease during growth (figure 7.24) but carbon is always present. Initially a decrease in the number of oxygen recombination centers causes an increase in the photoconductivity and $\mu\tau$-product (figure 7.25). Subsequently the photoconductivity and $\mu\tau$-product falls, even though the impurity concentrations are falling, as the silicon flux from the hot-wire (tungsten filament) becomes more evaporative in nature. At the lowest impurity content, the photoconductivity and $\mu\tau$-product remains low due to the changed growth mechanism.

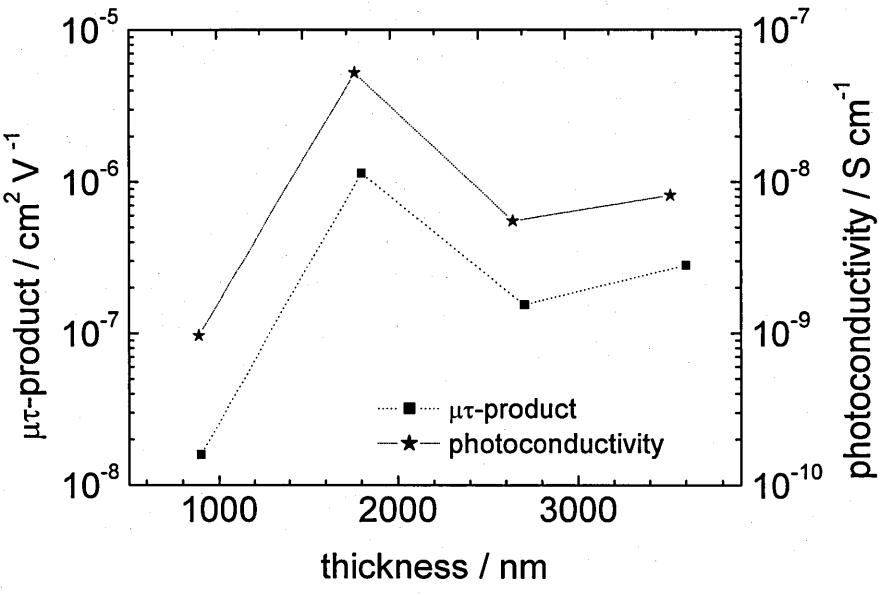

Figure 7.25 Photoconductivity and electronic performance results through the film.

A balance between the initial low film quality and the growing contribution of defective material produced by the evaporative flux from the siliconized wire results in an optimum growth window for relatively cool filaments.

The absorption coefficient from the CPM measurement is shown in figure 7.26. It can be seen that at a thickness of 1.8 μm for optimum photoconductivity figure 7.26 shows the lowest absorption curve and hence the lowest defect density of states.

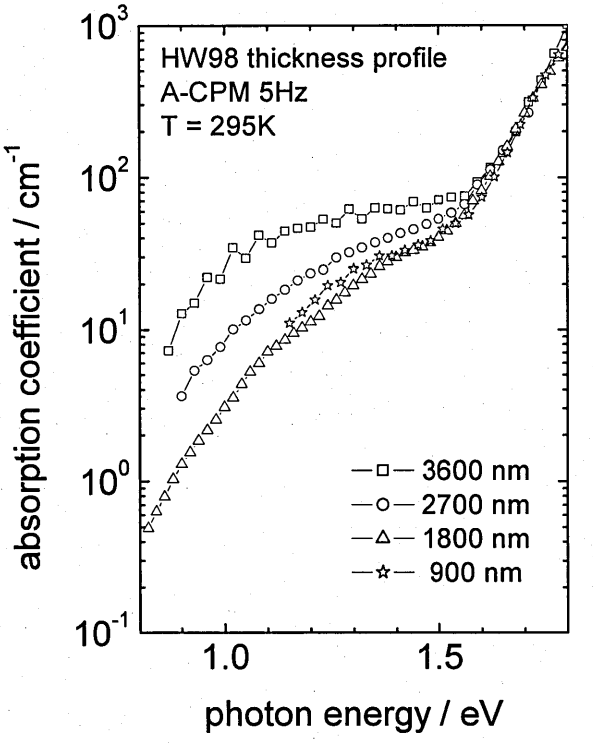

Figure 7.26 Absorption spectra for the HW98 thickness profile from A-CPM measurements.

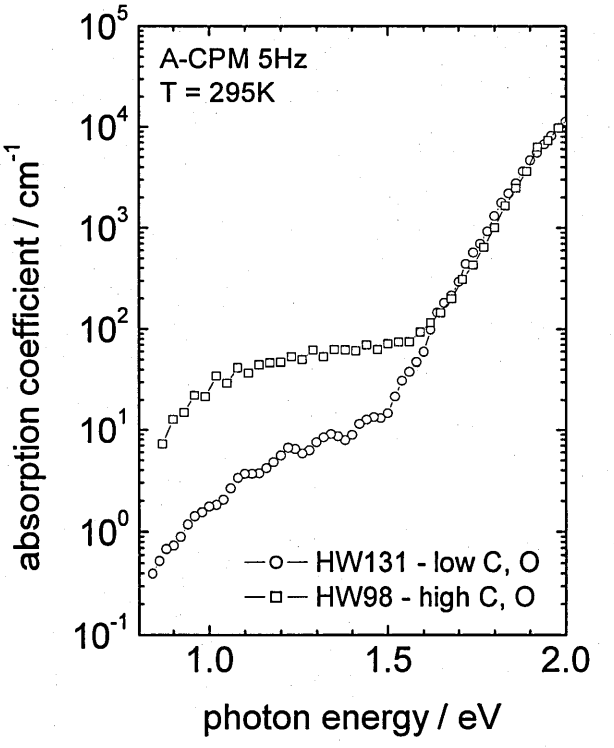

Figure 7.27 CPM results for a sample (HW98) with high impurity concentration (C, O) and with low impurity concentration (HW131).

Figure 7.27 shows a comparison between a sample containing a low level of oxygen and carbon (HW131) contamination and with a contaminated one (HW98), as presented in Table 7.2 by using absolute CPM measurement. The absorption spectra shows increased absorption values for the high level contaminated sample (HW98) in the defect tail at photon energies $E_{ph} < 1.6$ eV.

7.6 Connection between the 'filament to substrate' distance and the quality of HWCVD deposited films examined by CPM

7.6.1 Introduction

Producing high quality HWCVD material not only depends on parameters like filament temperature, chamber pressure, silane gas flow, hydrogen dilution, substrate temperature, etc., it also very much depends on the layout of the deposition chamber, the filament orientation and the distance between the tungsten filament and the substrate. In this chapter in particular, the 'filament to substrate' distance is of interest (also referred to as 'catalyzer to substrate' spacing in the literature). There is actually no existing recipe to achieve a spacing for which the HWCVD deposited film has the best qualities. It very much depends on the layout of the deposition chamber which mostly is designed as: substrate heater → substrate holder → substrate → shutter → tungsten wire (hot-wire). The gas inlet is either from behind the hot-wire towards the substrate (Iiduka et al, 1997, Itoh et al, 2001) or onto the hot-wire parallel to the substrate surface (Heintze et al, 1996). Iiduka et al reported using about 4 cm and Itho et al reported using 6 cm for the 'filament to substrate' spacing. Heintze et al varied their size of spacing and found an optimum value for $\Delta\sigma$ and $\alpha(E_{ph})$ at about 2 cm.

7.6.2 Sample preparation and experimental methods

The film HW200 was deposited under the following conditions: chamber pressure of 100 mTorr, a filament temperature as measured by a optical pyrometer of T_f = 1800 °C, substrate temperature T_s = 400 °C, flow rate of silane gas of 9.8 sccm, and hydrogen gas flow of 0.2 sccm. The deposition time was 30 min. As a substrate, Corning 7059 glass was

used. Figure 7.28 shows a schematic diagram of substrate and hot-wire position in the deposition chamber and the expected film growth relative to the hot-wire.

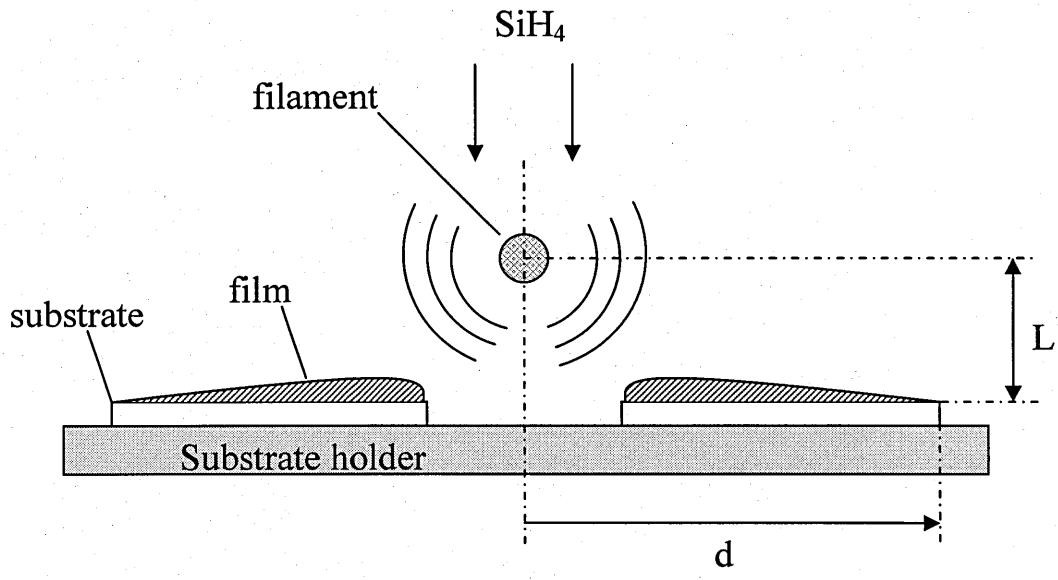

Figure 7.28 Schematic diagram showing the arrangement of the filament and the substrates in the deposition chamber of the laboratory system used.

In the current deposition setup shown in figure 7.28, a tungsten wire with 0.25 mm diameter was used as the filament and the 'filament to substrate' spacing '*L*' was set to 15 mm. After the deposition several Cr contacts were deposited at a certain position '*d*' onto the film.

At this point some additional explanation for the right meaning of the 'filament to substrate' spacing, which is here described with '*L*', should be given. In the publication from Heintze at al, Itoh at al and Iiduka et al the 'filament to substrate' spacing was determined as described in figure 7.28 with the parameter '*L*', where Matsumura (Matsumura 1998) used the direct 'substrate to catalyser' distance for '*L*' and should be referred here as 'L_M' (figure 7.29), assuming the hot-wire as a line catalyser, where the decomposed species should spread cylindrically and the flux density of species emitted from the catalyser are expected to be proportional to $1/L_M^2$ for low gas flow pressures $P_g < 1$ Torr.

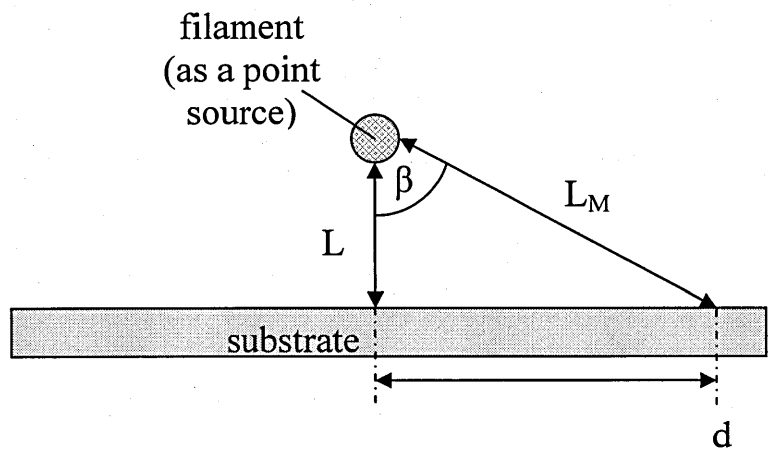

Figure 7.29 Diagram explaining the definition of the 'substrate to filament' spacing (L) and distance (L_M).

7.6.3 Results and discussion

Table 7.3 presents a summary of the experimental results for the HWCVD sample HW200 depending on the 'substrate to filament' spacing L and distance L_M, for thickness, α(1.2 eV), photoconductivity, dark conductivity, and $\mu\tau$-products.

Table 7.3 Experimental results for the HW200 (HWCVD) film

sample	position 'd' [mm]	direct 'filament to substrate' distance [mm]	thickness [nm]	alpha (1.2 eV) [cm^{-1}]	photo conductivity [S cm^{-1}]	dark conductivity [S cm^{-1}]	$\mu\tau$ - product [$cm^2 V^{-1}$]
HW200_02	36.6	39.6	4100	18.1	2.28E-08	1.94E-09	8.35E-07
HW200_03	45.2	47.6	2200	5.3	7.20E-08	7.27E-10	1.42E-06
HW200_04	54.2	56.2	1000	3.7	2.52E-07	1.36E-09	2.51E-06
HW200_05	63.6	65.3	400	4.2	4.65E-07	2.07E-09	2.19E-06
HW200_06	73.1	74.6	210	8.4	1.43E-06	2.79E-08	4.73E-06

Table 7.3 shows the best value for the absorption coefficient at E_{ph} = 1.2 eV at the position d = 54.2 mm. This corresponds to the best $\mu\tau$-product too, except the last result for d = 73.1 mm, where the $\mu\tau$-product rises again (figure 7.30). It is also seen that the photoconductivity and the dark conductivity increase steadily before rapidly rising from d = 63.6 mm to 73.1 mm, where the thickness of the sample is only 210 nm. This could be

explained by contribution from impurities as described in section 7.5 which result in a higher defect density.

Figure 7.30 shows the $\mu\tau$-products and the thickness of the film depending on the film position *d* and figure 7.31 shows the absorption coefficient spectra at these positions.

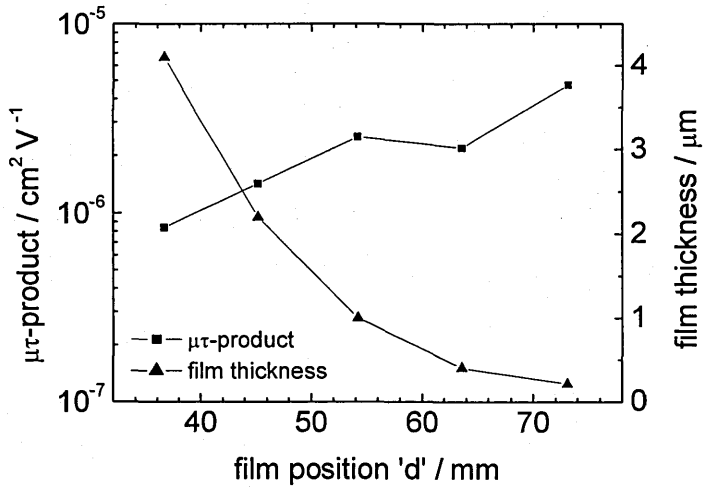

Figure 7.30 $\mu\tau$-products and film thickness as a function of the film position 'd'.

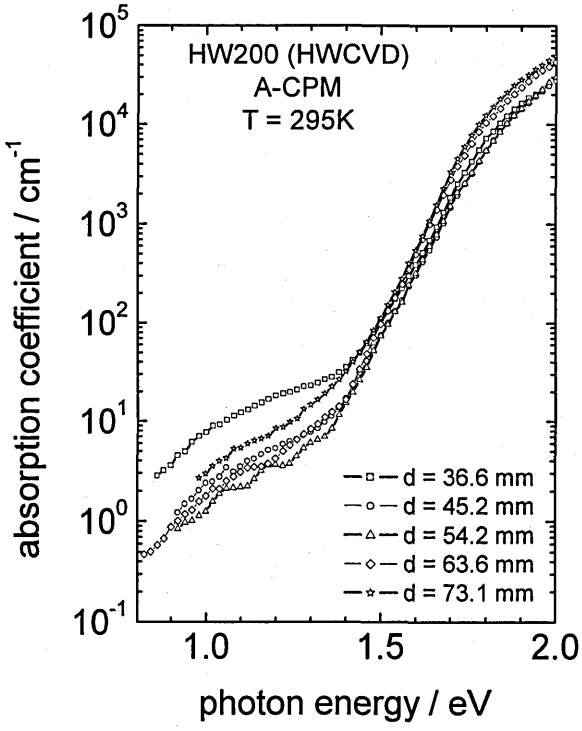

Figure 7.31 Absorption coefficient spectra for the HW200 sample obtained by A-CPM at film position '*d*'.

As reported by Heintze et al the thickness distribution follows a circular symmetry around the hot-wire which falls off as $cos^3\beta$ towards the film edge similar to the distribution of film precursors from an isotropic point source. Figure 7.31 shows the distribution of the absorption coefficient spectra for each position *d*. At the position d = 54.2 mm the absorption curve shows the lowest values for α in the defect region, which corresponds to a film thickness of 1000 nm. Getting closer towards the hot-wire the thickness increases by 4 times and α changes by one order of magnitude which indicates highly stressed material due to high thermal radiation from the hot-wire. Further away from the hot-wire the thickness decreases to 410 nm and the defect part of the absorption curve rises by a factor of 5. The $\mu\tau$-product, the dark conductivity and the photoconductivity are significantly increased at this position which indicates influences from contamination during the deposition process.

For the HWCVD deposition technique to be competitive and/or superior to the PECVD deposition method it is very important, even essential to produce large area films with a homogenous thickness and equally distributed optoelectronic film properties. An attempt to achieve this goal is to use an array of short tungsten filaments spaced in such a way by taking its point source character into account, where a good overlap of the best part of the film properties can be provided (Heintze et al). The solution used by Matsumura, Itoh et al and Iiduka et al is a coiled hot-wire array, where the total length of the wire is up to 400 cm able to cover a deposition area of 100 cm^2.

7.7 Microcrystalline silicon deposited by PECVD and HWCVD – Silane Concentration (SC) series

7.7.1 Introduction

Because of the potential of HWCVD deposited amorphous silicon films this method can also be applied to produce microcrystalline silicon films by decreasing the silane concentration '*SC*' (silane to hydrogen gas flow ratio $[SiH_4]/[SiH_4+H_2]$) during the deposition process. This effect has been reported by several groups - that by changing *SC*, the deposition of Si material can be shifted from the amorphous to the microcrystalline phase (Guillet et al, 2000, Brüggemann et al, 2000, Finger et al, 2001, Klein et al, 2001).

In this study the dependency between the silane concentration and the opto-electronic and structural properties of microcrystalline μc-Si:H films produced by PECVD and HWCVD, will be investigated.

7.7.2 Sample preparation and experimental methods

The first sets of sample, kindly given by Forschungszentrum Jülich, are microcrystalline silicon films of thickness 0.4 - 0.8 μm deposited on Corning glass in a UHV VHF PECVD system operating at 95 MHz, with a substrate temperature of 185 °C, chamber pressure of 0.3 Torr and RF power of 5 W. A series of films was produced by varying *SC* between 3.0% and 6.3%. Electrical contacts of length 1 cm and separation 0.05 cm were deposited to form a gap cell. Table 7.4 shows a summary of the deposition parameters for the samples produced.

Table 7.4 Deposition parameters for the PECVD sample series

sample	deposition method	chamber pressure [Torr]	substrate temperature [°C]	Silane Concentration [%]	thickness [μm]
00c354	VHF PECVD	0.3	185	3	0.41
00c341	VHF PECVD	0.3	185	3.7	0.55
00c348	VHF PECVD	0.3	185	4.3	0.6
00c345	VHF PECVD	0.3	185	6.3	0.8

The second set of samples, kindly provided by University of Dundee, was produced using the HWCVD deposition method, and are amorphous and microcrystalline films deposited on Corning glass, at a chamber pressure of 0.1 Torr, filament temperature of 1700 °C, substrate temperature of 400 °C. Electrical contacts of length 0.5 cm and separation 0.1 cm were deposited to form a gap cell. Table 7.5 shows the variation of the silane concentration and deposition parameters for the films produced.

Table 7.5 Deposition parameters for the HWCVD sample series

sample	deposition method	chamber pressure [Torr]	substrate temperature [°C]	filament temperature [°C]	SiH_4 flowrate [sccm]	H_2 flowrate [sccm]	Silane Conc. (SC) [%]	deposition time [min]	thickness [μm]
HW220	HWCVD	0.1	400	1700	0.2	9.8	2	60	0.7
HW219	HWCVD	0.1	400	1700	1	9	10	50	0.7
HW224	HWCVD	0.1	400	1700	4	6	40	30	0.85
HW223	HWCVD	0.1	400	1700	7.5	2.5	75	30	2
HW222	HWCVD	0.1	400	1700	9	1	90	30	3

FTIR results were obtained using a single beam Mattson 7000 spectrometer in the range of wavenumbers 400-5000 cm^{-1} (only for the HWCVD series). Absorption measurements were performed by the absolute CPM method. The voltage applied to samples was U = 300 V. $\mu\tau$-products and photoconductivity data were obtained at $\Phi = 10^{14}$ cm^{-2} s^{-1} at E_{ph} = 1.96 eV.

7.7.3 Experimental results

In table 7.6 experimental results for photoconductivity, dark conductivity, absorption coefficient at E_{ph} = 1.2 eV, and $\mu\tau$-products are presented for the VHF PECVD samples, listed in table 7.4. From Table 7.6 and figure 7.32 a decreasing $\mu\tau$-product and a tendency of decreasing α(1.2 eV) with increasing silane concentration can be obtained as reported in literature. Similarly, trends are also discerned for the photo- and dark conductivity. All samples have very similar optoelectronic properties and show a highly crystalline fraction with a very low amorphous contribution (figure 7.33).

Table 7.6 Experimental results for the VHF PECVD series.

sample	silane concentration [%]	thickness [nm]	alpha (1.2 eV) [cm^{-1}]	photo conductivity [S cm^{-1}]	dark conductivity [S cm^{-1}]	μτ - product [$cm^2 V^{-1}$]
OOC354	3	0.41	19	3.12E-07	1.38E-06	5.89E-06
OOC341	3.7	0.55	17.2	9.28E-08	2.15E-07	1.70E-06
OOC348	4.3	0.6	17.9	4.55E-08	4.58E-08	8.57E-07
OOC345	6.3	0.8	15.9	3.75E-08	1.43E-08	6.66E-07

The $\mu\tau$-products and the conductivity results obtained for the VHF PECVD deposited μc-Si:H films are similar to the results from literature as mentioned above and from Brüggemann et al (Brüggemann et al, 1999).

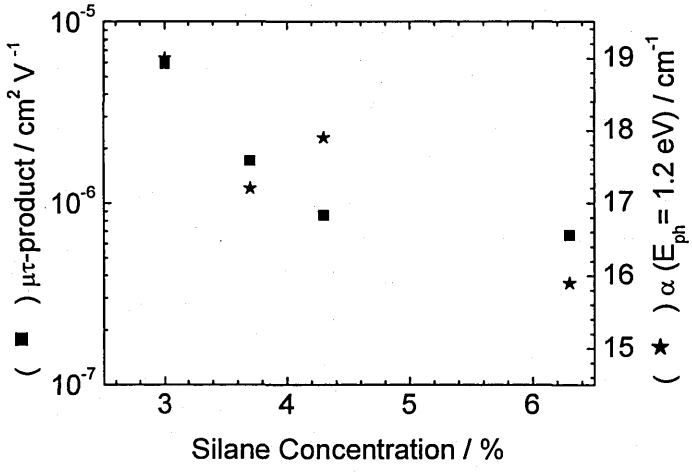

Figure 7.32 $\mu\tau$-product and alpha (1.2 eV) for different silane concentrations for the VHF PECVD μc-Si:H series.

Figure 7.33 shows the absorption coefficient spectra obtained by A-CPM. As seen most of the curves are very close together except the curve with the highest SC at 6.4%, which shows a higher α for E_{ph} between 2.5 eV to 1.9 eV. Also visible is a decreasing α for E_{ph} < 1 eV with increasing SC. For E_{ph} < 1.8 eV the absorption curves are close to the crystalline silicon curve (dotted line) which indicates a high crystalline fraction of the material while for E_{ph} < 1 eV, the contribution of the amorphous phase becomes noticeable, where the curves are showing similarities to a defect tail. The highest amorphous contribution is expected to be present in the sample OOC345 with 6.4% silane concentration.

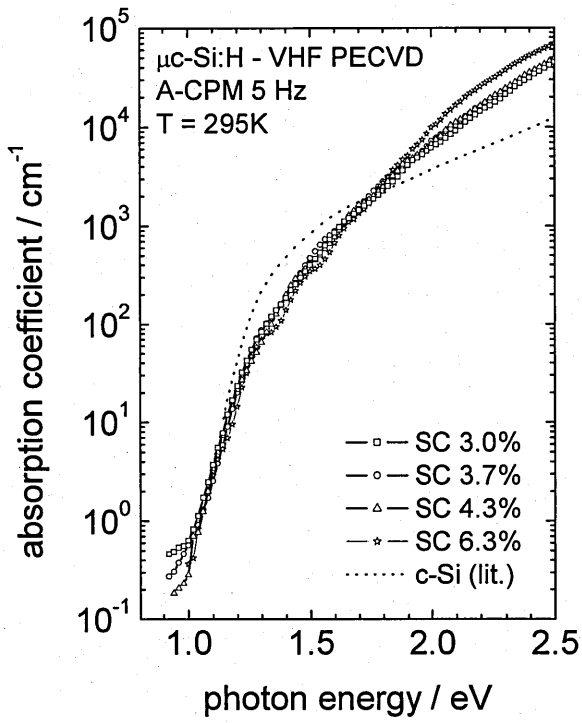

Figure 7.33 Absorption spectra for the VHF PECVD μc-Si:H films with different SC compared with the absorption curve for crystalline silicon (c-Si).

In table 7.7 experimental results for photoconductivity, dark conductivity, absorption coefficient at E_{ph} = 1.2 eV, and $\mu\tau$-products are presented for the HWCVD samples, listed in table 7.5. Here the values for the silane concentration are very widely spread, from 2% up to 90%, so it is expected to see absorption coefficient spectra showing a range of behaviour between highly microcrystalline and amorphous.

Table 7.5 Experimental results for the HWCVD series.

sample	silane concentration [%]	thickness [nm]	alpha (1.2 eV) [cm^{-1}]	photo conductivity [S cm^{-1}]	dark conductivity [S cm^{-1}]	μτ - product [$cm^2 V^{-1}$]
HW220	2	0.7	121.4	6.43E-10	1.07E-07	1.23E-08
HW219	10	0.7	176.1	2.72E-08	9.80E-07	3.57E-07
HW224	40	0.85	2.5	2.12E-08	2.37E-10	2.21E-07
HW223	75	2	43.6	7.34E-11	2.88E-11	1.81E-09
HW222	90	3	70.4	2.05E-10	1.31E-10	7.80E-09

The samples with 2% and 10% SC, which are microcrystalline (see figure 7.36), show a dark conductivity three orders of magnitude higher than the samples with 40%, 75% and 90% SC, which are more of amorphous type (figure 7.36). Brüggemann et al reported that μc-Si:H material has a significantly higher dark conductivity than a-Si:H material but the photoconductivity and $\mu\tau$-products are comparable to good quality a-Si:H material (Brüggemann et al, 1999). In the present work, the photoconductivity and $\mu\tau$-products for the samples with 2% and 10% SC indicate that they are of low quality compared with the microcrystalline samples from the VHF PECVD deposition (table 7.6). The sample with 40% SC shows a dark conductivity, photoconductivity and a $\mu\tau$-product comparable to an 'average quality' a-Si:H material, while the results for the samples with 75% and 90% SC indicate a poorer optoelectronic performance than typical a-Si:H material. Figure 7.34 shows the results for the dependency of the $\mu\tau$-products and α(1.2 eV) on the SC. As expected the α(1.2 eV) values for the microcrystalline samples with 2% and 10% SC are higher than for the amorphous samples with 40%, 75% and 90% SC but is not possible to classify the samples in microcrystalline or amorphous type from the $\mu\tau$-product data only (in contrast to the clear trends shown in fig 7.32), because of the overall low optoelectronic performance of these samples.

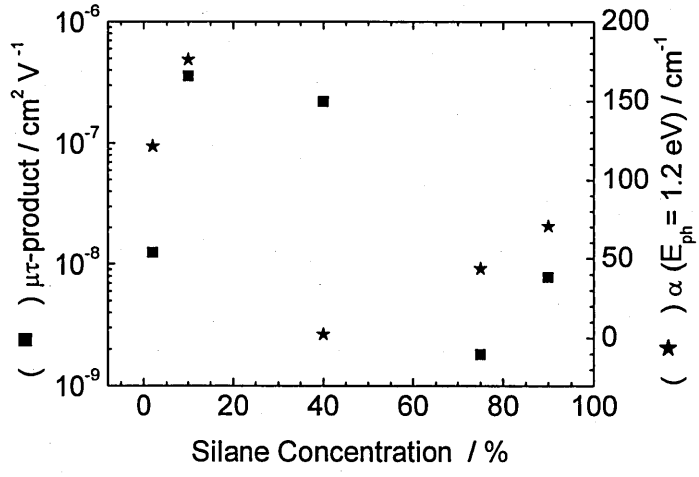

Figure 7.34 $\mu\tau$-product and alpha (1.2 eV) for different silane concentrations for the HWCVD series.

Experimental results from FTIR measurements, presented in figure 7.35, show at 2100 cm^{-1} the characteristic Si-H stretching doublet for the sample with the lowest SC at

2% which turns into the stretching mode at 2000 cm^{-1} with increasing SC, an indicator for high amorphous contribution, and the peak at 630 cm^{-1}, the 'wagging' mode, shifts to 640 cm^{-1} for the sample with 90% SC as reported by Klein et al.

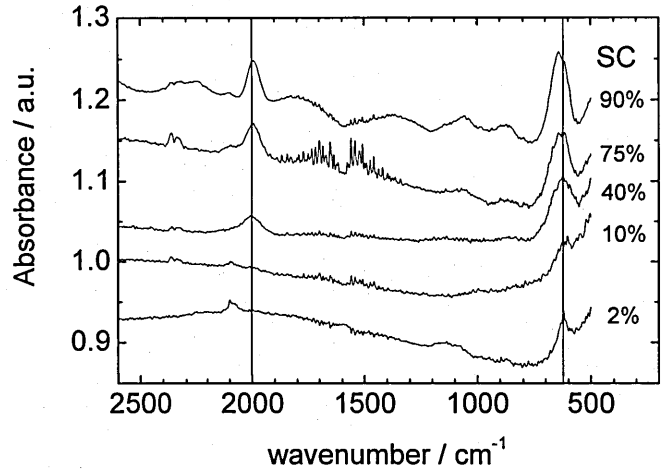

Figure 7.35 FTIR spectra (in arab. units) for the HWCVD produced films with changing silane concentration.

The peak at 1000 cm^{-1} to 1200 cm^{-1} for the sample with 2% SC indicates a Si-O contribution, which is used as an indicator for the porosity of material and is especially strong in μc-Si:H material, but this peak also shows up for the samples with 75% and 90% SC which indicates a low quality amorphous material with high oxygen contamination.

Figure 7.36 presents the absorption coefficient spectra, obtained by A-CPM, for the HWCVD series. It is clearly seen that the samples with 2% and 10% SC are of microcrystalline structure and the samples with 40%, 75% and 90% are of amorphous structure by comparing the curves with the c-Si reference data (dotted line). It is also noticeable that the amorphous samples with 75% and 90% SC are of low quality because they show a high defect part in the α-region for E_{ph} < 1.5 eV as predicted by the photoconductivity results and $\mu\tau$-results presented in table 7.7 and figure 7.34. This might be due to oxygen contamination as shown in the FTIR spectra from figure 7.35. The sample with 40% SC shows an average quality for an amorphous material. The microcrystalline samples show a very high contribution from the amorphous phase at E_{ph} < 1.2 eV compared with the VHF PECVD produced samples and according to their optoelectronic performance are of poor quality.

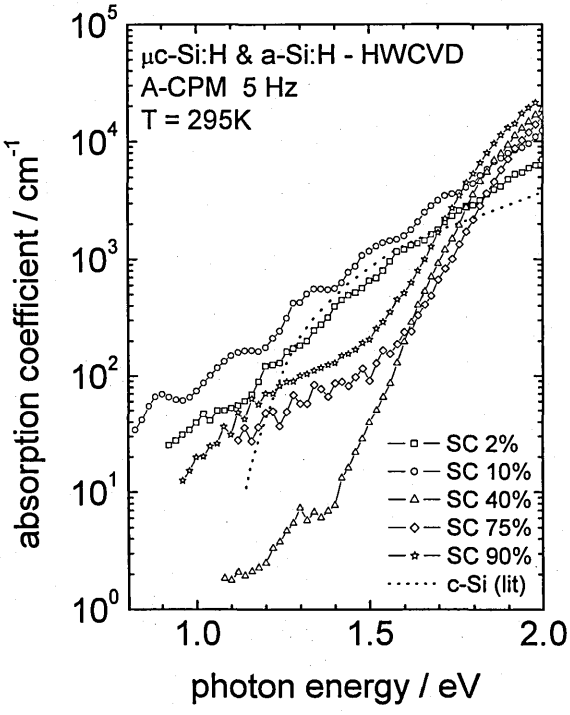

Figure 7.36 Absorption spectra for the HWCVD produced amorphous & µc-Si:H films with different SC compared with the absorption curve for crystalline silicon (c-Si).

7.8 Proton irradiation studies on amorphous and microcrystalline silicon

7.8.1 Introduction

Silicon-based photovoltaic devices used in an extraterrestrial environment, like the solar cell panels from a satellite orbiting the earth, are exposed to high energy radiation, which arises from the 'Van-Allen-Belt' providing protons with energies up to a few hundred MeV and electrons with energies up to a few MeV, and solar flares which is mainly due to proton radiation. Back on the earth's surface semiconductor detectors used in the field of high energy physics are also subject to high-energy proton and other particle radiation. The creation of defects by particle radiation and hence the increase of the defect density allows a fundamental study of the semiconductor electronic transport properties.

It has been reported that due to exposure of crystalline silicon solar cells to proton irradiation with energies smaller than 10 MeV changes were observed in the basic solar cell parameters (Yamaguchi et al, 1996, Morita et al, 1997). Kishimoto et al studied the properties of undoped, n-type and p-type c-Si material upon 17 MeV proton irradiation (Kishimoto et al, 1998). These authors also report a higher irradiation resistance from amorphous silicon in comparison with lowly doped crystalline silicon for the dark and photoconductivity. Proton fluences in the 10^{12} cm^{-1} range were sufficient to change the dark conductivity of lowly doped p-type c-Si by a few orders of magnitude (Kishimoto et al, 1998). Simeon et al., reported that n-type c-Si is more affected by 10 MeV proton irradiation than p-type c-Si (Simeon et al, 1996). As a result the damage coefficient for displacement damage of proton irradiation in silicon decreases with increasing proton energies. The maximum reduction in solar cell parameters for c-Si is in the 1 – 10 MeV proton energy range.

Brüggemann et al reported an increase in the sub-gap absorption and deteriorated photoelectronic properties of microcrystalline silicon by using electron irradiation with 1 MeV electrons (Brüggemann et al, 2001).

In this study proton irradiation with 100 MeV protons was applied to undoped amorphous and microcrystalline thin films produced by PECVD and HWCVD deposition technique and these films were investigated by using absolute CPM method.

7.8.2 Sample preparation and experimental methods

The samples used in this analysis were kindly provided by the 'Institut für Physikalische Elektronik, Stuttgart'. The sample EL26045 (μc-Si:H) was deposited by the UHV-HWCVD method and the samples L011132 (a-Si:H), L270714 (μc-Si:H) were deposited by the VHF-UHV-PECVD method. Proton irradiation with 100 MeV protons was performed at room temperature at Centre de Protonthérapie d'Orsay. The flux was about $4x10^{11}$ cm^{-2} s^{-1} and the duration of the irradiation was about 2.5 h, so that the total proton fluence was 10^{12} cm^{-2}. Absorption coefficient measurements were performed by using the absolute CPM method before and after proton irradiation. $\mu\tau$-products and photoconductivity data were obtained at $\Phi = 10^{14}$ cm^{-2} s^{-1} at $E_{ph} = 1.96$ eV.

7.8.3 Experimental results

Table 7.6 shows the results obtained for dark and photoconductivity and for $\mu\tau$-products before and after proton irradiation.

Table 7.6 Experimental results for optoelectronic properties before and after proton irradiation.

sample	proton irradiation 100 MeV	thickness [nm]	alpha (1.2 eV) [cm^{-1}]	photo conductivity [S cm^{-1}]	dark conductivity [S cm^{-1}]	$\mu\tau$ - product [$cm^2 V^{-1}$]
EL26045	no	504	113.6	9.45E-08	4.12E-05	1.54E-06
EL26045	yes	504	120.2	1.23E-07	3.90E-06	2.00E-06
L011132	no	914	0.37	3.08E-08	5.36E-11	3.48E-07
L011132	yes	914	0.47	5.21E-08	3.48E-10	5.88E-07
L270714	no	484	46.8	2.27E-07	5.50E-07	4.01E-06
L270714	yes	484	65.6	2.71E-07	7.45E-07	4.86E-06

As table 7.6 shows, no significant changes were observed before and after proton irradiation. The same results can be obtained for the absorption coefficient spectra obtained by A-CPM as shown in figure 7.37, 7.38, and 7.39. The absorption remains unchanged for both microcrystalline and amorphous samples after proton irradiation.

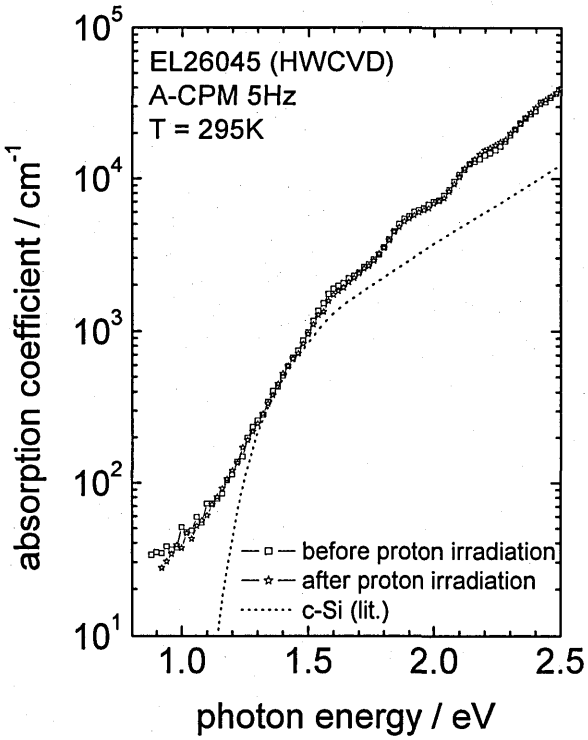

Figure 7.37 Absorption coefficient before and after proton irradiation for μc-Si:H film.

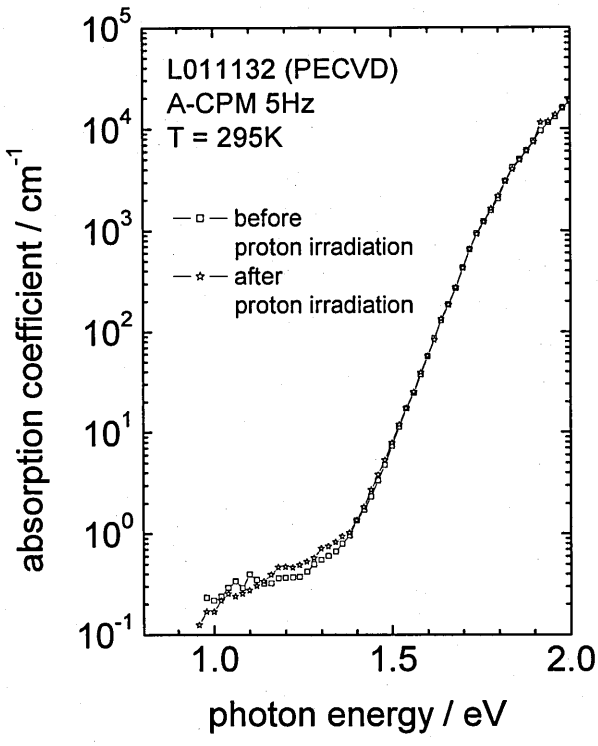

Figure 7.38 Absorption coefficient before and after proton irradiation for a-Si:H film.

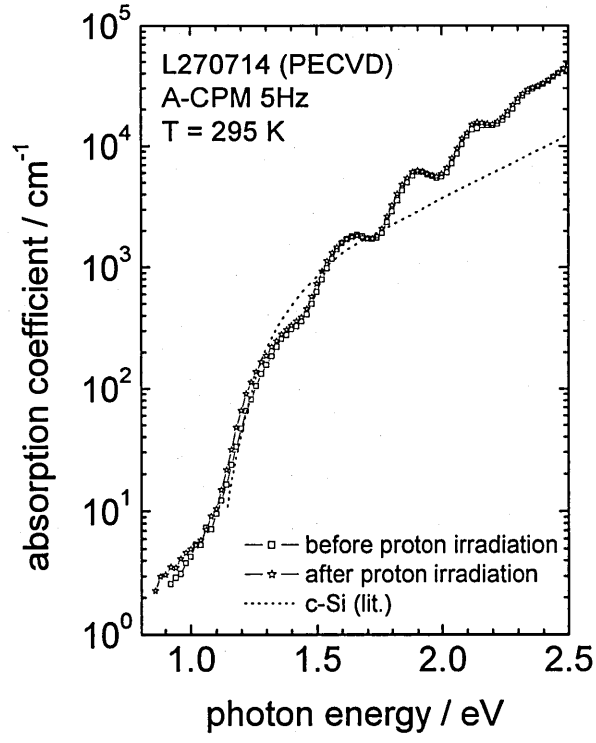

Figure 7.39 Absorption coefficient before and after proton irradiation for μc-Si:H film.

7.9 CPM measurements on non-Silicon materials

7.9.1 Introduction

In this study the CPM method was applied to photoconductive materials which are not based on silicon. This study should be considered as a demonstration only to show the applicability of the CPM method to non-silicon materials. CPM measurements were performed on Cadmium-Telluride (CdTe), Gallium-Arsenide (GaAs), and multilayer Cadmium-Selenide (CdSe) and Germanium-Sulfide (GeS_2) samples. It is worth noting that when the CPM method was first introduced by Grimeis and Lebedo in 1975, it was used to determine the density of states in GaAs material. Hence, the CPM method is not bound to silicon material only; any *photoconductive* material can be investigated by using this measurement method.

7.9.2 Photocurrent defect spectroscopy in CdTe:Sn

There is considerable interest in the study of CdTe for optoelectronic applications. For this semiconductor, doping with tin (Sn) allows a controlled variation of the dark conductivity between about 1 and 10^{-10} S cm^{-1} (Panchuk et al, 1999). It is important to understand the physics of defects in the band gap which are introduced by the doping. Defect spectroscopy for the vanadium counterpart CdTe:V is reported for quite a number of different methods, for example: Zielinger et al, 1993, Lambert et al, 1995, Longeaud et al, 1995. For the so far less popular CdTe:Sn the investigations are not so numerous (Shcherbin et al, 2001).

The sample under study here is a crystalline CdTe:Sn specimen with a thickness of 1.55 mm. The contacts were made from silver paint, 5 mm wide and 1 mm apart. The dark conductivity is 6.25×10^{-11} S cm^{-1} at room temperature. Panchuk et al have shown that the conductivity of CdTe:Sn is n-type and its type does not change under illumination (Panchuk et al, 1999).

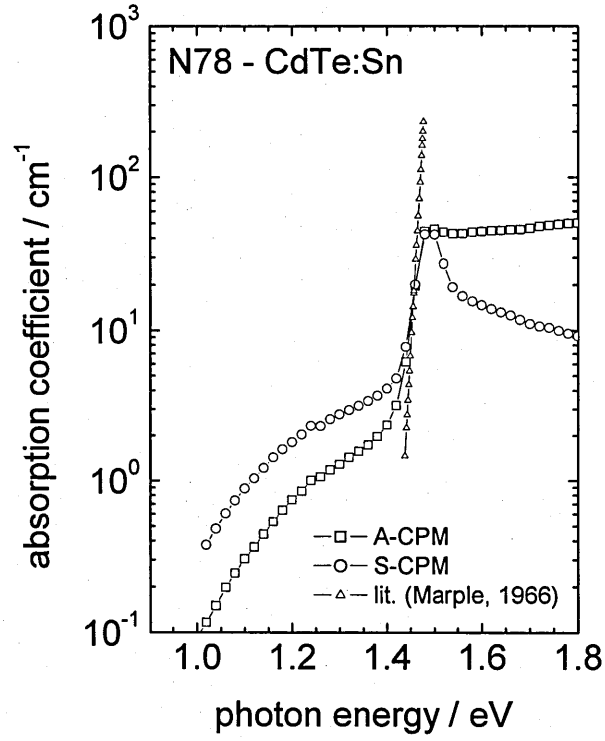

Figure 7.40 Absolute and standard CPM spectrum for CdTe:Sn. For comparison the absorption coefficient of undoped CdTe is shown (Marple, 1966).

Figure 7.40 shows the measured CPM spectrum which covers photon energies larger and smaller than the band gap of 1.55 eV. In comparison with published absorption-coefficient data on undoped CdTe by Marple (Marple 1966), there is an increase in sub-gap absorption. The absorption edge around the band gap is not modified by doping and in this region the CPM data were calibrated using the absolute CPM method. The values for the refractive index in the Ritter-Weiser-Equation (Equation 2.35), used to calculate the absolute values for the absorption coefficient, were altered to match the typical values for CdTe material. The S-CPM spectrum shows a gap defect level at 1.49 eV which nearly disappears in the A-CPM spectrum. The defect level identified here is not the only defect in the band gap. Jantsch and Hendorfer (Jantsch and Hendorfer, 1990) determined a mid-gap defect by electron-spin resonance techniques and a g-value of 2.012. By Fourier-transformed transient photoconductivity additional defect levels can be identified in the upper half of the band gap. Which of these levels is the one measured by Jantsch and Hendorfer needs further investigation. These measurement results show that in contrast to a number of levels in the upper half of the band gap there appears to be only one below.

For photon energies $E_{ph} < 1.45$ eV the A-CPM spectrum shows, by a factor of 3, a lower α than the S-CPM spectrum, which may be due to the greater thickness of the sample which causes a non-uniform generation profile. For photon energies $E_{ph} > 1.55$ eV both CPM spectra are influenced by surface recombination and hence are not valid anymore because of $\alpha d > 1$.

7.9.3 Photocurrent spectroscopy on GaAs

Gallium-Arsenide is a chemical compound composed of Gallium (Ga) and Arsenide (As) with a crystalline configuration known as cubic sphalerite or zinc blende. It is widely used in the semiconductor industry for making devices such as microwave frequency integrated circuits, laser diodes, infrared emitting LED's and solar cell applications. Due to its higher electron mobility (8500 $cm^2 V^{-1} s^{-1}$) than crystalline silicon (1350 $cm^2 V^{-1} s^{-1}$) it is a potential candidate for high-power applications. GaAs is a direct band gap semiconductor with a band gap $E_g = 1.42$ eV, which makes this material very useful for the manufacture of light emitting diodes and semiconductor lasers. GaAs can be doped with Si to give either p-type GaAs by incorporating it at low temperatures, or n-type GaAs by processing it at high temperatures. Another group IV element, carbon, is also used extensively to provide p-type GaAs. Chromium (Cr) behaves as an acceptor, with an impurity level close to the center of the energy gap. This provides a substrate that isolates components and performs many of the same tasks, albeit not as effectively, as silicon dioxide. Other elements such as copper, oxygen, selenium, and tin are also used in GaAs processing to provide the desired n- or p-like behaviour (Blakemore 1982).

The GaAs samples were kindly provided by the 'Ruđer Bošković Institute' Division of Materials Physics, Zagreb. One sample is undoped and the other sample was doped with Cr. Because of the silicon substrate CPM measurements were only performed in standard mode at a chopper frequency of 5 Hz. Figure 7.41 shows the CPM results for both GaAs samples.

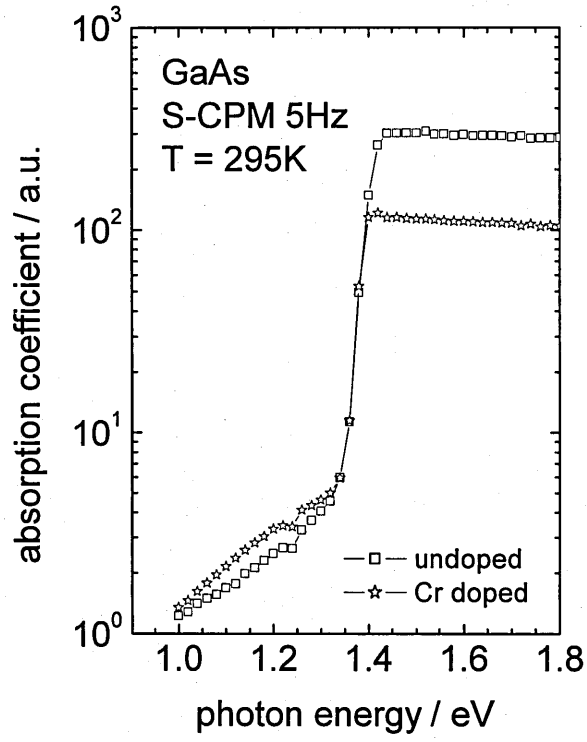

Figure 7.41 S-CPM spectra for undoped and Cr doped GaAs on Si samples.

Figure 7.41 shows for both sample the band edge at about 1.4 eV where a rapid decrease of the absorption coefficient is detectable. Both spectra overlap at the steep band edge section in the absorption spectrum and for photon energies E_{ph} < 1.35 eV the Cr doped GaAs sample shows a higher absorption than the undoped GaAs sample. For photon energies E_{ph} > 1.4 eV both CPM curves are in saturation because of mainly surface absorption and hence the data are invalid. The photoconductivity, measured at E_{ph} = 1.96 eV and a total flux of 10^{14} cm^{-2} s^{-1}, for the undoped sample is 2 x 10^{-6} S cm^{-1} and for the Cr doped sample 3 x 10^{-7} S cm^{-1}, in accordance with the accepted application of Cr to produce semi-insulating GaAs.

7.9.4 Defect spectroscopy of CdSe nanocrystals in GeS_2-CdSe superlattices

The major reasons for research on nanocrystals (NCs) lie in the effect of electron and hole quantized states in different confinement regimes, confined phonon modes, the process of electron-phonon interactions etc., which can lead to device applications benefiting from size controlled spectral tunability, confinement induced concentration of the oscillator strength and ultra fast relaxation dynamics.

In this study GeS_2-CdSe superlattices and composite films were investigated by using the CPM measurement method. The films were kindly provided by the Institute of Solid State Physics, Bulgarian Academy of Sciences, 1784 Sofia, Bulgaria. The films were prepared by consecutive thermal evaporation of CdSe and GeS_2 in vacuum. The CdSe layer thickness varies between 1 and 10 nm, while the thickness of GeS_2 layers is either equal (in superlattices) to or 20 times greater (in composite films) than that of CdSe layers. The two films used in this analysis had a CdSe layer thickness of 2.5 nm (G144) and 5 nm (G24), and a GeS_2 layer thickness of 3nm (G144) and 100 nm (G24) resulting in a total thickness of 165 nm for the G144 sample and 1780 nm for the G24 sample. For more details information about the deposition process and sample preparation data see Nesheva et al, 2004.

The A-CPM measurements were carried out at room temperature and a chopping frequency of 5 Hz. The electric field applied to both samples was $E = 500$ V cm^{-1}.

The usage of the CPM method on two-component films is more complicated than on an individual film. Both components of these samples are photoconductors and one had to estimate the contribution of each kind of layer to the total photocurrent. From photoconductivity measurements on individual GeS_2 and CdSe films it is known that the photoconductivity of GeS_2 under 50 mW white light exposure is more than 100 times lower than that of CdSe. The other feature is that the band gap of GeS_2 is 2.5 eV and that of CdSe is 1.75 eV, which should be noticeable in the CPM spectrum (Nesheva et al, 2004).

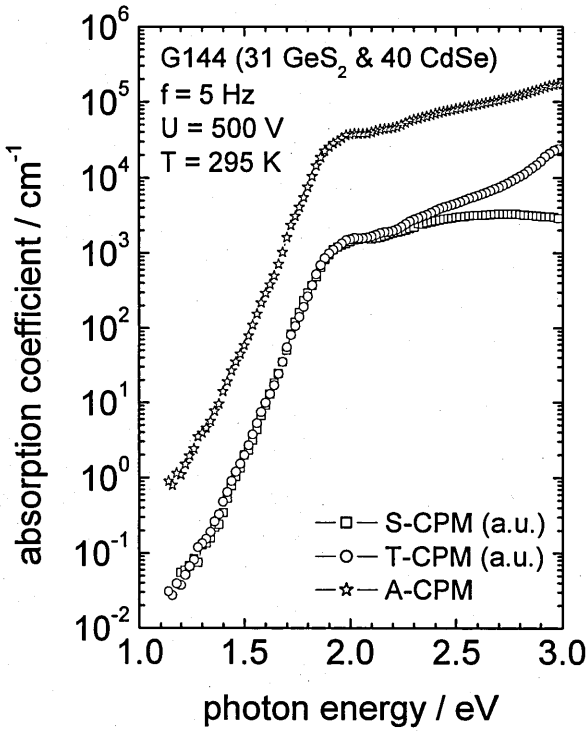

Figure 7.42 Standard, transmission and absolute CPM measurements results for the G144 GeS_2 & CdSe nanocrystalline sample with total thickness of 165 nm.

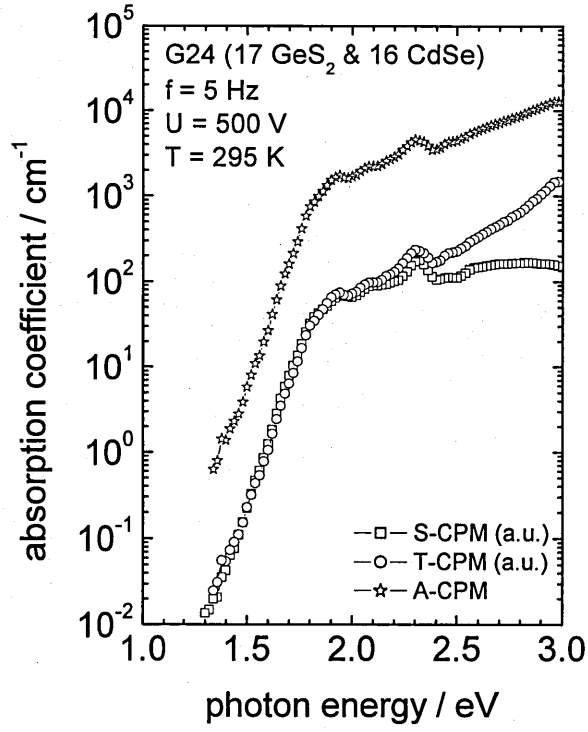

Figure 7.43 Standard, transmission and absolute CPM measurements results for the G24 GeS_2 & CdSe nanocrystalline sample with total thickness of 1780 nm.

Figure 7.42 shows the absorption spectra for the G144 sample with the '2.5 nm' single layer thickness for CdSe. Because of the total thickness of 165 nm the curves do not show any significant features except the for the very weak interference maximum at 1.9 – 2.0 eV. At E_{ph} = 2.3 eV the standard- and the transmission- CPM curves split apart which is due to the CPM limitations ($\alpha d \geq 1$). At E_{ph} = 1.8 eV towards lower photon energies the absorption coefficient rapidly decreases because of the band gap of CdSe. From the CPM spectra no indication of the band gap of GeS_2 is detectable.

Figure 7.43 shows the absorption spectra for the G24 sample with the '5 nm' single layer thickness for CdSe. The thickness of 1780 nm causes the standard and transmission CPM spectra to enter saturation at E_{ph} = 2.1 eV towards higher photon energies, while the position of the features is the same for all spectra. Three significant maxima can be observed from figure 7.43 at E_{ph} = 1.94 eV, E_{ph} = 2.09 eV, and E_{ph} = 2.3 eV, which were associated with the electron transition $1S_{3/2}$-$1S_e$ at 1.94 eV, $1S_{1/2}$-$1S_e$ at 2.09 eV, and $2S_{1/2}$-$1S_e$ at 2.3 eV in CdSe quantum dots (Norris and Bawendi, 1996).

Because of the lack of absorption coefficient data from other sources like transmittance measurements, the validity of the absolute CPM method for both samples could not be verified.

7.10 Summary

The CPM measurement on a c-Si sample in chapter 7, section 7.2, has shown that the resolution of the absolute CPM setup used in this work is sufficient for most measurements on a-Si:H material. It is also valid to use multiple CPM photocurrents during a CPM measurement to obtain the absorption coefficient spectrum over the whole photon energy range of interest, as shown in section 7.3.

The first attempted experimental production of an HWCVD film (HW105) in section 7.4 has resulted in a moderately n-type sample due to some contamination. The source of contamination is at this stage still unknown but it has been shown that the quality of the PECVD film (B1421) produced in the same laboratory system as the HWCVD film previously, is comparable to PECVD films produced in a commercial reactor. The second test sample produced by the HWCVD deposition technique, HW159, shows electronic properties and DOS profile very similar to the commercially produced PECVD films. It is

also more resistant against light-soaking than the PECVD films. As a conclusion it was shown that the HWCVD deposition method is indeed able to produce high quality amorphous silicon material at much higher deposition rates, as seen in table 7.1.

The depth profiling study in section 7.5 has shown that high concentrations of carbon and oxygen impurities are responsible for low film qualities, and which might have also been responsible for the low quality of the 'n-type' sample (HW105) presented in section 7.4. It has been shown that the oxygen and carbon contamination decreases throughout the deposition, but as more evaporated silicon is incorporated, the electronic structure changes. If initially, on the film surface, the growth process involves diffused thermally dissociated radicals, then later in the deposition there is a contribution from evaporated species after the formation of a thick silicide on the heated tungsten wire. As a result, the quality of the films produced is a varying function of the elapsed filament operating time, and aged filaments are predicted to produce poorer quality films. Therefore control of the filament conditions is likely to be a major implementation of the HWCVD process.

In section 7.6 the connection between the 'filament to substrate' distance and the quality of HWCVD deposited films has been examined by CPM and as a result the best film properties were shown to be obtained at the film position d = 54.2 mm from the hot-wire. Further away from the hot-wire the film thickness falls off as $cos^3\beta$ towards the film edge while the photoconductivity and $\mu\tau$-product results show influences from contamination. Closer to the hot-wire the film thickness increases rapidly as the film becomes very stressed due to the heat radiation from the hot-wire as seen in the absorption spectrum. Aim of this study was to show a way of producing films with a homogenous thickness and equally distributed optoelectronic film properties i.e by using an array of hot-wires.

In section 7.7 it was shown that the silane concentration in the deposition process is an important parameter in producing either amorphous or microcrystalline material. It has been shown that by increasing the silane concentration, the material turns out to be more amorphous or even fully amorphous after deposition. From the literature it has been shown that by increasing the silane content over 20% the resulting material deposited is amorphous. The microcrystalline sample series produced by the VHF PECVD method turn out to be of high quality while the HWCVD method employed was able to produce microcrystalline material but only of low quality. The amorphous samples produced by this method are of low quality too, because of possible contamination as revealed from FTIR measurements. The literature has shown that it is indeed possible to produce high quality

microcrystalline material by using HWCVD which is comparable to PECVD – produced material, but the present laboratory system used still needs lots of fine-tuning.

Section 7.8 has shown for both μc-Si:H and a-Si:H samples only negligible changes in the optoelectronic properties upon proton irradiation with 100MeV protons and a fluence of 10^{12} cm^{-2}. Also no significant changes were found in the CPM spectra irrespective of the deposition method. As already reported in the literature these results confirm the resistance to proton irradiation of a-Si:H material as well as the μc-Si:H material.

Section 7.9 has shown that the absolute CPM method is applicable to non-silicon material, too. CPM results for the crystalline CdTe:Sn sample show that the standard CPM method was able to detect a defect level in the band gap of CdTe:Sn material where the absolute CPM method only shows a very small peak. The absorption coefficient obtained with absolute CPM method is in good agreement with the data from Marple (Marple 1966). CPM measurements on GaAs samples could only be performed in standard mode because of the silicon substrate. The standard CPM spectrum shows for both samples a rapid decrease in the absorption coefficient at about 1.4 eV which is the band edge for this material. For $E_{ph} < 1.4$ eV the Cr doped GaAs sample shows a higher absorption than the undoped GaAs sample which is in accordance with the literature (Blakemore 1982), where again, Cr doping is used to produce semi-insulating GaAs. Absolute CPM measurement results on CdSe nanocrystals in GeS_2-CdSe superlattices (multi-layer) show for the G144 sample a rapidly decreasing $\alpha(E_{ph})$ for $E_{ph} < 1.8$ eV which indicates the band edge of CdSe, but no indication of the GeS_2 band edge is noticeable. The absolute CPM spectrum for the G24 sample, where the material concentration of GeS_2 is much higher than CdSe, shows three significant maxima at $E_{ph} = 1.94$ eV, $E_{ph} = 2.09$ eV, and $E_{ph} = 2.3$ eV and a rapid decrease of $\alpha(E_{ph})$ for $E_{ph} < 1.8$ eV, which again indicates the band edge of CdSe. The validity of the absolute CPM spectra could not be verified because of the lack of $\alpha(E_{ph})$ data from other measurement methods.

Chapter 8 - Summary and conclusions

Amorphous silicon films produced by the HWCVD method are reported in the literature to be more resistant against degradation during light soaking, have a better electronic performance, and can be produced at far higher deposition rates with electronic performance comparable to films produced by the PECVD method. In chapter 7, section 7.4, HWCVD samples produced in a laboratory reactor at the University of Dundee, were compared with PECVD samples from a commercial production line at Intersolar UK, which have been regarded as a 'reference'. As a result it can be reported that the nominally undoped samples produced by the HWCVD method are at least comparable to their PECVD counterpart, with similar photoconductivity and $\mu\tau$-product, Fermi energy level, absorption coefficient and density of states. A slightly better resistance against light soaking could be determined too (at least for the HW159 sample) which increases with the number of annealing and light soaking cycles as was shown in figure 7.22. Also it can be confirmed that it is indeed possible to produce a high quality film by HWCVD at much higher deposition rates than with PECVD when comparing the deposition times and thickness of the HW159 (HWCVD) and the B1421 (PECVD) samples. Unfortunately, the deposition times for the Intersolar samples were unknown but the author assumes that they are similar to the B1421 (PECVD) sample produced in a laboratory setup.

A significant problem with the HWCVD material was contamination of carbon and oxygen during the HWCVD deposition process which resulted in slightly n-type material with a significant lower optoelectronic performance as reported in chapter 7, section 7.4, 7.5 and 7.7. The origin of the contamination is assumed to be the effect from aged filaments, especially if they are covered by a thick silicide on the heated tungsten wire as the depth profiling analysis in section 7.5 reveals and therefore control of the filament condition during the hot wire deposition process is a major requirement.

A major problem for the commercial application of the HWCVD method is the fact that films deposited using only a single tungsten wire as a filament result in a very inhomogeneous film thickness distribution, resulting from the filament – substrate geometry, as demonstrated in section 7.6. According to the CPM results shown in figure 7.31 the best film quality was achieved at a film position 54.2 mm, which corresponds to a direct 'filament to substrate' distance of 56.2 mm. The difficulty thus lies in designing an array of filaments, where each hot wire string has the optimum distance from its neighbour,

in which including overlapping deposition processes from every single hot wire, an overall distance between hot wire array and substrate of about 56 mm can be achieved, so as to produce a homogeneous film thickness over a large area (> 100 cm^2). From the literature distances between filament and substrate of 40 – 60 mm were reported, which also varies with the design of the reactor chamber.

In chapter 7, section 7.7 the effect of the silane content on the film properties was presented, where it was shown that by increasing the silane content (silane gas concentration in hydrogen) the resulting film shifts from the microcrystalline towards the amorphous phase. CPM and FTIR measurements were performed on PECVD and on HWCVD produced samples. Due to the low quality films associated with contamination problems in the laboratory HWCVD setup, a more reliable comparison between the microcrystalline samples from PECVD and HWCVD was not possible. Despite contamination influence the FTIR results shown in figure 7.35 still show the typical shifts in the peak from 2100 cm^{-1} to 2000 cm^{-1}, for the Si-H stretching mode, and from 630 cm^{-1} to 640 cm^{-1}, for the Si-H 'wagging' mode, with increasing silane content as reported in the literature. In accordance with the FTIR results, the CPM results showed for low silane content the typical microcrystalline optical absorption curve, which follows the shape of the c-Si spectrum and for high silane content the typical amorphous shape of the α curve, with a steep tail part and the defect shoulder.

In chapter 7, section 7.8 reported on amorphous and microcrystalline samples exposed to 100 MeV proton irradiation. The CPM results obtained before and after the irradiation process show no significant changes in the absorption and electronic performance in contrast to electron irradiation, where an increase in the sub-gap absorption could be observed as reported from literature. It is assumed that the amorphous network is able to rearrange itself after damage to the bonding structure caused by high energy particles like protons.

In chapter 7, section 7.9 demonstrates the CPM method on non-Si materials and shows that CPM measurement can be performed on any photoconductive, single or multi-layer material. The only limitation noted is the use of the Ritter-Weiser equation in the absolute CPM method, where the equation needs to be adjusted by the corresponding different refractive index R_2 of the material examined.

Study of the CPM measurement method itself became the main focus of this thesis, originating in the clear differences in the absorption coefficient as measured by DC and AC CPM, reported and presented in chapter 4, 5 and 6. In chapter 4 a model was presented which explains the differences between DC and AC CPM, whose origin is 'slow' phonon assisted free electron creation *via* unoccupied defects (i.e. optical transition into unoccupied defect followed by thermal release). This view is supported by an analysis of sub-gap AC photoconductivity which shows that CPM may be formally treated as super-gap MPC, but with the inclusion of distributed poles in the generation rate. A consequence of this is that the AC CPM measurement may actually allow a more accurate deconvolution to determine the defect DOS.

In chapter 5 DC and AC CPM measurements were performed on PECVD and HWCVD samples. The DC and AC discrepancy in the absorption coefficient spectra caused a difference of up to a factor 4 after deconvolution into the DOS spectra. The chopping - frequency-dependent CPM measurements were in good agreement with the model presented in chapter 4. At chopping frequencies higher than 27 Hz no significant difference in the CPM results was noted. Temperature dependent DC and AC CPM measurements showed a disappearance of the AC - DC discrepancy towards higher temperatures for the light-soaked PECVD sample where for the HWCVD sample the discrepancy remained. The MPC related measurements showed that if the AC photocurrent stays constant (with wavelength) during a DC CPM measurement, then no AC/DC discrepancy could be observed, because the transitions are mainly dominated by optical transitions (fast path, see chapter 6, figure 6.1 (b)).

In chapter 6 a method was presented which allows determination of the distribution of defects *below and above* the Fermi level from combined DC and AC CPM measurements. Simulation results showed that using the *difference* between DC and AC α spectra, reflected across the mid-gap, it is possible to reproduce the original distribution of *unoccupied* defects above the Fermi level. Experimental results which include the DOS above the Fermi level obtained from TPC measurement, for comparison, gave good agreement with the extended CPM – DOS model presented in chapter 6.

8.1 Directions for future work

A model was presented which explains the DC – AC CPM discrepancy observed in this work and by others, and identifies the AC mode CPM as a more accurate measure of the DOS below E_F, but much further work is required to include effects of defect occupancy, quasi Fermi level shifts and the influence of holes on the analysis. Further, the influence of temperature needs to be investigated experimentally in more detail, especially since the temperature dependence of the DC – AC CPM discrepancy towards low temperatures is of importance because no measurements were performed at low temperatures to test the model predictions as shown in chapter 6, figure 6.2. More TPC measurements are necessary, to be performed on samples showing the DC – AC discrepancy, to verify the obtained DOS from the (DC – AC) α difference as shown in chapter 6, figure 6.7. Also DC and AC CPM measurements should be performed on microcrystalline material and multilayer structures, which may give additional information to the density of states structure of these materials.

As for the CPM measurement method a new approach was introduced by Poruba et al using FTIR and CPM combined to obtain the absorption coefficient for photon energies even lower than 0.7 eV (Poruba et al, 2002). The new method is called 'Fourier Transform Infrared Photocurrent' spectroscopy – FTPS. A Fourier transform infrared (FTIR) spectrometer is used as the light source and interferometer and a photoconductive sample as the external detector. Typical measurement range is 0.4 – 1.9 eV which could be performed in a few minutes only (CPM → approx. 60 min.). The implications of the model developed in the present work for such a method need to be explored, as do the implications with respect to the existing PDS method.

The laboratory HWCVD setup presented in this thesis needs development to reduce or even eliminate future contamination influences, which significantly degraded the optoelectronic performance of the HWCVD samples examined. Also more research is necessary into the catalytic processes involved on the hot wire surface during deposition. Possible alternatives to the tungsten wire material (i.e. Tantalum, Molybdenum, Vanadium) may be investigated, too (Matsumura, 1998).

Masuda et al reported proposed using a "catalytic plate" instead of the conventional wire in order to suppress the heat radiation by keeping the catalyser area which resulted in a-Si:H films with lower dangling bond density (Masuda et al, 2000).

Latest research work in simulation of the Staebler-Wronski effect by Biswas and Pan revealed that hydrogen-diluted material grown at the edge of crystallinity – the phase boundary between microcrystalline and amorphous film growth, have a much greater stability to light-induced degradation than standard amorphous materials (Biswas and Pan, 2002, Biswas 2003) which might be the key for future *sunproof* solar cells.

References

Abe, K. Okamoto, H. Nitta, Y. Tsutsumi, Y. Hattori, K. Hamakawa, Y. 1988. *Philosophical Magazine B*, **58:** 171.

Abe, K. Tsushima, T. Ichikawa, M. Yamada, A. Konagai, M. 2000. *Journal of Non-Crystalline Solids,* **266-269:** 105.

Anderson, P.W. 1958. *Physical Review*, **109:** 1492.

Biswas, R. and Pan, B.C. 2002. *Journal of Non-Crystalline Solids*, **299-302:** 507.

Biswas R. 2003. *AMES LABORATORY's website* [online]. [Accessed 31st May 2005]. Available from World Wide Web: < http://www.external.ameslab.gov/Final/News/2003rel/solar.html>.

Blakemore, J. 1982. *Journal of Applied Physics*, **53:** 520.

Brodsky, M.H. Cardona, M. and Cuomo, J.J. 1977. *Physical Review B*, **16:** 3556.

Brüggemann, R. Hierzenberger, A. Reinig, P. Rojahn, M. Schubert, M.B. Schweizer, S. Wanka, H.N. Zrinščak, I. 1998. *Journal of Non-Crystalline Solids*, **266-269:** 258.

Brüggemann, R. 1998 in *Properties of Amorphous Silicon and its Alloys - Vol 19*, edited by Tim Searle, London, U.K., INSPEC, IEE, 217.

Brüggemann, R. Bronner, W. Hierzenberger, A. Schubert, M.B. and Zrinščak, I. 1999. *Thin Film Materials and Devices – Developments in Science and Technology*, edited by J.M. Marshall et al., Singapore, 1999, World Scientific, p.1.

Brüggemann, R. Kleider, J.P. Longeaud, C. Mencaraglia, D. Guillet, J. Bourée, J.E. Niikura, C. 2000. *Journal of Non-Crystalline Solids*, **266-269:** 258.

Brüggemann, R. Bronner, W. Mehring, M. 2001. *Solid State Communications*, **119:** 23.

Bube, R.H. Benatar, L.E. Grimbergen, M.N. and Redfield, D. 1992. *Journal of Applied Physics*, **72:** 5766.

Chittick, R.C. Alexander, J.H. and Sterling, H.F. 1969. *Journal of the Electrochemical Society*, **116:** 77-81.

Conte, G. Irrera, F. Nobile, G. Palma, F. 1993. *Journal of Non-Crystalline Solids*, **164-166:** 419.

Dalal,V. L. 2001. *Thin Solid Films*, **395:** 173.

Feifar, A. Poruba, A. Vaněček, M. Kočka, J. 1996. *Journal of Non-Crystalline Solids*, **198-200:** 304.

Finger, F. Vetterl, O. Carius, R. Lambertz, A. Scholten, C. Houben, L. Luysberg, M. 2001 in *Materials for information technology in the new millenium*, edited by J.M. Marshall et al, Bath, 2001, p26.

Fritzsche, H. 1977. *Proceedings of the 7th International Conference on Amorphous and Liquid Semiconductors,* edited by W.E. Spear. Edinburgh: CLCI, 3.

Gallagher, A. 2001. *Thin Solid Films*, **395:** 25.

Grimmeis, H.G. and Lebedo, L. A. 1975. *Journal of Applied Physics*, **46:** 2155.

Guillet, J. Niikura, C. Bourée, J.E. Kleider, J.P. Longeaud, C. Brüggemann, R. 2000. *Materials Science and Engineering*, **69-70:** 284.

Hasegawa, S. Nitta, S. Nonomura, S. 1996. *Journal of Non-Crystalline Solids*, **198-200:** 544.

Hata, N. and Wagner, S. 1991 in *Amorphous Silicon Technology - 1991, Proceedings of MRS Symposium A, Vol. 219,* edited by A. Madan, Y. Hamakawa, M. Thompson, P. C. Taylor, and P. G. LeComber, (MRS, Pittsburgh, 1991), p611.

Heintze, M. Zedlitz, R. Wanka, H.N. Schubert, M.B. 1996. *Journal of Applied Physics*, **79:** 2699.

Hishikawa, Y. Nakamura, N. Tsuda, S. Nakano, S. Kishi, Y. and Kuwano, Y. 1991. *Japanese Journal of Applied Physics*, **30**(5)**:** 1008.

Holt, J.K. Swiatek, M. Goddwin, D.G. Müller, R.P. Goddard III, W.A. Atwater, H.A. 2001. *Thin Solid Films*, **395:** 29.

Hulthén, R. 1975. *Physika Scripta*, **12:** 342.

Iiduka, R. Heya, A. Matsumura, H. 1997. *Solar Energy Materials and Solar Cells*, **48:** 279.

Itoh, M. Ishibashi, Y. Masuda, A. Matsumura, H. 2001. *Thin Solid Films*, **395:** 138.

Jackson, W.B. Amer, N.M. Boccara, A.C. Fournier, D. 1981. *Applied Optics*, **20:** 1333.

Jantsch, W. and hendorfer, G. 1990. *Journal of Crystal Growth*, **101:** 404.

Jensen, P. 1990. *Solid State Communications*, **76:** 1301.

Karatyan, S.L. Chatilyan, G.A. Voskerchan, Z.A. Manasaryan, Z.A. 1997. *Chemical Physics Reports*, **16:** 1217.

Kishimoto, N. Amekura, H. Kono, K. Lee, C.G. 1998. *Journal of Nuclear Materials*, **258-263:** 1908.

Klein, S. Finger, F. Carius, R. Wagner, H. Stutzmann, M. 2001. *Thin Solid Films*, **395:** 305.

Kočka, J. Vaněček, M Schauer, F. 1987. *Journal of Non-Crystalline Solids*, **97-98:** 715.

Kołodziej, A. 2004. *Opto-Electronics Review*, **12:** 21.

LeComber, P.G. and Spear, W.E. 1970. *Physical Review Letters*, **25:** 509.

LeComber, P.G. Spear, W.E. Allan, D. 1979. *Journal of Non-Crystalline Solids*, **32:** 1.

Ley, L. 1998 in *Properties of Amorphous Silicon and its Alloys - Vol **19***, edited by Tim Searle, London, U.K., INSPEC, IEE, 113.

Liu, H.N. and Xu, M.D. 1986. *Solid State Comminication*, **58** (9): 601.

Longeaud, C. Kleider, J.P. and Cuniot, C. 1995. *Optical Materials*, **4:** 271.

Mahan, A.H. Carapella, J. Nelson, B.P. Crandall, R.S. 1991. *Journal of Applied Physics*, **69:** 6728.

Main, C. Berkin, J. Russell, R. Merazga, A. Marshall, J. M. 1987. *Journal of Non-Crystalline Solids*, **97-98** (part 2)**:** 779.

Main, C. Merazga, A. Kirstensen, I.K. and Berkin, J. 1990. *Solid State Communications*, **74:** 667.

Main, C. Berkin, J. and Merazga, A. 1991 in *New physical problems in electronic materials*, edited by M. Borissov, N. Kirov, J.M. Marshall and A. Vavrek. Singapore: World Scientific, 55.

Main, C. Brüggemann, R. Webb, D. P. Reynolds, S. 1993. *Journal of Non-Crystalline Solids*, **164-166:** 481.

Main, C. in *Amorphous and Microcrystalline Silicon Technology - 1997, Proceedings of MRS Symposium A, Vol. **467***, edited by M. Hack, E.A. Schiff, S. Wagner, A. Matsuda and R. Schropp, (MRS, Warrendale PA 1997) Ch.143, p.167.

Main, C. Reynolds, S. Zrinščak, I. Merazga, A. 2003. *Journal of Materials Science: Materials in Electronics,* **14** (10-12)**:** 681.

Main, C. Reynolds, S. Zrinščak, I. Merazga, A. 2004. *Journal of Non-Crystalline Solids*, **338–340:** 228.

Marple, D.T.F. 1966. *Physical Review*, **150:** 728.

Marshall, J.M. Pickin, W. Hepburn, A.R. Main, C. Brüggemann, R. 1991. *Journal of Non-Crystalline Solids*, **137-138:** 343.

Masuda, A. Ishibashi, Y. Matsumura, H. 2000 in *Amorphous and Heterogeneous Silicon Thin Films – 2000, Proceedings of MRS Symposium A, Vol. **609***, edited by R.W. Collins, H.M. Branz, S. Guha, H. Okamoto, M. Stutzmann, (MRS, San Francisco, 2000), A6.3.

Masuda, A. Izumi, A. Umemoto, H. Matsumura, H. 2002. *Vacuum*, **66:** 293.

Matsumura, H. 1998. *Japanese Journal of Applied Physics*, **37**: 3175.

Meier, J. Keppner, H. Dubail, S. Ziegler, Y. Feitknecht, L. Torres, P. Hof, C. Kroll, U. Fischer, D. Cuperus, J. Anna Selvan, J.A. Shah, A. 1998. *Proceedings of the 2nd World Conference on Photovoltaic Energy Conversion*, Vienna, July 1998, Vol. **I:** 375-380.

Mettler, A. Wyrsch, N. Shah, A. 1993, *Journal of Non-Crystalline Solids*, **164-166**, 427.

Mettler, A. 1994. PhD Thesis, University of Neuchâtel, Switzerland.

Mettler, A. Wyrsch, N. Goetz, M. Shah, A. 1994. *Solar Energy Materials and Solar Cells*, **34:** 533.

Morgado, E. 2002. *Journal of Non-Crystalline Solids*, **299-302:** 471.

Morita, Y. Ohshima, T. Nashiyama, I. Yamamoto, Y. Kawasaki, O. Matsuda, S. 1997. *Journal of Applied Physics*, **81:** 6491.

Mott, N.F. 1968. *Journal of Non-Crystalline Solids*, **1:**1.

Mott, N.F. and Davis, E.A. 1979. *Electronic processes in non-crystalline materials*, Oxford: Clarendon press, 15ff.

Naito, H. 1996. *Journal of Applied Physics*, **80:** 5089.

Neamen, D. A. 2003. *Semiconductor Physics Devices: Basic Principles – Third Edition*, New York, McGraw-Hill Higher Education, Ch 1, pp16.

Nesheva, D. Levi, Z. Aneva, Z. Zrinščak, I. Main, C. and Reynolds, S. 2002. *Journal of Nanoscience & Nanotechnology*, **2:** 645.

Norris, D. and Bawendi, M. 1996. *Physical Review B*, **53:** 16338.

Oheda, H. 1980. *Solid State Communications*, **33:** 203.

Okamoto, H. Kida, H. Hamakawa, Y. 1984. *Philosophical Magazine B*, **49:** 231.

Overhof H. and Thomas P. 1989. *Electronic Transport in Hydrogenated Amorphous Silicon*, Springer Tracts in Moden Physics Vol **114**, Heidelberg: Springer.

Panchuk, O. Savitskiy, A. Fochuk, P. Nykonyuk, Y. Parfenyuk, O. Shcherbak, L. Ilashchuk, M. Yatsunyk, L. and Feychuk, P. 1999. *Journal of Crystal Growth*, **197:** 607.

Pierz, K. Mell, H. Terjukov, J. 1985. *Journal of Non-Crystalline Solids*, **77-78:** 547.

Poruba, A. and Schauer, F. 1994 in *Proceedings of the 8th International School on Condensed Matter Physics: Electronic, Optoelectronic and Magnetic Thin Films*, Varna 1994, ed. J. M. Marshall, John Wiley, New York 1995, p.616.

Poruba, A. Vaněček, M. Meier, J. Shah, A. 2002. *Journal of Non-Crystalline Solids*, **299-302:** 536.

Reynolds, S. Main, C. Webb, D.P. and Rose, M.J. 2000. *Philosophical Magazine B*, **80:** 547.

Ritter, D. and Weiser, K. 1986. *Optics Communications*, **57:** 336.

Robertson, J. 2000. *Journal of Non-Crystalline Solids*, **266-269:**79.

Roca I Cabarrocas, P. 1998 in *Properties of Amorphous Silicon and its Alloys - Vol 19*, edited by Tim Searle, London, U.K., INSPEC, IEE, 3.

Roca I Cabarrocas, P. 2000. *Journal of Non-Crystalline Solids*, **266-269:** 31.

Rose, A. 1963. *Concepts in Photoconductivity and Allied Problems*, Interscience, New York, pp. 5.

Sasaki, M. Okamoto, S. Hishikawa, Y. Tsuda, S. Nakano, S. 1994. *Solar Energy Materials and Solar Cells*, **34:** 541.

Schmidt, J.A. Koropecki, R.R. Arce, R.D. Rubinelli, F.A. Buitrago, R.H. 2000. *Thin Solid Films*, **376:** 267.

Shimizu, T. Sugiyama, H. Kumeda, M. 2001. *Solar Energy Materials & Solar Cells*, **66:** 203.

Shockley, W. and Read, W.T. 1952. *Physical Review*, **87:** 835.

Siebke, F. Stiebig, H. Carius, R. 1997. *Solar Energy Materials and Solar Cells*, **49:** 7.

Simeon, E. Vanhellement, J. Claeys, C. 1996. *Applied Physics Letters*, **69:** 2858.

Simmons, J.G. and Taylor, G.W. 1971. *Physical Review B*, **4:** 502.

Sladèk, P. and Thèye, M.L. 1993. *Solid State Communications*, **89:** 199.

Sladèk, P. Stahel, P. 1995. *Philosophical Magazine B*, **71:** 871.

Spear, W.E. 1974. *Advances in Physics*, **23**: 523.

Spear, W.E. and LeComber, P.G. 1975. *Solid State Communication*, **17:** 1193.

Spear, W.E. and LeComber, P.G. 1977. *Advances in Physics*, **26:** 811.

Staebler D.L. and Wronski C.R. 1977. *Applied Physics Letters*, **31:** 292.

Stiebig, H. Brammer, T. Zimmer, J. Vetterl, O. Wagner, H. 2000. *Journal of Non-Crystalline Solids*, **266-269:** 1104.

Street, R.A. 1991. *Hydrogenated amorphous silicon*, Cambridge: Cambridge University Press, p4, 11, 18, 19, 29, 100, 109.

Stutzman, M. 1998. *Properties of Amorphous Silicon and its Alloys - Vol 19*, edited by Tim Searle, London, U.K., INSPEC, IEE, 61.

Swanepoel, R. 1983. *Journal of physics E, Scientific instruments*, **16:** 1214.

Tange, S. Inoue, K. Tonokura, K. Koshi, M. 2001. *Thin Solid Films*, **395:** 42.

Tiedje, T. and Rose, A. 1980. *Solid State Communications*, **37:** 49.

Urbach, F. 1953. *Physical Review*, **92:** 1324.

Vaněček, M. Kočka, J. Stuchlik, and J. Třika, A. 1981. *Solid State Communication*, **39:** 1199.

Vaněček, M. Poruba, A. Remeš, Z. Beck, N. Nesládek, M. 1998. *Journal of Non-Crystalline Solids*, **227-230:** 967.

Vetterl, O. Finger, F. Carius, R. Hapke, P. Houben, L. Kluth, O. Lambertz, A. Mück, A. Rech, B. Wagner, H. 2000. *Solar Energy Materials & Solar Cells*, **62:** 97.

Wanka, H.N. Zedlitz, R. Heintze, M. Schubert, M.B. in *Amorphous Silicon Technology - 1996, Proceedings of MRS Symposium A, Vol. **420**,* edited by M. Hack, E.A. Schiff, S. Wagner, A. Matsuda and R. Schropp, (MRS, Warrendale PA, 1996), p295.

Webb, D.P. 1994. PhD Thesis, University of Abertay Dundee, U.K.

Wiesman, H. Ghosh, A.K. McMahon, T. Strongin, M. 1979. *Journal of Applied Physics*, **50:** 3752.

Wolfe, D.M. and Lucovsky, G. 2000. *Journal of Non-Crystalline Solids*, **266-269:** 1009.

Wyrsch, N. Finger, F. McMahon, T.J. Vaněček, M. 1991. *Journal of Non-Crystalline Solids*, **137-138:** 347.

Yamaguchi, M. Taylor, S.J. Yang, M.J. Matsuda, S. 1996. *Journal of Applied Physics*, **80:** 4916.

Zielinger, J.P. Tapiero, M. Guellil, Z. Roosen, G. Delaye, P. Launay, J.C. and Mazoyer, V. 1993. *Materials Science and Engineering B*, **16:** 273.

Publications arising from this work

Zrinščak, I. Reynolds, S. Main, C. Persheyev, S. and Rose, M.J. 2001. A Comparison of the Electronic Properties of Hot-Wire and PECVD Amorphous Silicon in the Annealed and Light-Soaked States. Published in *Materials for Information Technology in the New Millennium*, edited by JM Marshall, AG Petrov, A Vavrek, D Nesheva, D Dimova-Malinovska, JM Maud (ISCMP2000, Varna, Bulgaria, September 2000) 336-339.

Persheyev, S.K. Goldie, D.M. Gibson, R.A.G. Rose, M.J. Anthony, S. Keeble, D.J Robb, K. Main, C. Reynolds, S. Zrinščak, I. 2001. Depth profiling and the effect of oxygen and carbon on the photoelectrical properties of amorphous silicon films deposited using tungsten wire filaments. *Thin Solid Films*, 395: 130.

Brüggemann, R. Kleider, J.P. Bronner, W. and Zrinščak, I. 2002. Influence of electron and proton irradiation on the electronic properties of microcrystalline silicon. *Journal of Non-Crystalline Solids*, **299-302:** 632.

Nesheva, D. Levi, Z. Aneva, Z. Zrinščak, I. Main, C. and Reynolds, S. 2002. Size-dependent absorption and defect states in CdSe nanocrystals in various multilayer structures. *Journal of Nanoscience & Nanotechnology,* **2:** 645.

Reynolds, S. Main, C. Zrinščak, I. Aneva, Z. and Nesheva, D. 2003. A Study of Electronic Defects in Hydrogenated Amorphous Silicon Prepared by the Expanding Thermal Plasma Technique. Published in *Amorphous and Nanocrystalline Silicon-Based Films – 2003, Proceedings of MRS Symposium A, Vol.* ***762***, edited by John R. Abelson, Gautam Ganguly, Hideki Matsumura, John Robertson, Eric A. Schiff (MRS, San Francisco, 2003), A19.14.

Main, C. Reynolds, S. Zrinščak, I. and Merazga, A. 2003. Determination of Defect Densities by Constant Photocurrent Method - Comparison of AC and DC Methods. Published in *Amorphous and Nanocrystalline Silicon-Based Films – 2003, Proceedings of MRS Symposium A, Vol.* ***762***, edited by John R. Abelson, Gautam Ganguly, Hideki Matsumura, John Robertson, Eric A. Schiff (MRS, San Francisco, 2003), A19.12.

Main, C. Reynolds, S. Zrinščak, I. Merazga, A. 2003. The influence of generation and transport processes in the constant photocurrent method in a-Si:H. *Journal of Materials Science: Materials in Electronics*, **14:** 681.

Main, C. Reynolds, S. Zrinščak, I. Merazga, A. 2004. Comparison of AC and DC constant photocurrent methods for determination of defect densities. *Journal of Non-Crystalline Solids*, **338–340:** 228.

COMPARISON OF ELECTRONIC PROPERTIES OF HOT-WIRE AND PECVD AMORPHOUS SILICON IN THE ANNEALED AND LIGHT-SOAKED STATES

I. Zrinščak, S. Reynolds, C. Main, S. Persheyev# and M.J. Rose#
School of Science and Engineering, University of Abertay Dundee, Bell Street, Dundee DD1 1HG, U.K., and # Department of Electronic Engineering and Physics, University of Dundee, Dundee DD1 4HN, U.K.

ABSTRACT

The electronic properties of hydrogenated amorphous silicon prepared by hot-wire and PECVD methods and subjected to light soaking are investigated using transient photocurrent and constant photocurrent spectroscopies. Conduction band tails and defect densities in the upper half of the gap are found to be similar in both materials, but the valence band tail is broader and the defect density in the lower half of the gap much higher in our hot wire material.

1. Introduction

The electronic properties of hydrogenated amorphous silicon (a-Si:H) are strongly influenced by defects associated with the presence of dangling bonds and also by metastable defects created by illumination. Undoped a-Si:H films can be produced at high deposition rates by the hot-wire (HW) or 'catalytic' CVD method, having a smaller hydrogen content and greater electronic stability on illumination than conventional RF PECVD films[1]. As part of a wider programme of commercialisation and refinement of the HW technique, HW and PECVD films subjected to annealing - light soaking cycles have been investigated using transient photocurrent spectroscopy (TPC)[2] and the absolute constant photocurrent method (A-CPM)[3].

2. Experimental

2.1 Materials preparation and conditioning

HW films were prepared in a laboratory system with: gas flow rate 8 sccm, chamber pressure 220 mTorr, tungsten wire temperature 1500 °C, substrate temperature 200 °C. PECVD films were prepared in an industrial reactor with: 5% hydrogen dilution, chamber pressure 500 mTorr, substrate temperature 200 °C. Representative HW and PECVD films were measured after annealing at 180 °C for 3 hours, and again following exposure to simulated AM1 radiation for 10, 100 and 1000 minutes.

2.2 Measurement systems

Our TPC system, and the methods employed in calculating the DOS from current-time data, have been described elsewhere[2]. Data were recorded typically between 1 ns and 10 s following excitation by a 4 ns, 620 nm pulse from a nitrogen-pumped dye laser, providing an initial carrier density of approximately 10^{15} cm^{-3}. Absolute CPM spectra were obtained following the procedures described by Vanecek *et al* and calibrated with reference to optical

transmission measurements through the Ritter-Weiser formula[3]. The DOS was obtained by differentiation of the absorption curve.

3. Results and discussion

3.1 Steady-state measurements

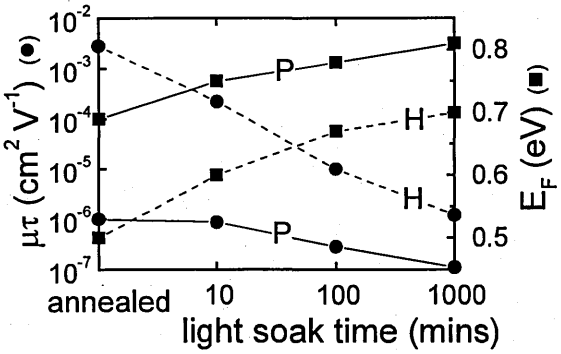

Figure 1: Fermi level positions and μτ-products for HW and PECVD samples

Fermi level positions and μτ-products obtained for the PECVD film are typical of literature values for intrinsic amorphous silicon[4]. However, although μτ-products for the HW material are promisingly high, the position of the Fermi level indicates clearly that the sample is inadvertently moderately n-type. Thus the high values cannot be attributed to a fundamental improvement in electronic properties. The source of contamination has not yet been determined.

Additional light-induced defects appear to compensate the donor impurities in the HW material. Where the Fermi level positions overlap the μτ-products for both samples are similar, suggesting that if impurities could be eliminated the resulting intrinsic HW material might be of reasonable quality.

3.2 TPC data

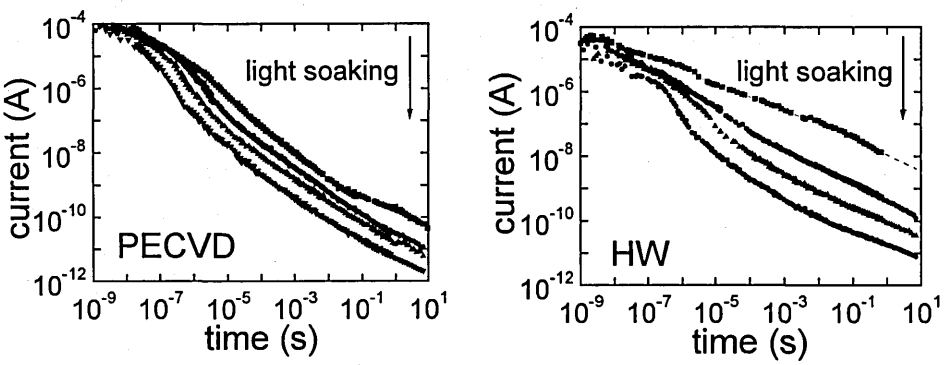

Figure 2: Raw TPC data obtained from PECVD and HW samples

In the PECVD sample, the effect of light soaking is revealed in Figure 2 as a more rapid fall in current at $\approx 10^{-7}$ s, associated with trapping into an increased density of defects[2]. The annealed HW sample displays the shallow decay associated with recombination-free transport in n-type material[5]. However, with increasing light soaking, E_F moves to a more intrinsic position and the decays more closely resemble the PECVD data.

3.3 CPM data

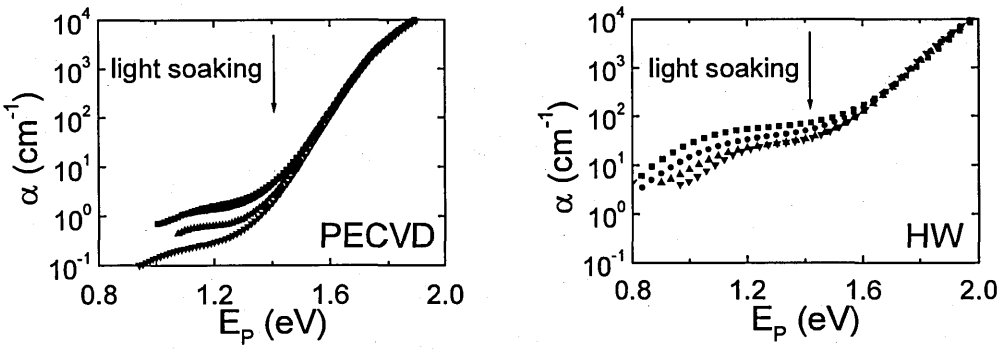

Figure 3: Absolute CPM optical absorption spectra

From Figure 3 it appears that the HW material quality is poor in comparison to PECVD, with greater low energy absorption and a shallower Urbach tail. Both show similar fractional increase in absorption on light soaking.

3.4 DOS plots

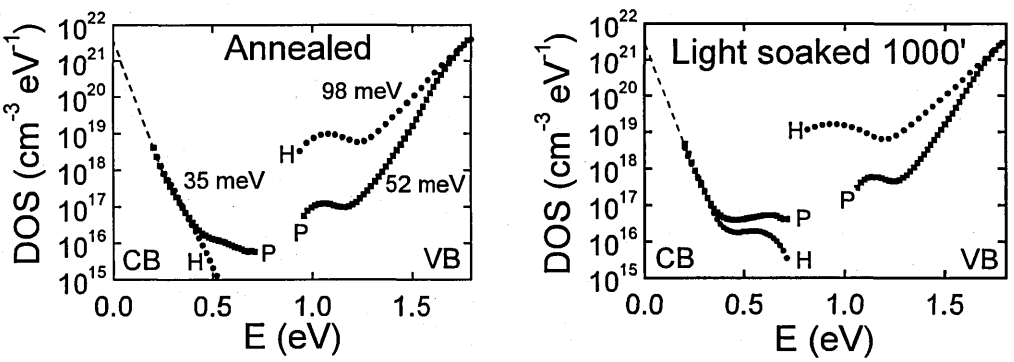

Figure 4: DOS plots obtained by combination of TPC and CPM data

The DOS profiles shown in figure 4 extend over most of the mobility gap, with the TPC data providing the upper (CB) and the CPM the lower (VB) portion. The DOS scale is uncalibrated; we have adjusted the band edge densities to be equal at 4×10^{21} cm^{-3} eV^{-1}.

The conduction band tails for HW and PECVD samples have a similar slope, approximately 35 meV. However, the valence band tail for the HW sample is much broader, 98 meV compared with 52 meV, and the defect density is some two orders higher. Both observations are consistent with its n-type character[6]. Light soaking the PECVD material increases the defect density by a factor of 5 to 10 over both portions of the DOS. Interpretation of the annealed HW TPC data is limited by the shallow Fermi energy position (0.5 eV) as DOS calculations below E_F are invalid[2]. For the light-soaked HW sample, where the range of validity of the DOS should extend to 0.7 eV, the TPC data indicate similar defect densities in both HW and PECVD materials. This contrasts markedly with the CPM data. As the energy regions probed do not overlap, the defect density could increase very rapidly in the HW material between 0.6 and 0.8 eV, in accordance with the defect pool model which predicts a large D^- contribution in n-type material deep in the gap.

4. Conclusions

Conduction band tails in a-Si:H samples prepared in our laboratory by the HW method have a characteristic energy of typically 35 meV, comparable with commercial PECVD material. Defect densities in the upper portion of the mobility gap are also similar, and are estimated to be between 10^{16} and 10^{17} cm^{-3} eV^{-1} depending on the degree of light soaking. The valence band tail in the HW material has a slope of 98 meV, approximately twice that of PECVD material, and a defect density some 100 times greater in the lower portion of the gap. More detailed and reliable studies of HW material quality will be possible once persistent n-type contamination has been eradicated.

5. References

[1] M. Heintze, R. Zedlitz, H.N. Wanka and M.B. Schubert, J. Appl. Phys. 79, 2699, 1996.

[2] S. Reynolds, C. Main, D.P. Webb and M.J. Rose, Philos. Mag. B 80, 547, 2000.

[3] M. Vanecek, J. Kocka, A. Poruba and A. Fejfar, J. Appl. Phys. 78, 6203, 1995.

[4] R. Brüggemann, in *Properties of Amorphous Silicon and its Alloys*, ed. T. Searle (IEE, 1998), p217.

[5] C. Main, A. Merazga, I.K. Kristensen and J. Berkin, Solid State Comms. 74, 667, 1990.

[6] L. Ley, in *Properties of Amorphous Silicon and its Alloys*, ed. T. Searle (IEE, 1998), p113.

6. Acknowledgements

EPSRC support (grant number GR/M16696) is gratefully acknowledged.